Final Technical Report: Multipoint Pressure and Temperature Sensing Fiber Optic Cable for Monitoring CO_2 Sequestration

Contract #: DE-FE0010116
Report Period: 01/01/2013 – 12/31/2014
Budget Period: 01/01/2013 – 12/31/2014

PI: Dr. William Challener
GE Global Research
One Research Circle
Niskayuna, NY 12309
(518) 387-6886
challene@ge.com
DUNS 086188401

Department of Energy
National Energy Technology Laboratory
3610 Collins Ferry Road
Morgantown, WV 26507

Program Manager: Jason Hissam
Jason.Hissam@netl.doe.gov

Award Administrator: Diane Franklin
diane.franklin@netl.doe.gov

February 10, 2015

Submitted by William A. Challener
William A. Challener

This report was prepared as an account of work sponsored by an agency of the United States Government. Neither the United States Government nor any agency thereof, nor any of their employees, makes any warranty, express or implied, or assumes any legal liability or responsibility for the accuracy, completeness, or usefulness of any information, apparatus, product, or process disclosed, or represents that its use would not infringe privately owned rights. Reference herein to any specific commercial product, process, or service by trade name, trademark, manufacturer, or otherwise does not necessarily constitute or imply its endorsement, recommendation, or favoring by the United States Government or any agency thereof. The views and opinions of authors expressed herein do not necessarily state or reflect those of the United States Government or any agency thereof.

Abstract

This report describes the work completed on contract DE-FE0010116. The goal of this two year project was to develop and demonstrate in the laboratory a highly accurate multi-point pressure measurement fiber optic cable based on MEMS pressure sensors suitable for downhole deployment in a CO_2 sequestration well. The sensor interrogator was also to be demonstrated in a remote monitoring system and environmental testing was to be completed to indicate its downhole survivability over a lengthy period of time (e.g., 20 years). An interrogator system based on a pulsed laser excitation was shown to be capable of multiple (potentially 100+) simultaneous sensor measurements. Two sensors packages were completed and spliced in a cable onto the same fiber and measured. One sensor package was subsequently measured at high temperatures and pressures in supercritical CO_2, while the other package was measured prior and after being subjected to high torque stresses to mimic downhole deployment. The environmental and stress tests indicated areas in which the package design should be further improved.

Table of Contents

1. Executive summary	5
2. Objectives	6
3. Background	6
3. Task 1: Project management	7
4. Task 2: Design and fabrication of sensor package	7
5. Task 3: Design of readout system	44
6. Task 4: Fabricate and test fiber sensor cable	89
7. Task 5: Wireless remote sensor operation	119
8. Conclusions and summary	136
8. List of acronyms and abbreviations	137
9. Acknowledgments	138
10. References	139

Executive Summary

This report describes the work completed on the two year contract DE-FE0010116, to develop and demonstrate in the laboratory a multipoint pressure and temperature sensing fiber optic cable for monitoring CO_2 sequestration.

In the course of this project, a sensor package was designed and the parts were fabricated. The GE measurement and Control business specially fabricated high pressure Si MEMS sensor die for the package. A process was developed for aligning the sensor die to the fiber and packaging the sensor die. Two sensor packages were assembled. A high pressure die specifically fabricated for this project was placed in one package for environmental testing at high temperatures and pressures even though the die had a low "Q." A high "Q" low pressure sensor die was placed in the other package for measurements of mechanical stress testing and for making a comparison between the relative signal amplitudes of the two die.

Four different interrogator approaches were investigated in the course of the project. The conventional fiber optic interrogator used for a single MEMS sensor and an interferometric interrogator were both shown to operate with at most four multiplexed sensors. A modulated laser approach was found not to work at all. However, the pulsed laser interrogator was found to be potentially suitable for measurements of hundreds of sensors in the same cable.

At the beginning of this project, there were no known commercially available wavelength division multiplexers (WDMs) or coupler/splitters that could survive 250°C temperature for long term measurements. Two vendors were identified who both supplied custom parts. The WDMs successfully survived for >1600 hours at 250°C with little/no change. High temperature splitters received from a two vendors successfully survived for >1000 hours at 250°C with no change.

One sensor package was tested at high temperatures and pressures. A measurement of its temperature and pressure sensitivities was obtained, though the package failed at 100°C and 5000 psi in supercritical CO_2. A sheave tester was designed, fabricated and assembled to apply torque to a sensor package to simulate deployment stresses. The second sensor package was tested on this device and the weld between the sensor and the cable cracked though the sensor package itself exhibited only minor effects. A second, more stringent test with larger applied torques was subsequently applied to the sensor package. This resulted in some small frequency changes but no loss of signal.

Long term environmental testing of Inconel membranes was completed. There was superficial corrosion when placed in a saturated brine solution with sc-CO_2 at 10 kpsi and 250°C for 200 hours but the mass change was negligible. A second set of membranes was exposed to pure sc-CO_2 at 250°C and 10 kpsi for 1100 hours. Again, the mass change was negligible and little or no corrosion was observed. These results indicate that Inconel 625 is an excellent package material, although the specific composition of downhole fluid must be taken into consideration when deploying sensors for very long periods of time.

Objectives

The overall program objective is to develop and demonstrate the technology for implementing multi-point sensors on a fiber optic cable for remote monitoring of pressure and temperature in the harsh environment of deep underground CO_2 sequestration cavities. In the first year of the project, the team was to design a MEMS pressure/ temperature sensor for operation up to 250°C and 10,000 psi, and develop a low-cost, multiplexed readout method. In the second year of the project, a robust fiber optic cable with multiple spliced sensors was be fabricated, and a complete multi-point sensing cable able to withstand long-term downhole deployment was demonstrated in the laboratory with remote activation and operation.

Background

A proposed means for reducing CO_2 atmospheric emissions is to sequester CO_2 deep underground in depleted oil wells or saline reservoirs. In such a case, it will be very important to monitor the stored CO_2 over time to ensure that it is not leaking back out into the atmosphere. By making accurate distributed pressure measurement in the well, it is possible to monitor for leakage, flow and CO_2 plume extent.

As shown in Fig. 1, CO_2 under pressure can be forced into deep underground saline reservoirs.

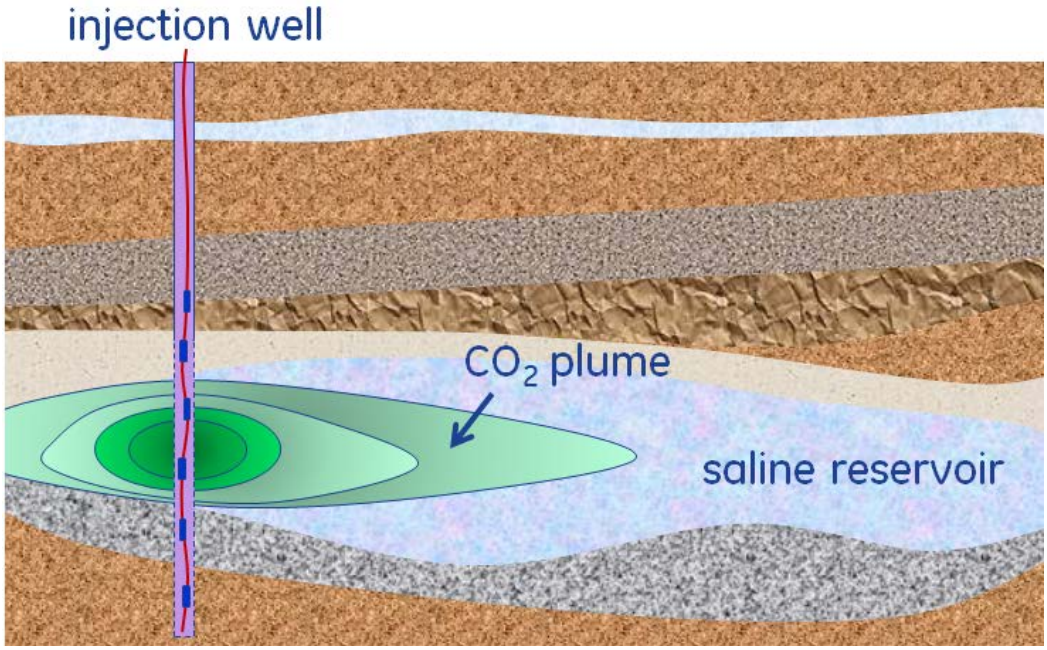

Fig. 1: Illustration of a CO_2 sequestration well utilizing an underground brine cavity. CO_2 is forced under pressure into the reservoir through an injection well. As the CO_2 penetrates the reservoir, the extent of the plume enlarges. There is a density and pressure gradient associated with the concentration of CO_2 in the reservoir. Accurate pressure measurements along the length of the well can be used to determine the plume extent.

As the CO_2 plume extends into a brine reservoir, for example, it creates a density gradient as shown in the figure. It has been shown that this gradient also leads to a pressure gradient that can be measured.[1] A change in slope of the pressure is indicative of the flow front between the CO_2 and the original saline solution. By accurately measuring the pressure along the length of the saline reservoir, it is possible to estimate the position of the flow front and the extent of the reservoir. However, the error in determining the location of the flow front is highly dependent upon the accuracy and spacing of the downhole pressure measurements. It was found[1] that a 1 psi pressure measurement accuracy was sufficient to locate the flow front to within an accuracy of 5% with a 100 foot spacing between measurements, while a 5 psi pressure measurement accuracy required a 3 foot spacing to obtain the same flow front location accuracy. This result indicates the need for both distributed pressure measurements and highly accurate pressure measurements. In this project, we have developed a means for splicing potentially hundreds of MEMS-based pressure sensors onto a single downhole cable, with each sensor able to provide highly accurate (±0.01 to ±0.1% full scale) and highly stable (±0.01% full scale/year) pressure measurements that could meet this need.

In this report we refer to "supercritical CO_2" (sc-CO_2). When CO_2 exists at pressures greater than 1070 psi (7.39 MPa) and temperatures above 30°C, it enters the supercritical state in which the fluid has both gaseous and liquid-like properties. The temperatures and pressures required to sequester the CO_2 in underground cavities will generally correspond to supercritical CO_2.

In this final project report we will describe the work accomplished for each task in the project.

Task 1: Project Management and Planning

This technical report is the final requirement of this task.

Task 2.0: Design and Fabrication of Sensor Package

For measurement of pressure and temperature in a CO_2 sequestration cavity, the sensor package must withstand the harsh environment of sc-CO_2 at up to 250°C and 10 kpsi for a period of 20 years, and accurately measure pressure and temperature at multiple points along a single optical fiber in the well without drift during this time period.

A. Outer package material

As background to this project, a single point MEMS-based pressure sensor had been developed earlier for high temperature, high pressure downhole measurements. This sensor is shown in Fig. 2. This sensor package does not meet the requirements of the current project in a few ways, but many of the same principles developed for that sensor package can be applied for this project. For example, the sensor in Fig. 2 was fabricated from Inconel 625. This is a nickel-chromium alloy with high strength and outstanding corrosion resistance.[2] It includes small amounts of other elements including iron, molybdenum, and niobium. It has been found especially useful in

sea water applications, for example, due to its resistance to pitting and crevice corrosion. It has high thermal fatigue strength and is relatively easily welded or brazed, both properties necessary for this application. Inconel 625 has been previously studied in a sc-CO_2 environment at 650°C and 3 kpsi.[3] It was found that a thin, dense Cr oxide layer provided the corrosion resistance. In this environment, the Inconel exhibited a weight gain over time *t* due to corrosion given by

$$\Delta W = 0.01\, t^{0.35} \tag{1}$$

where time is measured in hours. The samples in this experiment were tested for 3000 hours total.

Fig. 2: Photo of single point MEMS pressure sensor developed for high tempeature, high pressure harsh environments. The package diameter is 3 cm. The cable pigtail contains a single mode optical fiber.

This was one of the better alloys studied as shown by the results in Fig. 3. Therefore, for the new sensor package it was decided to use Inconel 625. This material is also compatible with the steel cable that was recovered from the previous project and that will be used in this project to demonstrate welding of the sensor into the cable.

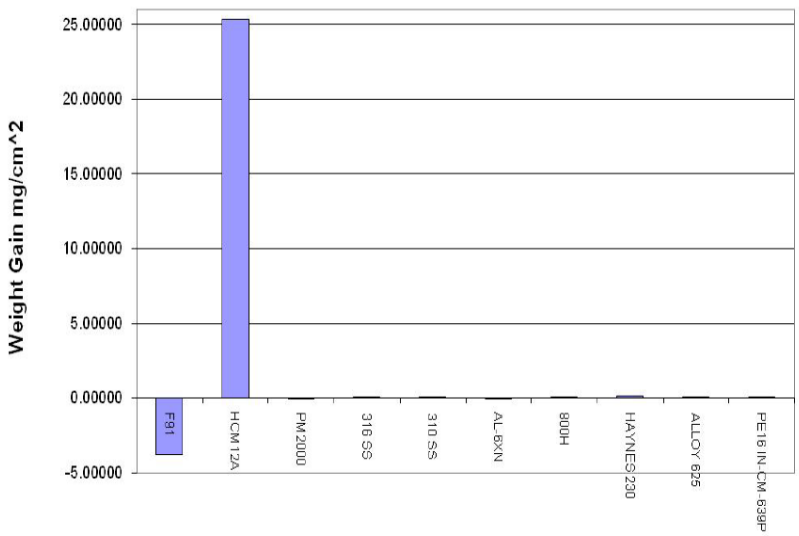

Fig. 3: Data from reference[4] on weight gain due to corrosion of various alloys in a sc-CO_2 environment. The Inconel 625 alloy (second from right) is clearly one of the alloys exhibiting low corrosion.

B. High temperature adhesives

The package design that was ultimately settled upon required the use of nonmetallic adhesives that could survive high temperatures (at least 250°C) and at least in some cases remain optically transparent. This section first describes the measurement process and results of adhesive testing.

The goal is to create a mechanically stable bond between an optical fiber and either the sensor die, a ceramic ferrule, or the metallic package that can withstand temperatures up to 250°C over extended periods of time. The attachment between fiber and die must also be transparent to laser light with wavelengths ranging from 1300 to 1600 nm. The proposed design uses a ferrule stick to contain the optical fiber and a matching ferrule sleeve to allow for easy attachment of the optical fiber assembly to the Si spacer (see Fig. 4).

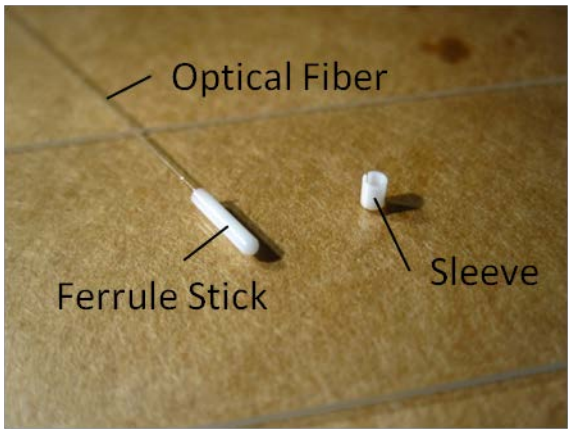

Fig. 4: Photograph of an optical fiber that is attached to a ferrule stick. A matching ferrule sleeve is glued to a glass slide using high temperature epoxy.

Various adhesives have been tested. EPO-TEK® 353ND from Epoxy Technology, Inc. was evaluated as described below. The ferrule sleeve is attached to a glass slide (emulating the glass prism) using this high temperature epoxy. The amount of epoxy applied to the hollow sleeve surface has to be controlled stringently to avoid filling of the sleeve through capillary forces. In order to generate epoxy films with a controlled thickness, epoxy is dispensed on a microscope cover slip using spacers of multiple layers of polyimide tape. By using a razor blade any excess epoxy can be scraped off resulting in epoxy films with an accurate thickness. Film thicknesses of 90, 180, and 270 μm were used. The ferrule sleeve was dipped into an epoxy film to wet the surface of the hollow sleeve. An epoxy film thickness of 90 μm resulted in an opening of the sleeve whereas the larger film thicknesses of 180 and 270 μm resulted in a partially and a completely filled sleeve, respectively (Fig. 5).

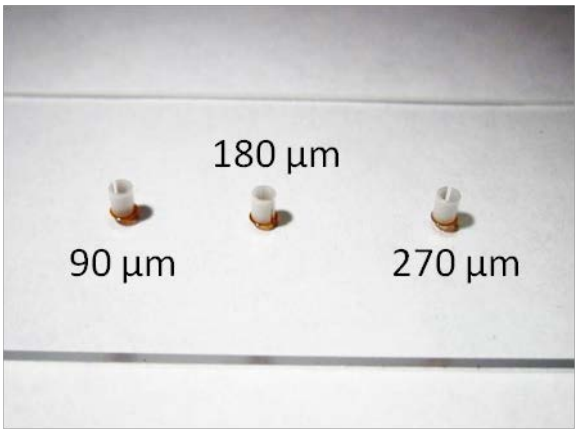

(a)

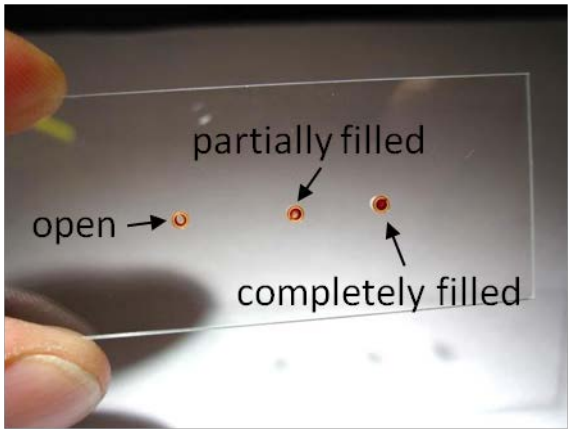

(b)

Fig. 5: Photographs of ferrule sleeves attached to a glass slide using different thicknesses of epoxy films (a) side view of glass slide and (b) backside view.

The epoxy was cured at 130°C for 5 min. After this initial cure, the ferrule stick containing the optical fiber was inserted into the sleeve using the same epoxy as adhesive. A final cure at 180°C for 60 min cross linked all the epoxy to achieve its maximum strength. Fig. 6 illustrates a

subassembly composed of optical fiber, ferrule stick, and matching ferrule sleeve that is attached to a glass slide. Only the first curing step was performed, hence the non-tarnished color of the epoxy covering the ferrule stick surface. The epoxy significantly darkens after the final cure process at 180°C. A summary of the curing conditions is shown in Table 1.

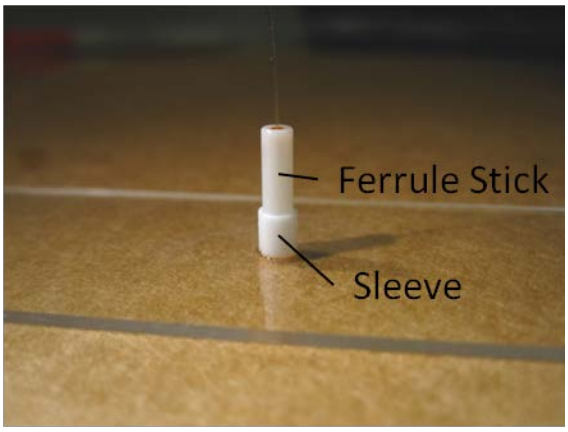

(a)

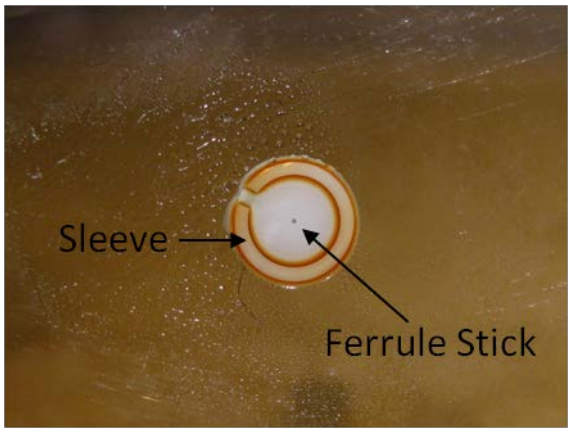

(b)

Fig. 6: Photograph of fiber optical subassembly attached to a glass slide by epoxy: (a) side view of glass slide and (b) backside view of glass slide.

Table 1: Curing condition used for high temperature epoxy.

Epoxy Type	**Curing Condition**	**Operating Temperature** (continuous)	**Operating Temperature** (intermittent)
EPO-TEK 353ND	*Pre-Cure* 130°C for 5 min *Post-Cure* 180°C for 60 min	-55 to 250°C	-55 to 350°C

To investigate the mechanical strength of the fiber-to-prism bond at elevated temperatures, a pull stress test using a furnace with an opening in the top was constructed. The glass slide and fiber subassembly containing one end of the optical fiber were placed in the oven chamber while the other end of the fiber was relayed over to metal rolls to a collection bin. A free hanging weight (100g) attached to the fiber end applied a tensile force to the fiber-to-prism bond. A sketch of the experimental setup is shown in Fig. 7. Photographs showing the side and top view of the experimental setup are depicted in Fig. 8.

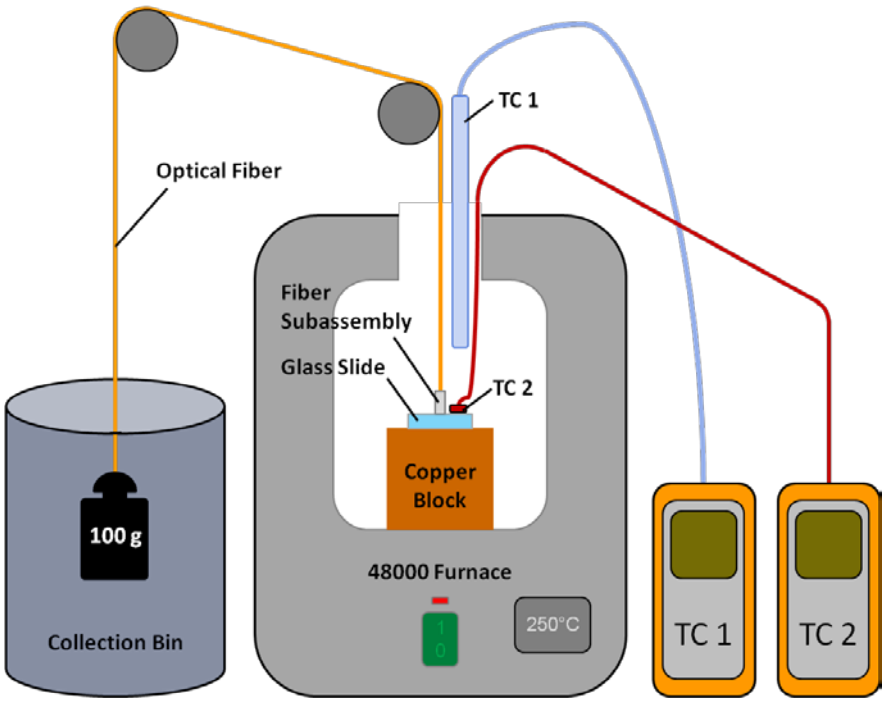

Fig. 7: Sketch of the experimental setup. A copper block with a large thermal mass and good thermal conductivity can be used to minimize temperature fluctuations of the device under test.

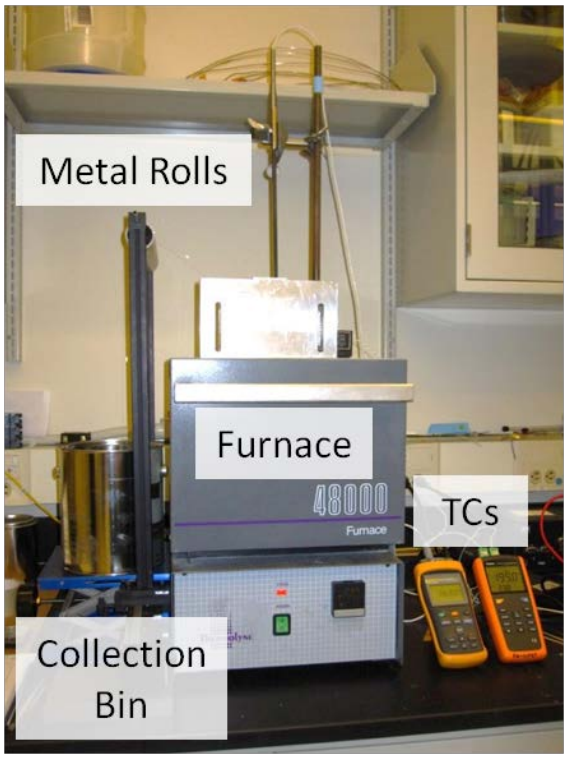

(a)

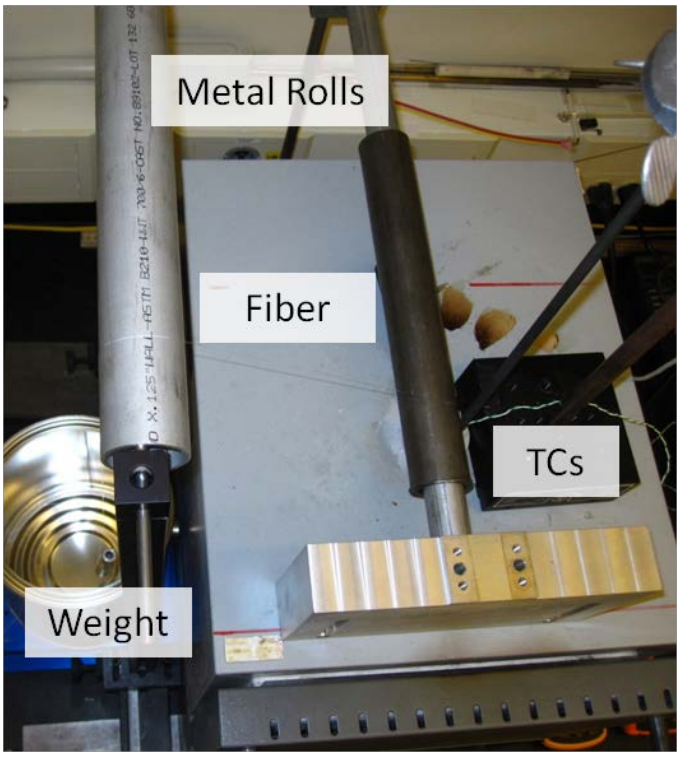

(b)

Fig. 8: Photographs of the experimental setup: (a) side view and (b) top view.

The collection bin allows for the weight to be captured when the fiber subassembly separates from the glass slide during stress testing at elevated temperatures. Two thermocouples (TCs) were used to monitor the temperatures of the furnace chamber and the fiber-to-prism bond. To improve the measurement accuracy of the temperature, the second TC is brought in physical contact with the epoxy bond using a heat-conductive paste (Fig. 9).

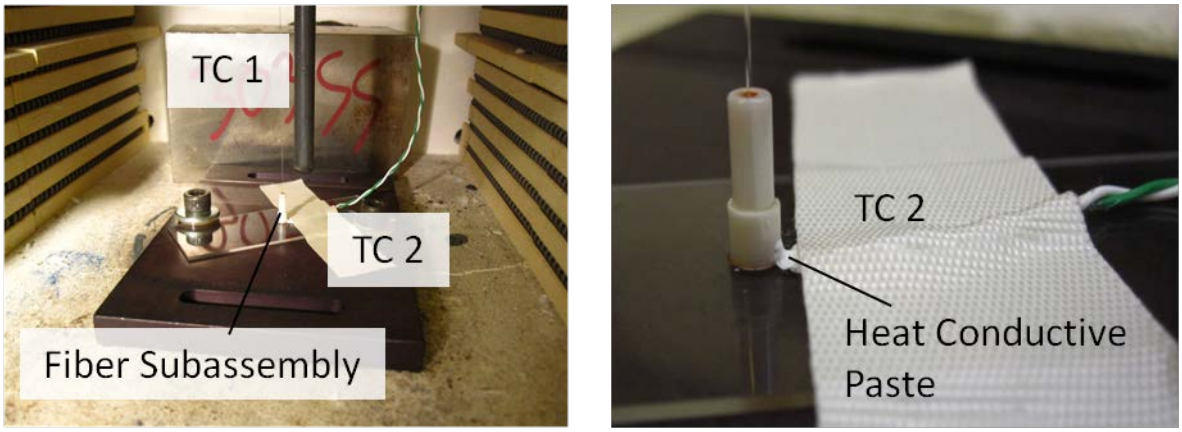

(a) (b)

Fig. 9: Photographs showing the inside of the furnace chamber: (a) view of the entire chamber and (b) close up picture of fiber subassembly.

During experimentation it was observed that the temperature of the glass slide could deviate from the air temperature of the furnace by as much as 25°C. During soak periods, the furnace would stabilize the temperature by turning the heater coils on and off. To eliminate any potential temperature fluctuations during these on and off cycles, a large copper block was used as a base for the glass slide (Fig. 10).

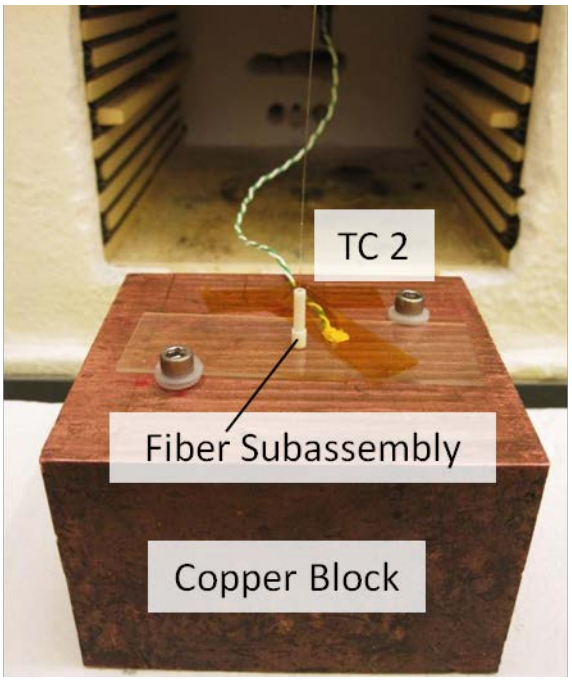

Fig. 10: Photograph of a fiber subassembly attached to a glass slide that is mounted onto a copper block.

The copper block has high thermal conductivity and a large thermal mass guaranteeing a stable temperature of the fiber-to-glass interface during soak periods.

During stress testing, the furnace temperature was ramped to 250°C and allowed to soak for 45 min. At these temperatures the epoxy significantly weakens. After soak times of 20 to 30 min the bond between fiber subassembly and glass slide would fail. A photograph of a broken bond is shown in Fig. 11. The darkening of the epoxy after exposure to 250°C is clearly visible. To improve the bond strength, a combination of different adhesives, e.g., an ultrahigh temperature ceramic adhesive for the sleeve attachment and an optically transparent epoxy for the ferrule stick attachment may be employed.

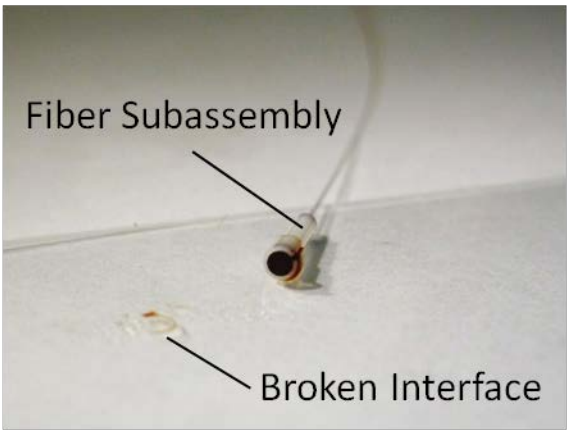

Fig. 11: Photograph of a fiber subassembly that separated from a glass slide during stress testing.

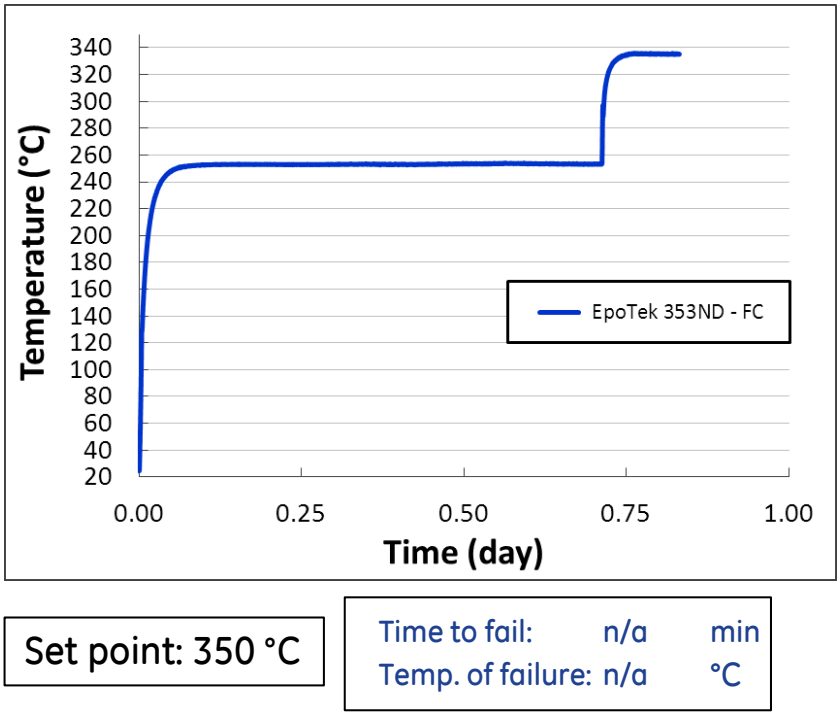

Fig. 12: Example of data collected for EpoTek 353ND high temperature epoxy. This is a plot of oven temperature at the point of the epoxy bond, which is slightly lower than the oven set point. The oven was first ramped to a sample temperature slightly above 250°C. At this temperature the bond survived for over half a day. The oven was then ramped to a sample temperature of 330°C and the bond continued to survive for at least two hours.

The optical transmission of the EPO-TEK 353ND epoxy was measured as a function of thickness after curing for two to three weeks at 270°C. Epoxy samples laminated between glass microscope slides are shown in Fig. 13(a). Transmittance measurements as a function of thickness are shown in Fig. 13(b).

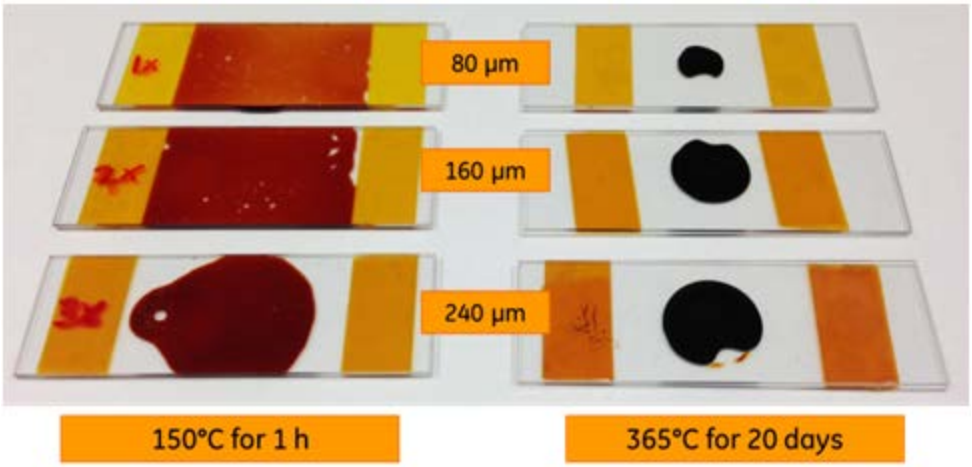

(a)

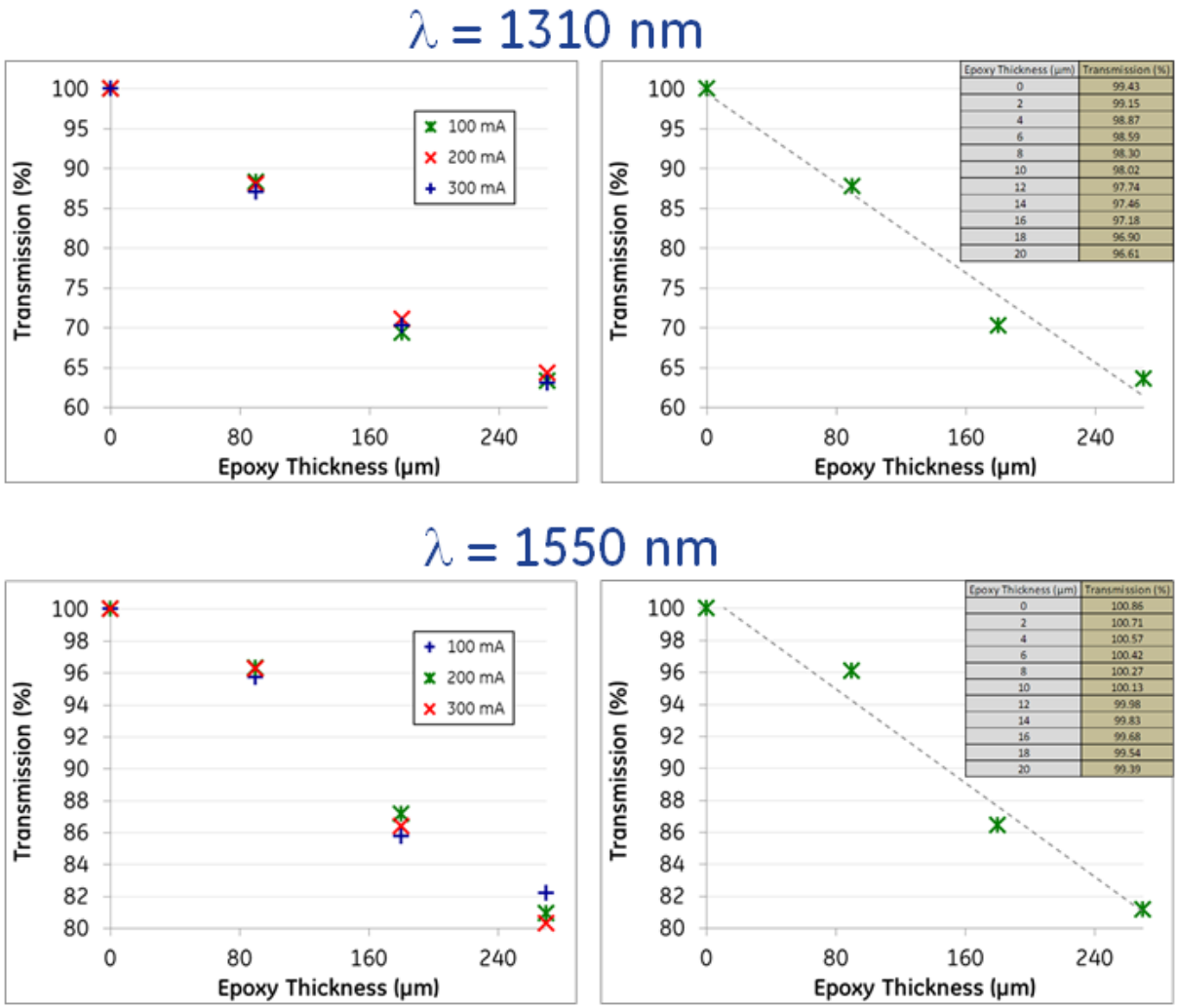

(b)

Fig. 13: (a) Examples of EPO-TEK 353ND optical high temperature epoxy laminated between microscope slides and cured at two different temperatures and times. (b) Measurement of transmittance of epoxy samples as a function of thickness.

C. Package design

Because the sensor package developed in the earlier project was designed for a single point sensor measurement, it does not include a means for transmitting light past the sensor into the fiber continuing on down the cable and, therefore, it cannot be spliced into the middle of an optical cable. This is one of the key issues to be dealt with in the new sensor package design. Also, the sensor package itself in the previous project was relatively large, having a 3 cm diameter. If such a package were spliced into the middle of a cable, it would be very difficult to deploy the cable because the sensor would not readily pass around a sheave or go through the packing to go into the well as shown in Fig. 14. Indeed, the sheave diameter as shown in Fig. 14 was designed for ¼″ (6.35 mm) diameter cable tubing. As the tubing diameter increases, the sheave and spool diameters must also increase correspondingly. This in turn increases the difficulty of cable deployment and greatly increases the cost of the cable. There is, therefore, a strong incentive to design the sensor package to have as small a diameter as possible. The original goal for the new sensor was a 3/8″ (9.53 mm) diameter package. In the first iteration of the package, the diameter had to be slightly increased to 7/16″ (11.11 mm).

Fig. 14: Fiber cable passes around two sheaves during deployment as shown here with a blue sheave on the ground and an aluminum sheave in the sky at the top of the well. The ¼″ diameter cable passes under the blue sheave and over the aluminum sheave and then down into the well pipe. The diameter of the sheaves is determined by the flexibility of the cable, which is itself determined primarily by the cable material, diameter and wall thickness.

The single point sensor package was also limited to some extent in its temperature range (although it was tested up to 260°C) due to the manner in which the external pressure was transduced to the silicon MEMS die via silicone oil. The external pressure causes flexure of a

very thin Inconel diaphragm on the surface of the sensor. The diaphragm is the corrugated region in Figs. 2 and 15. As the diaphragm flexes, it applies pressure to the internal silicone oil which surrounds the Si MEMS sensor die. The increased pressure in the oil causes the thin Si membrane in the MEMS die to flex, thereby applying strain to the MEMS resonator and changing its vibrational frequency. The thermal expansion coefficient of silicone oil is much larger than that of Inconel. Therefore, as shown in Fig. 15, even when no external pressure is applied to the sensor, if the temperature of the sensor is increased, then the thermal expansion of the oil within the package generates enormous pressure which is directly applied to the MEMS sensor. This is partly why the pressure readings of the sensor must be calibrated as a function of temperature, and why it is necessary to know the sensor temperature accurately in order to determine the pressure. Also, without carefully minimizing the volume of the oil inside the package, the pressure generated by the oil at high temperatures may be sufficient to rupture the diaphragm. In order to accommodate the pressure and temperature range for the new sensor, it was desirable to minimize the thermal effect of the oil on the sensor as much as possible.

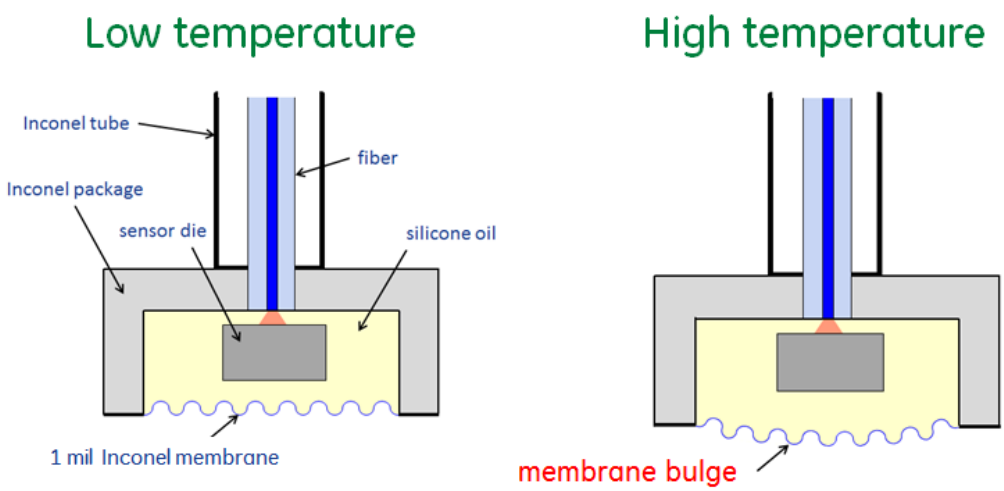

Fig. 15: Sensor die cavity is surrounded by silicone oil and isolated from the environment by a thin Inconel membrane. (a) At room temperature, the oil is typically at atmospheric pressure and there is no stress on the membrane. (b) As the temperature rises, the oil expands much more than the surrounding Inconel package, causing enormous stress in the membrane and making it bulge outward.

The general package design is shown in Fig. 16.

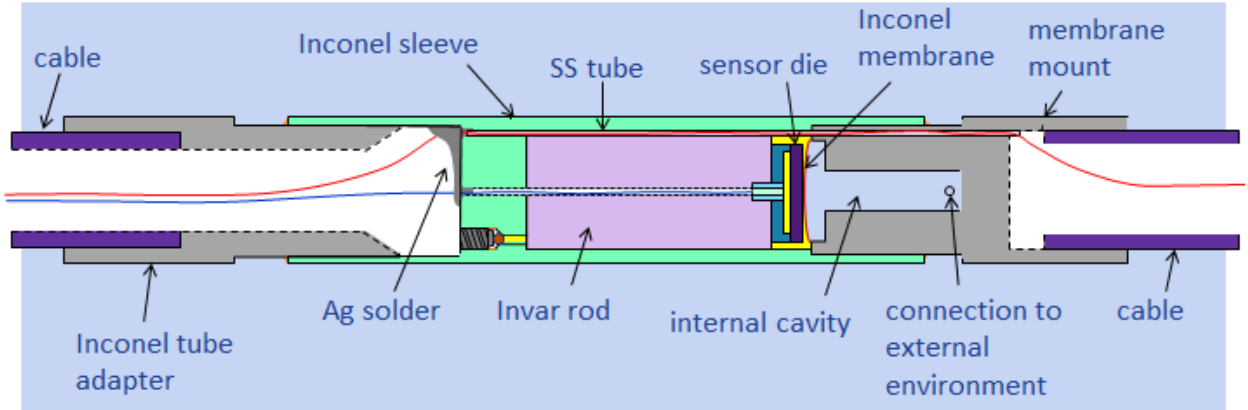

Fig. 16: Sketch of sensor package. The cable enters the package from the left. The fiber splitter or WDM is located to the left of this figure and will be discussed in Section D. A fiber also exits the package to the right to carry light on down to the next sensor. The package is designed to be spliced into the cable.

Not shown in this figure, but located to the left, *i.e.*, upstream and closer to the surface, is another package that contains the fiber wavelength division multiplexer (WDM) or optical splitter. This component and package will be discussed in section D. Nevertheless, at the point on the left of Fig. 16 where the cable is welded to the sensor package there are two fibers. The "blue" fiber carries the desired light to the sensor, while the "red" fiber carries the remaining light on down the cable to the remaining sensors. We will now discuss each part of this package in turn.

Tube adapter: The part shown in light gray on the left is the tube adapter which joins the cable coming from the surface to the sensor package. The adapter is welded to the main sensor cavity or "Inconel sleeve" shown in green in the center of the package, and to the fiber cable on the left. The adapter is designed for ¼" (6.35 mm) fiber cable. The outer dimension of the adapter is 7/16" (11.11 mm).

Sleeve: The Inconel sleeve in light green in Fig. 16 contains the main portion of the sensor including the Si MEMS die. As mentioned previously, it is welded to the tubing adapter on the left. It is also welded to the membrane mount on the right. It has an outer diameter of 7/16" (11.11 mm).

Membrane mount: The membrane mount in gray on the right is welded to the sleeve on the left and to the remainder of the cable going on down to the next sensor on the right. This part has a ¼" (6.35 mm) hole on the right side for the cable tubing to slip into and a larger cavity on the left side and an outer diameter of 7/16" (11.11 mm). This larger cavity is open to the external environment via small holes drilled around its circumference. Two holes on opposite sides have been drilled in the first generation part.

Diaphragm: At the left end of the membrane mount is a 1 mil (25 μm) thick Inconel membrane forming the diaphragm between the external environment and the inner sensor die cavity. The Inconel membrane was purchased from Goodfellow Corp., part 957-903-92.[5] The membrane in the original point pressure sensor developed by the GE Measurement & Control business (Fig. 2) was e-beam welded to the mount, but neither an e-beam nor laser beam welder was available at the GE Research Center, so instead the membrane was hard soldered to the membrane mount as shown in Fig. 17. The solder is a Pb-In-Ag alloy #164 sold by Indium Corporation of America with a solidus temperature of 300°C.[6] The solder flux is Ruby Stainless Steel Flux.[7] This solder process was found to be very inadequate and may have contributed to ultimate failure of the sensor when subjected to high temperatures and pressures. Although the final part was He-leak tested and found to be leak tight, the Ag solder did not wet easily to the Inconel and the solder seal was weak.

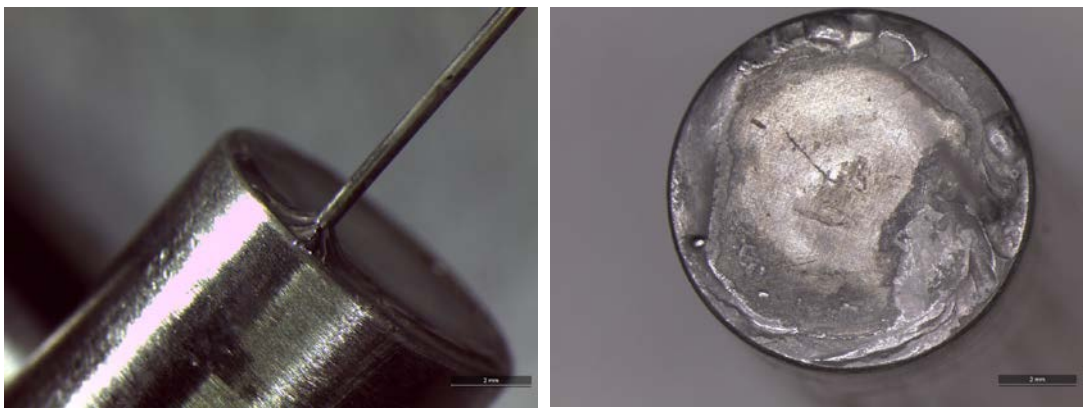

(a) (b)

Fig. 17: (a) Side view of Inconel tube adapter with hypodermic tube coming out of adapter on the same surface as the Inconel diaphragm. The silver solder has sealed the hypodermic tube. (b) Top view of Inconel membrane silver soldered to the adapter. The hypodermic tube is out of focus in this image but can be slightly seen as a blurred line starting from the right side of the image.

Invar rod: Inside the Inconel sleeve is a large cavity that holds the sensor die, the silicone oil, and an Invar rod. The Invar rod has a hole running through its center to carry one optical fiber to the sensor die. It also has a groove running down one side. A stainless steel tube used for hypodermic needles fits into this groove or slot. The purpose of the Invar rod is to balance the total thermal expansion of the components inside the Inconel sleeve cavity. In addition to the rod, these components are primarily the Si sensor die and the silicone oil. If the volume of the cavity is V_1, the volume of the Invar rod is V_2, the volume of the Si die (including the Si spacer) is V_3, and the volume of the silicone oil is $V_4 = V_1 - V_2 - V_3$, then the following thermal expansion criterion should be satisfied so that as the temperature of the sensor package increases, there is not undue pressure generated by the silicone oil inside the cavity,

$$\alpha_1 V_1 = \alpha_2 V_2 + \alpha_3 V_3 + \alpha_4 V_4 \tag{1}$$

where the α_1, …, α_4 are the coefficients of thermal expansion for the Inconel, Invar, Si, and silicone oil, respectively. If the diameter of the cavity in the sleeve is *d*, and the length of the cavity is L_1, then the length of the Invar rod is determined from Eq. (1). After simplification, Eq. (1) can be reduced to

$$L_2 = \frac{(\alpha_4 - \alpha_1) L_1 - \left(\frac{4 V_3}{\pi d^2}\right)(\alpha_4 - \alpha_3)}{\alpha_4 - \alpha_2}. \tag{2}$$

Of course, the thermal coefficients of expansion are themselves temperature dependent, so the average value of these coefficients over the temperature range of interest for the sensor should be chosen. Values used for the thermal expansion coefficents in this design are given in Table 2.

Table 2: Thermal expansion coefficients of various package materials

Material	CTE (10^{-6}/ °C)
Invar	1.0
Silicon	3.2
DURABOND 952	4.0
Inconel 625	13.1
EPOTEK 353ND	206.0

In the current package design, the cavity length inside the Inconel sleeve is 61.47 mm, leading to a Invar rod length of 56.95 mm.

Hypodermic tubing: This tube, which fits into the slot of the Invar rod, was purchased from Component Supply, part HTX-25T.[8] It has an O.D. of 0.508-0.521 mm and an I.D. of 0.292-0.330 mm so that the 250 μm diameter optical fiber can pass through the tubing. The tubing is hard soldered to the membrane mount at the surface of the membrane as shown in Fig. 17(a), and to the back side of the Inconel sleeve to make hermetic seals at both ends. Silicone oil is present around the tube which must not be allowed to leak into the cable.

Sensor die: The sensor die are shown in Fig. 18.

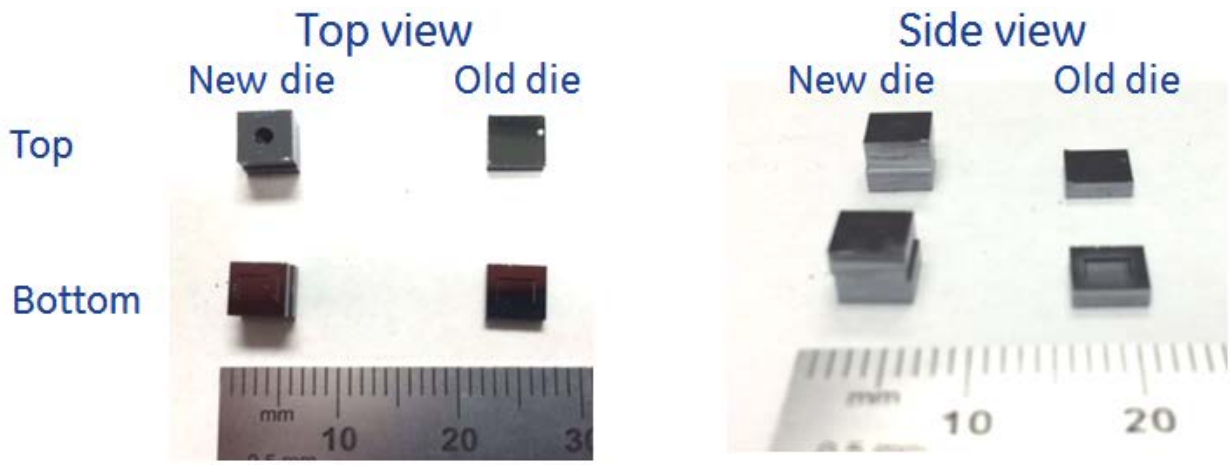

Fig. 18: Comparison of old die to new die fabricated for this project.

22 Si MEMS sensor die were earlier obtained from GE Measurement and Controls and are shown in Fig. 19. Complete frequency scans of the die were made from 7 kHz to 100 kHz to identify all resonant modes and measure their amplitudes. The results are shown in Fig. 20. The lowest resonant mode occurs at ~12 kHz and the highest one at ~93 kHz. There are four different resonator shapes in this collection of sensors, which explains the wide variety of resonant mode frequencies. The red boxes, however, are drawn around groupings of sensors that exhibit nearly the same frequencies corresponding to die with the same shape of resonators.

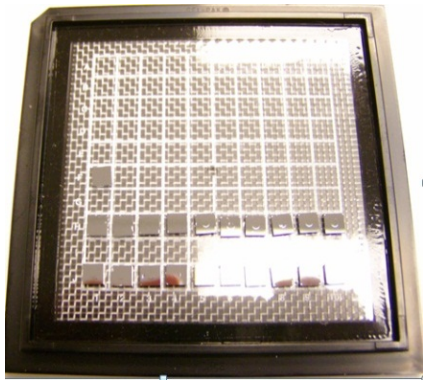

Fig. 19: 22 MEMs sensor die were obtained from GE measurement and Controls (GE M&C) in the first quarter. These die are designed for pressures of 3000 psi and will be used to develop the interrogation systems and package design.

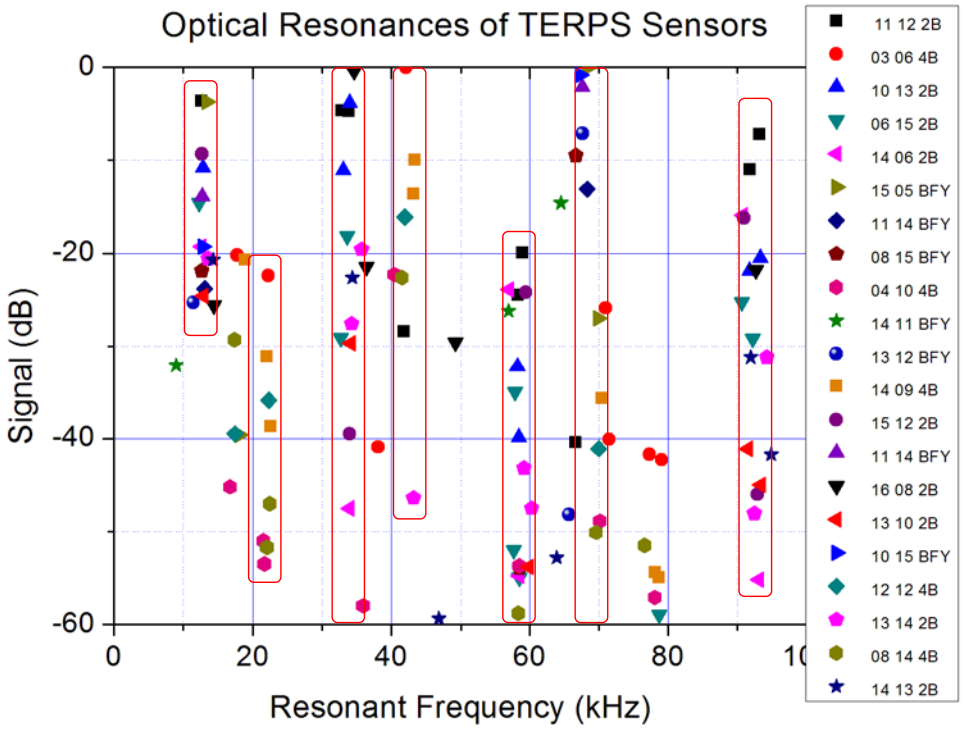

Fig. 20: Resonant frequencies for the Si die. One of the die did not exhibit any resonances. The other die generally exhibited multiple resonant modes. The resonant frequency is graphed along the horizontal axis and the measured signal amplitude is charted along the vertical axis for each sensor.

From this set of measurements, it is clear that multiplexing the sensors based on resonant frequency is indeed possible. As an example, sensors 15 05 BFY (12 kHz), 03 06 4B (43 kHz), and 11 14 BFY (68 kHz) are easily distinguishable. However, even sensors 14 11 BFY (65 kHz) and 11 14 BFY (68 kHz) are sufficiently separated in frequency to be easily distinguishable due to the very high Q and narrow linewidths of these sensors, so in principle it should be possible to multiplex ten or more sensors without difficulty by choosing die with different resonant frequencies.

Ceramic ferrule: The ceramic ferrules are sold by various vendors, including Thorlabs.[9] Ceramic ferrules for LC connectors (#CFLC128) have a 1.25 mm diameter, which will fit within the 1.6 mm hole in the Si spacer and provide a little room for optimizing the optical alignment of the fiber to the sensor die. However, it was found that the hole was not perfectly aligned with the resonator in the Si die, and the ferrules had to be machined to a smaller diameter in order to provide sufficient room for alignment. Moreover, as shown in Fig. 21, corrugations were also machined in the ferrule to provide a stronger attachment of the adhesives. Also, the corrugations created a visual aid for alignment of the ferrule with the Si spacer attached to the MEMS die.

The epoxy, ferrule, spacer and MEMS die were placed in an oven to cure the high temperature epoxy and allowed to set for several days.

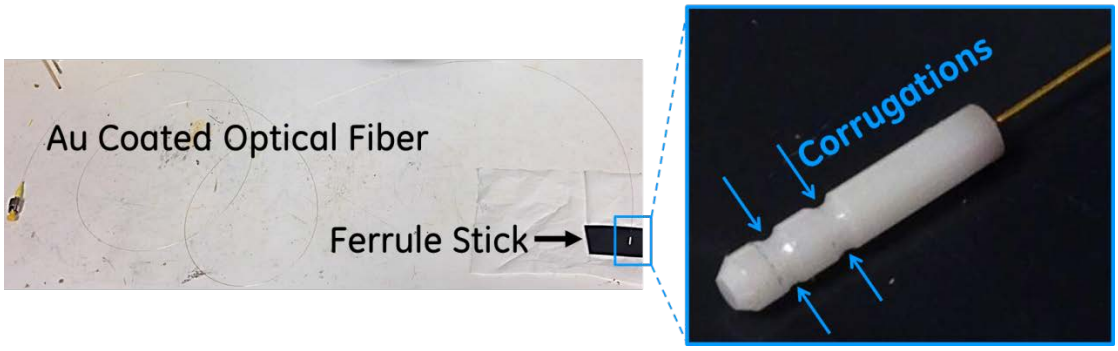

Fig. 21: Photograph of gold-coated fiber attached to a zirconia ferrule stick with corrugations.

Bonding of fiber into ferrule:

Gold-coated single mode (SM) optical fiber was purchased from Fiberguide. The optical fiber was epoxied into a ceramic ferrule stick. The gold coating on the tip of the fiber was stripped using a gold etchant #651818 from Sigma-Aldrich. Then the stripped fiber end was inserted into a zirconia ferrule stick and bonded using high-temperature epoxy, EPOTEK 353ND. After a heat cure, the tip of the ferrule stick holding the fiber was polished to create an optically flat surface. Fig. 21 shows a flat-polished fiber that is attached to a ceramic ferrule stick with corrugations machined into it.

Alignment of fiber to die: A picture of the experimental setup used for the alignment of optical fiber to MEMS sensor die as well as close-up photographs of the alignment station are shown in Figs. 22 and 23, respectively.

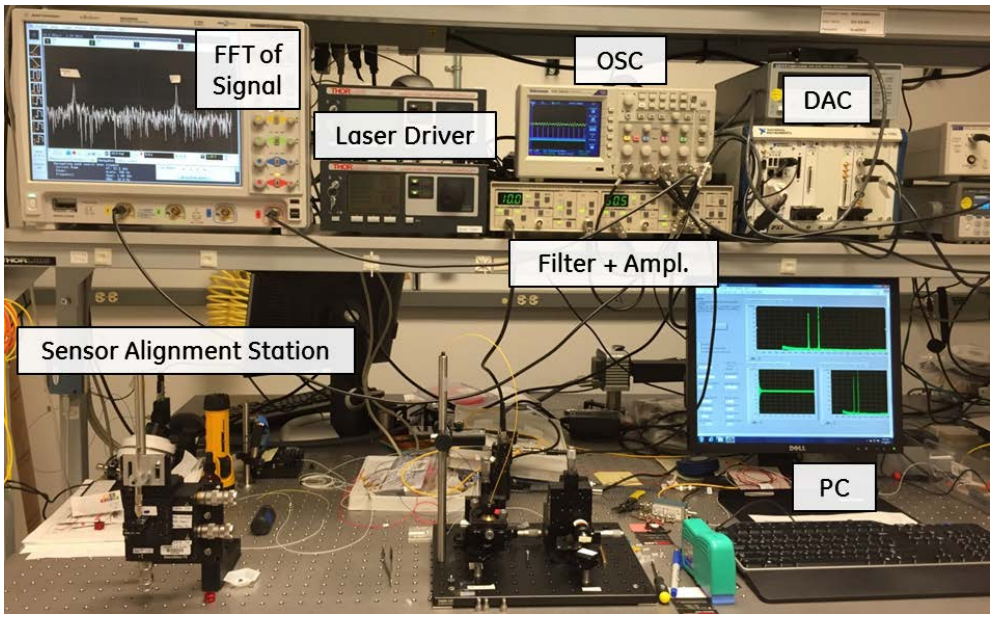

Fig. 22: Photograph of experimental setup used for the alignment of an optical fiber to a MEMS sensor die. The in situ alignment is performed using the pulsed laser interrogation technique.

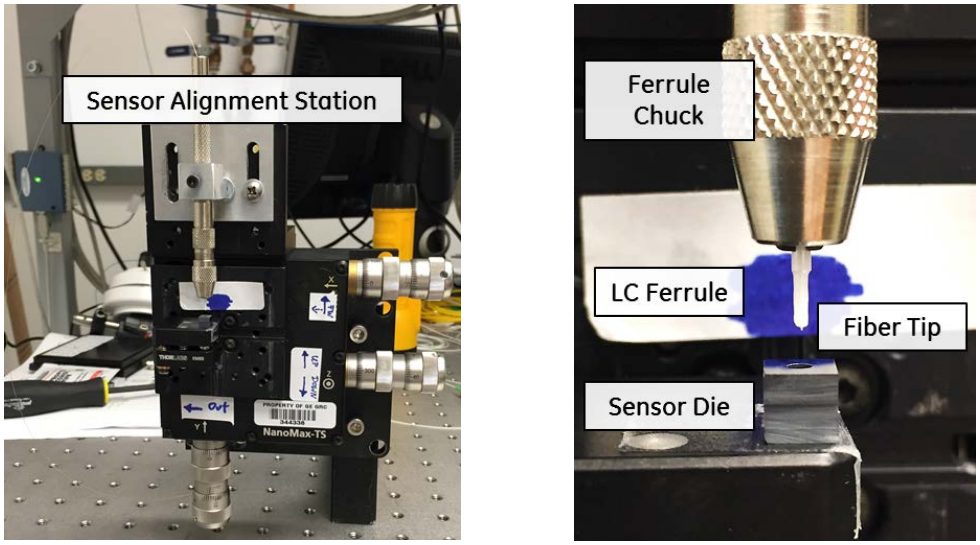

(a) (b)

Fig. 23: Photographs of sensor alignment station: (a) Micropositioner with x, y, z and tilt alignment capabilities and (b) close up photograph of sensor die, fiber tip, LC ferrule, and ferrule chuck.

The sensor alignment station is composed of a tilt station and a 3-axis micro positioner unit. The ferrule stick was firmly held in place by a ferrule chuck that was bolted to the micropositioner housing. The sensor die was attached firmly but not too tightly to the tilt station using double-sided sticky tape. The tilt station was mounted to the micro positioner platform to allow for

accurate alignment of fiber tip to the sensor die. The first 3.5 mm of the LC ferrule was reduced in diameter to about 800 μm, allowing more space for x, y alignment when inserted into the sensor die hole. The epoxy used as first interface between fiber tip and sensor die was EPOTEK 353ND. It was found to be optically transparent in the IR and provides a good index match between silica fiber and silicon chip. After a soft cure for 24 hours at room temperature, the sensor die and fiber ferrule were carefully removed from the alignment station and placed on a hot plate at 150°C for 3 hours. The coefficient of thermal expansion (CTE) of EPOTEK 353ND is 230 inch/inch/°C. This is much larger than the CTE of all the other components used in the sensor package (see Table 2). Because of this, DURABOND 952, a nickel based metallic adhesive, was used for the bulk mechanical attachment of the ferrule stick to the sensor die as well as for the attachment of the sensor die to the Invar rod. DURABOND 952 is formulated to have a very low CTE and is intended for bonding of metals, ceramics, and dissimilar materials for use up to 2000°F. The properties of the nickel-based DURABOND 952 are displayed in Table 3.

Table 3: Chemical and mechanical properties of DURABOND 952.

DURABOND	**952**
Use Temp °F	**2000**
Base	Nickel
Color	Grey
Density (# / ft^3)	180
Thermal Expansion (10^{-6}/°F)	4
Pot Life (Hours)	2
Bond Strength @ 200°F (psi)	400
Bond Strength @ 1200°F (psi)	1200
Components	2
Mixed Ratio (A / B)	100/120
Cure (@ R.T.)	24

The data sheet for Durabond 952 claims that this adhesive overcomes the brittle bonds observed in ceramic adhesives while offering some of the ductility and impact resistance associated with soldering and welding. During assembly, the metal particle grain size for the DURABOND 952 was discovered to be too large for dispensing through the opening of a small syringe needle. Therefore, the 952 adhesive was applied to the sensor with a small spatula. Even though the pot life is noted as 2 hours in the data sheet, the adhesive was observed to harden and form a thin film or “skin” within in a matter of a few minutes after mixing the two parts. The bond strength of 952 fully reaches its maximum only after one week of curing at room temperature. The metallic adhesive also becomes stronger at higher temperatures. A cross sectional sketch of the sensor die package with adhesives, ferrule stick, and gold coated optical fiber is shown in Fig. 24(a).

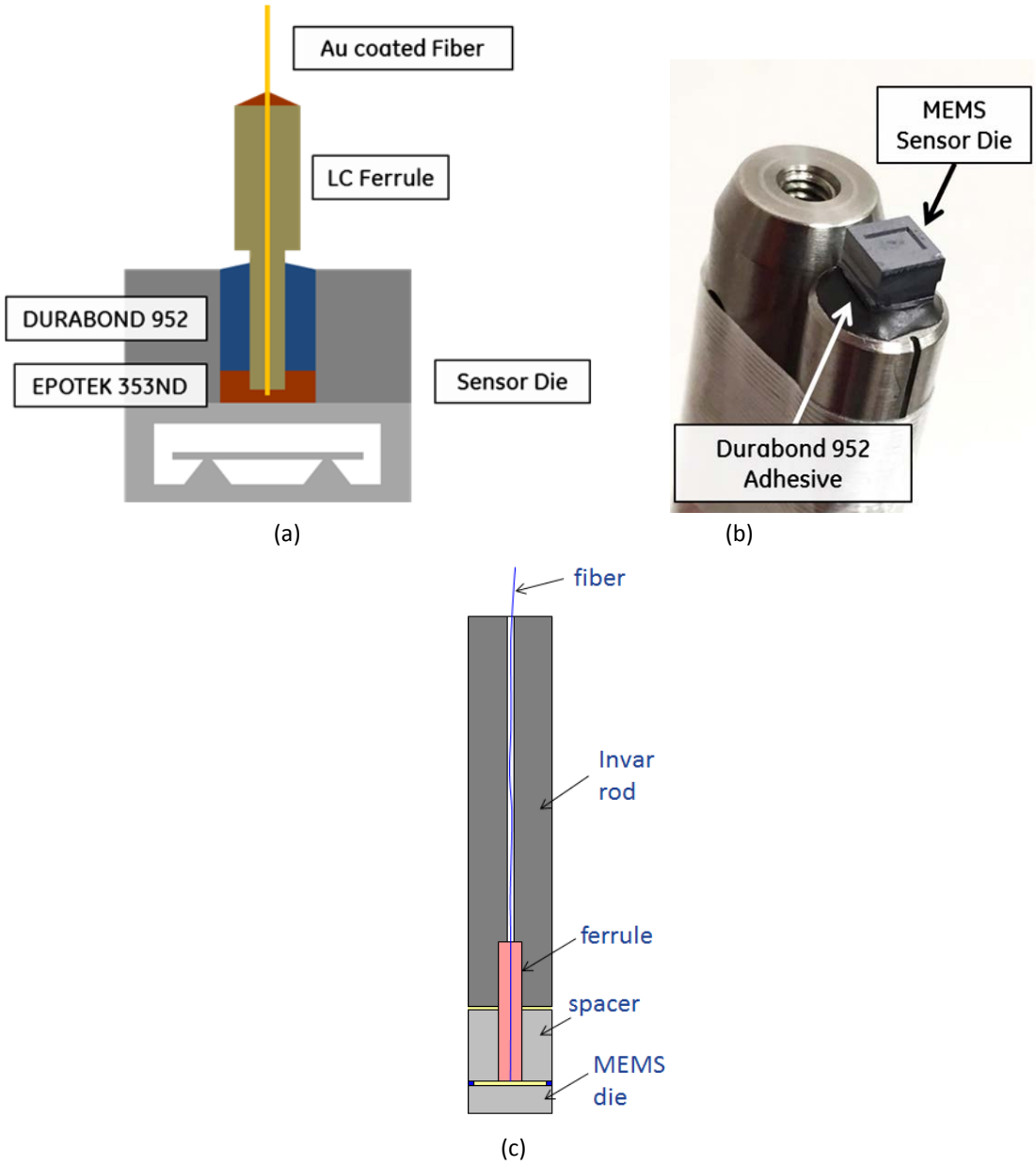

Fig. 24: (a) The fiber is bonded to the ceramic ferrule with Epotek 353ND, and bonded inside the Si spacer with the same epoxy. This high temperature epoxy is also relatively transparent to the near-IR light and provides a good index match to the glass fiber, thereby suppressing reflections at the tip of the fiber. The high temperautre ceramic adhesive Durabond 952 was then used to completely fill the space between the ferrule and the Si spacer and to bond the spacer to the Invar rod as shown in (b). The hole in the Invar rod for the fiber is also filled with high temperature adhesive to prevent access by the silicone oil.

The sensor die package was attached to an Invar rod using DURABOND 952, as depicted in Fig. 25. The sensor package must operate over a very wide temperature range, up to 250°C. The low CTE of the Invar rod inside the sensor cavity is used to offset the large CTE of the silicone oil to match the total volume change within the sensor cavity due to the CTE of the Inconel outer

package. Invar is an alloy of iron and nickel with extremely small coefficient of thermal expansion, ~3.6×10^{-6} K^{-1}. By adjusting the volume of Invar rod to that of the oil as discussed on p. 21 in the section on the Invar rod, the total volume expansion inside the Inconel cavity can be kept nearly the same as that of the outer Inconel package. Therefore, the stress on the diaphragm is minimized. The volume of Invar that is required is 20.5 times the volume of oil, so it is still important to minimize the oil volume in order to keep the sensor more compact.

The gold-coated fiber was funneled through the center hole in the Invar rod. The LC ferrule that was sticking out from the sensor package was placed into the center hole of the Invar rod and potted using DURABOND 952. As shown in Fig. 25(f), Kapton tape was used to close off the bottom side of the Invar rod to allow filling of the center hole with the 952 adhesive. Care has to be taken to not cover the fiber bypass groove or the oil dispense groove in the Invar rod. The Invar rod and the attached sensor package were then cured at room temperature for seven days.

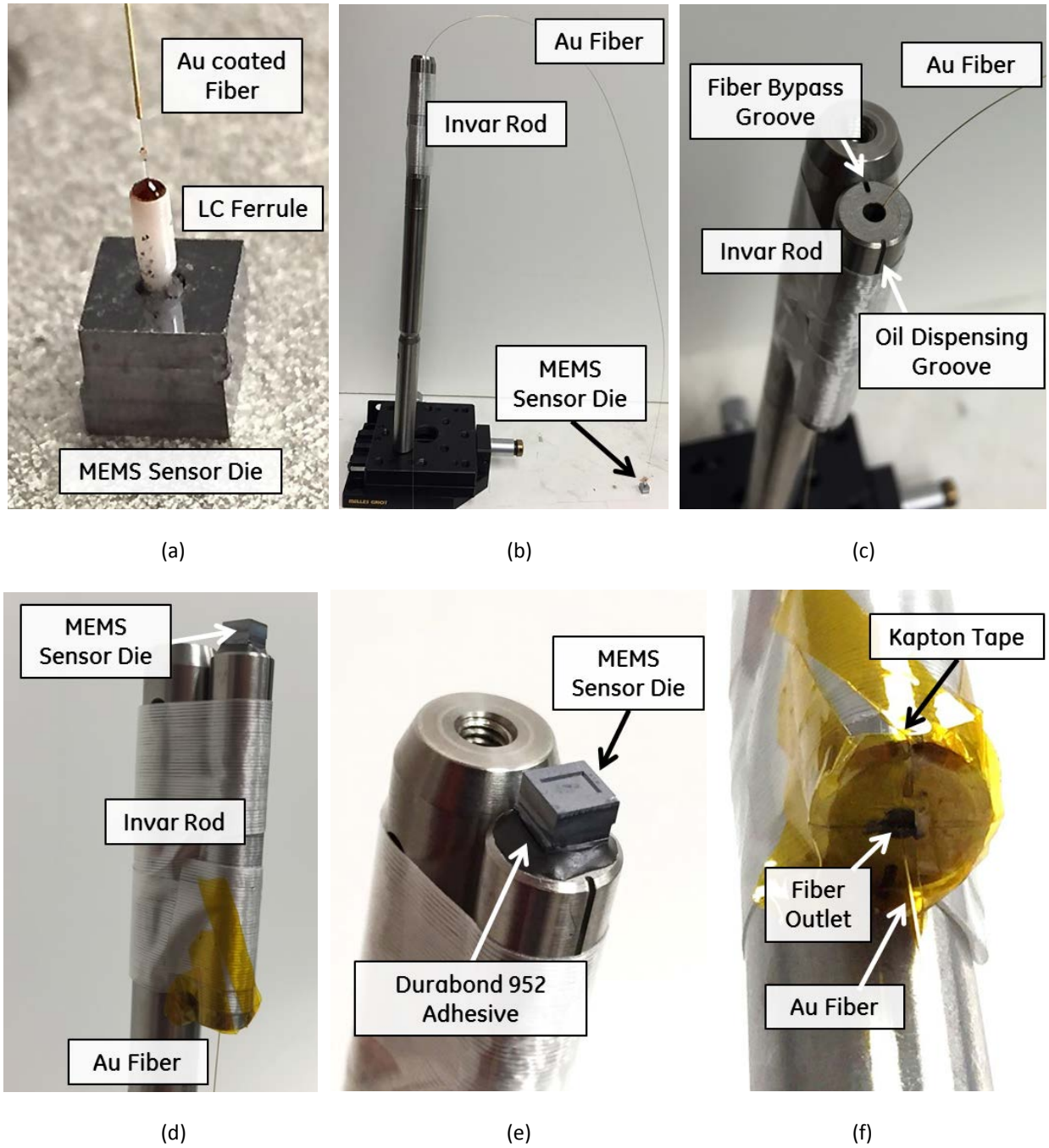

(a) (b) (c)

(d) (e) (f)

Fig. 25: Photographs showing procedure of attachment of sensor die package to Invar rod: (a) sensor die package, (b) fixture to hold Invar rod, (c) Au coated fiber funneled through center hole of Invar rod, (d) attachment of MEMS sensor die to Invar rod, (e) dispensing of DURABOND 952 around sensor die, and (f) filling center hole of Invar rod with DURABOND 952 using Kapton tape.

At this point, the Invar rod with attached MEMS sensor was inserted into the Inconel housing as shown in Fig. 26(b). A 1 mil Inconel membrane and the hypodermic tube had been previously hard soldered onto the membrane mount as shown in Fig. 17 and helium leak tested. The hypodermic tube is used as a bypass channel for the fiber which travels past the sensor and on

down the cable to the following sensors. It must be hermetically sealed to the sensor housing at both ends, however, to prevent either oil or fluid in the external environment from entering the sensor cavity or cable. The membrane mount was inserted into the Inconel sleeve as shown in Fig. 26(b). Unfortunately, when the sensor was assembled, the hypodermic tube was discovered to have shifted during soldering and to be too short to extend through the Inconel housing on the left.

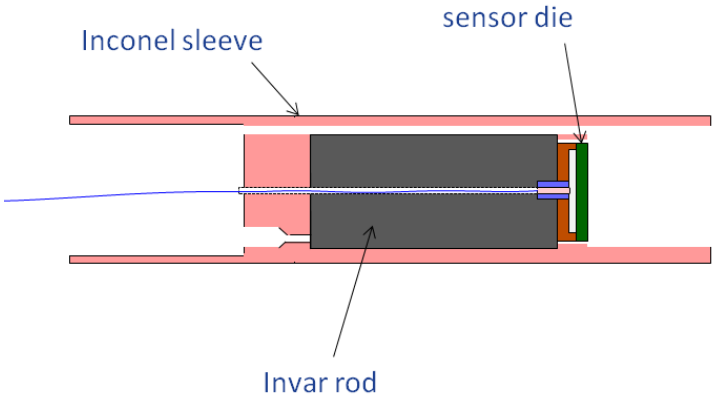

(a)

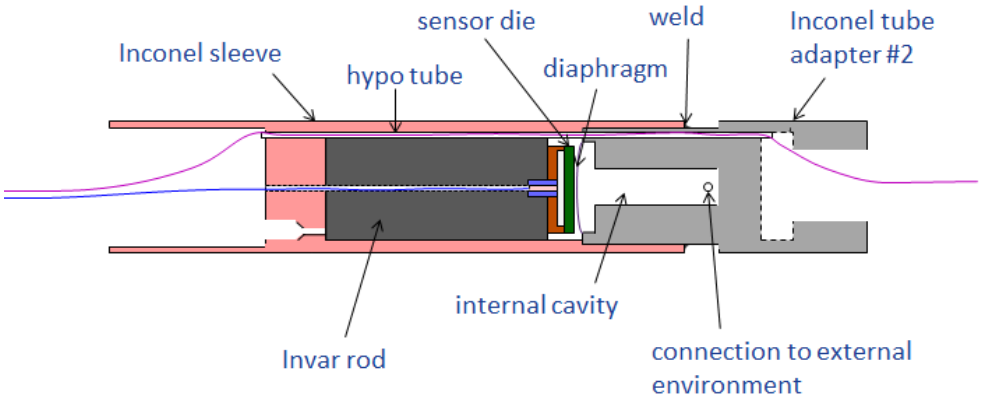

(b)

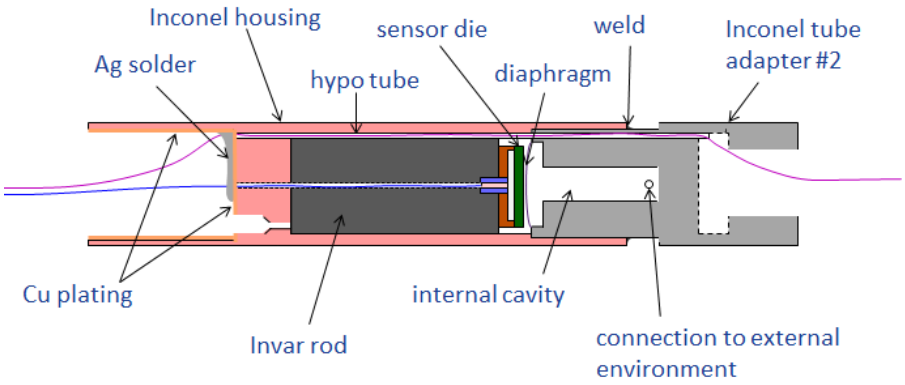

(c)

Fig. 26: (a) Sketch of insertion of Invar rod with bonded Si die into Inconel outer package. (b) Insertion of diaphragm into Inconel housing. (b) Insertion of Inconel tube with Inconel membrane and hypodermic tubing **into** outer housing. (c) Silver solder sealing Au-coated fiber, Cu-plated housing, and stainless steel hypodermic tube at left end of Inconel housing.

The membrane mount is then welded to the Inconel sleeve as shown in Fig. 26(d). The sleeve is cooled during the welding process so that the internal epoxy and hard solder joints are not damaged. The hypodermic tube is hard soldered to the copper plating inside the Inconel sleeve. It was previously hard soldered into the membrane mount as shown in Fig. 17. Again, the sleeve is cooled during the soldering process to maintain the integrity of the internal joints.

In the normal sensor assembly process, the hypodermic tube should be hard soldered to the Inconel housing on the left side to make a hermetic seal. Since the tube was too short for this to be done, in order to prevent oil from entering the hypodermic tube, DURABOND 952 adhesive was used to fill in the groove around the hypodermic tube in the Invar rod. Ultimately, during sensor testing, this remedy was found not to have worked and oil did in fact penetrate the hypodermic tube into the cable cavity below the sensor.

Brass plate: In the initial package design, there was a brass plate at the left side of the Inconel sleeve as can be seen in Fig. 27. This plate had two holes in it to allow the two fibers to pass through and was to be hard soldered onto the sleeve. To simplify the package assembly, however, the brass plate was replaced by simply electroplating a thin copper film on the inside of the sensor housing. Both fibers are standard 125 μm single mode fiber with an outer gold coating, purchased from Fiberguide.[10] The gold coating allows them to be soldered to the copper plating to make a hermetic seal as shown in Fig. 26(c). The gold-coated fiber is also rated to temperatures up to 700°C. Prior to feeding the fibers into the package, the hypodermic tube should be hard soldered to the copper electroplate inside the Inconel sleeve.

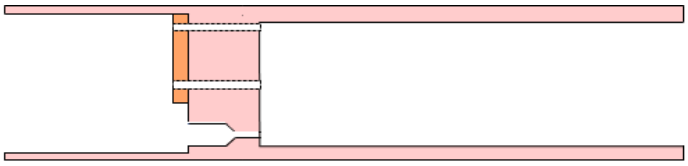

Fig. 27: Brass plate in original sensor package design has been replaced by a copper eletroplate inside the Inconel sleeve.

Gold-coated fiber was inserted through the hypodermic tube. Hard solder was obtained from Indium Corporation of America #151 solder paste specifically for stainless steel soldering, and had a melting temperature of 287°C. It was used to seal the gold-coated bypass fiber coming out of the left side of the Inconel housing to the Cu-plated housing as shown in Fig. 26(c). This solder was also meant to provide a hermetic seal for the gold-coated fiber emerging through the center of the Inconel housing from the sensor die. Unfortunately, visual inspection after the soldering seemed to indicate that the fiber from the sensor coming through the center of the housing had not been successfully soldered. Therefore, an additional layer of DURABOND 952 adhesive was placed into the end of the housing near the end of the sensor assembly process to ensure this fiber was also sealed.

Silicone oil: Surrounding the sensor die is high temperature silicone oil. DPDM-400 from Clearco Products with a refractive index of 1.505 and an operating point up to 315°C in a closed system with a coefficient of thermal expansion is 7.3×10^{-4} was used for this sensor.

The sensor die cavity must be filled with this silicone oil. Prior to filling with oil, the cavity must be evacuated. A photograph of the vacuum bell jar with mounted sensor package and silicon oil in aluminum foil pocket is shown in Fig. 28. The sensor package was evacuated overnight.

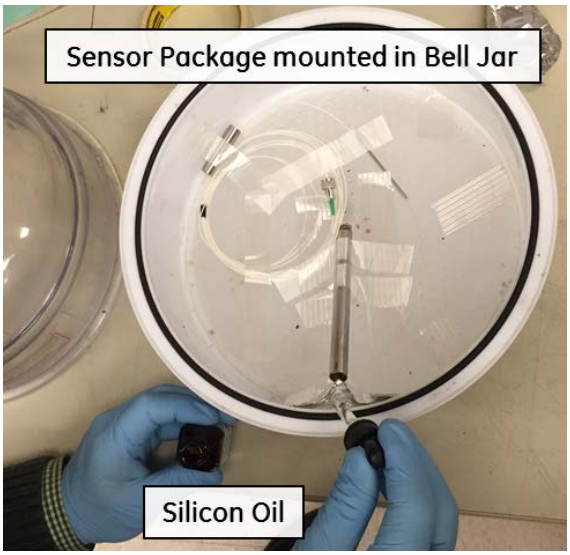

(a)

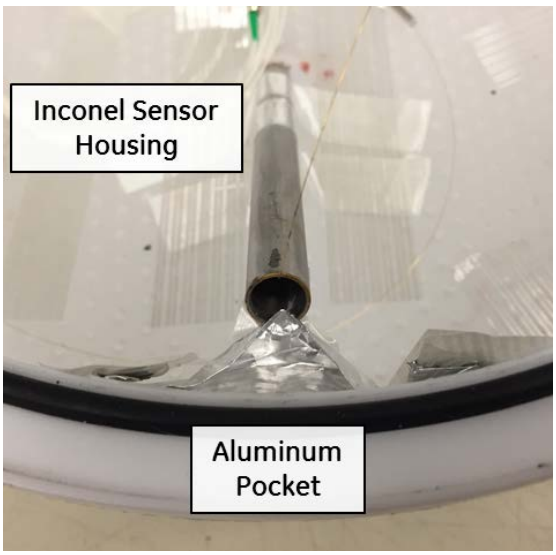

(b)

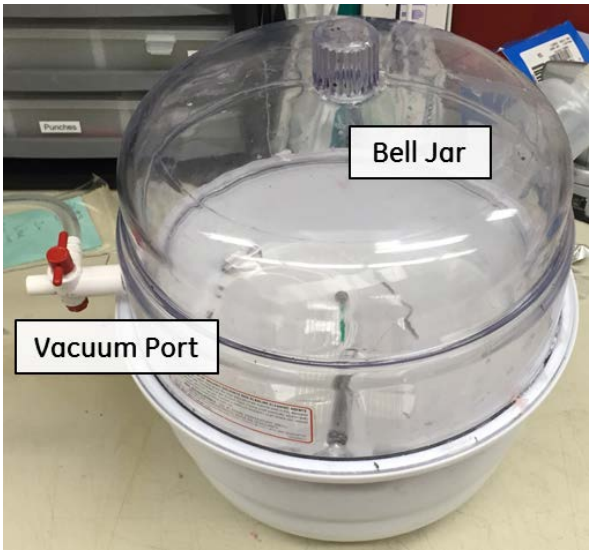

(c)

Fig. 28: Photographs showing filling of air gap between MEMS sensor die and diaphragm with silicon oil: (a) mounting of sensor package in vacuum bell jar, (b) filling of aluminum pocket with silicon oil, and (c) pumping down vacuum bell jar before tilting setup to flow silicon oil into sensor housing.

The sensor die cavity with filled with silicone oil. At this point, a layer of DURABOND 953 was applied over the two fibers and the set screw inside the Inconel housing as previously mentioned to make doubly certain that all three ports into the housing on the left side were hermetically sealed. Then the Inconel tube adapter in Fig. 16 was welded to the Inconel sleeve as shown in Fig. 30 and the sensor was then ready for being welded into the cable.

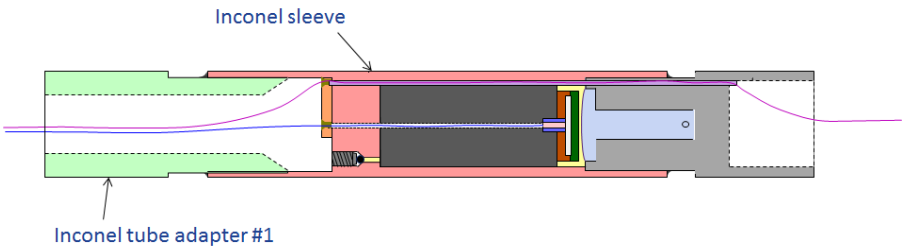

Fig. 30: Welding of tube adapter to sleeve.

The completed MEMS sensor was attached to a protective Inconel tube. The Inconel tube housed a fiber optical cable to which additional sensors could be multiplexed via power splitters or WDMs. To demonstrate multiplexing capabilities of the distributed sensor cable, a second MEMS sensor was attached using a 50/50 fiber optical power splitter (Fig. 31). Photographs of the completed multipoint sensor cable are shown in Fig. 32. The first MEMS sensor on the sensor cable had a sensor die with a high-Q cavity (~8000) and, therefore, provided a high signal-to-noise ratio (SNR) during measurement. However, this sensor die was from an earlier project and was only designed for maximum pressures of 3000 psi. The second MEMS sensor was made with a sensor die specifically fabricated for this project with a maximum pressure rating of 10,000 psi. However, all of these high pressure sensor die had much lower quality factors (~200 to 1100), with corresponding lower SNRs. The performance of each of the multiplexed MEMS sensors, individually as well as combined, is discussed in greater detail in the section of this report on Task 4, page 90.

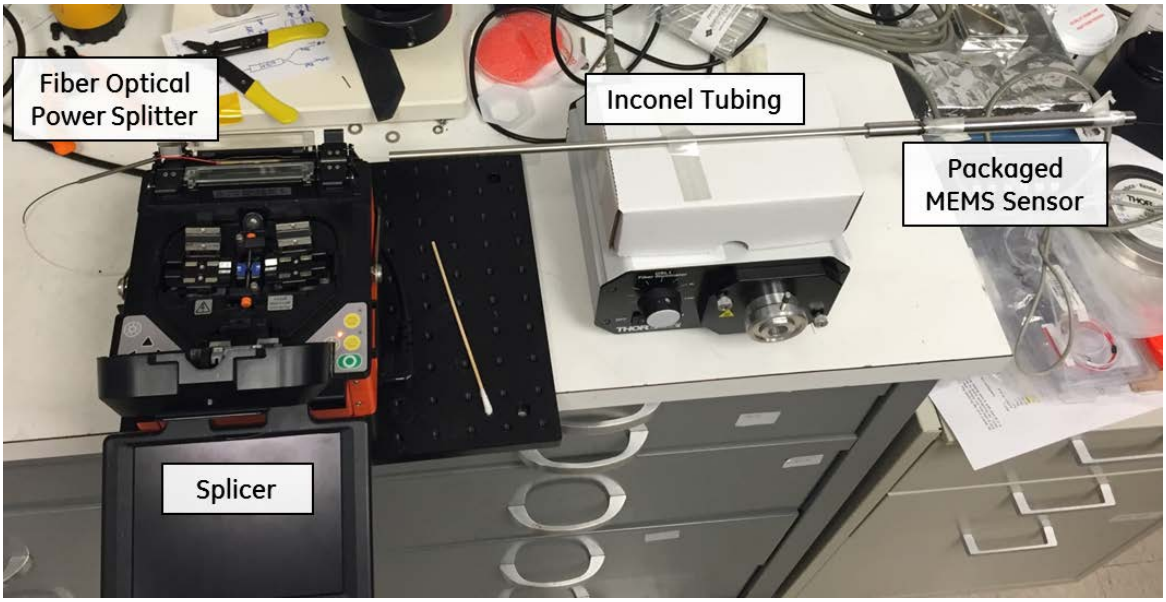

Fig. 31: Attachment of protective Inconel tubing to packaged MEMS sensor and splicing of a power splitter to the fiber optical cable.

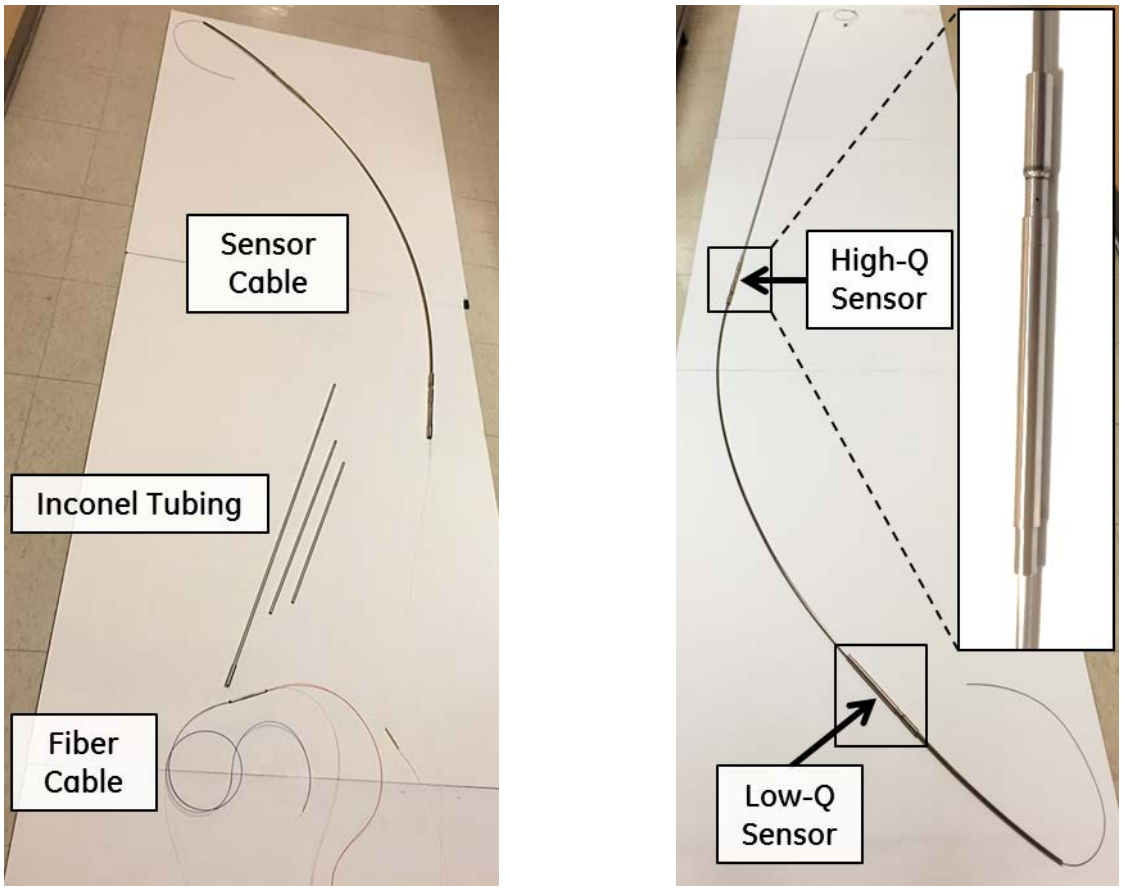

(a) (b)

Fig. 32: Photographs of sensor cable assembly: (a) optical fiber cable inserted into protective Inconel tubing and (b) completed sensor cable with two multiplexed pressure and temperature sensors using a single fiber input/ output.

This completes the description of the assembly process for the sensor package. When testing the completed sensor on the sheave tester as described in Task 4B, the weld connecting the cable to the sensor package cracked. Apparently, the welding process significantly weakens the cable. Hence, a steel insert like that shown in Fig. 33 will be necessary in future package-to-cable welding to prevent bending of the cable at the welding point.

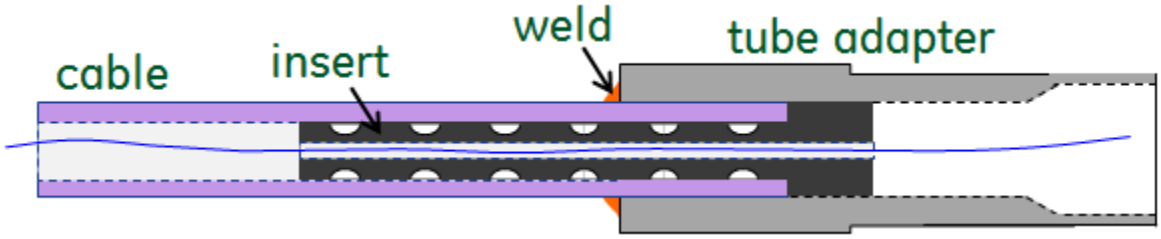

Fig. 33: Joint insert for connecting for connecting cable to sensor package that ensures that the cable does not bend at the position of the weld.

C. Splitter package

As mentioned in the previous section, there are two fibers entering the sensor die package. The single fiber coming down the cable has to be split prior to entering the sensor die package. In principle, the splitter could also be located within the sensor die package, but it was decided to place the splitter within its own package in order to reduce the length of each package so that the cable would more easily wrap around the sheaves. It is envisioned that there will be ~1 m length of cable tubing separating the two packages as shown in Fig. 34.

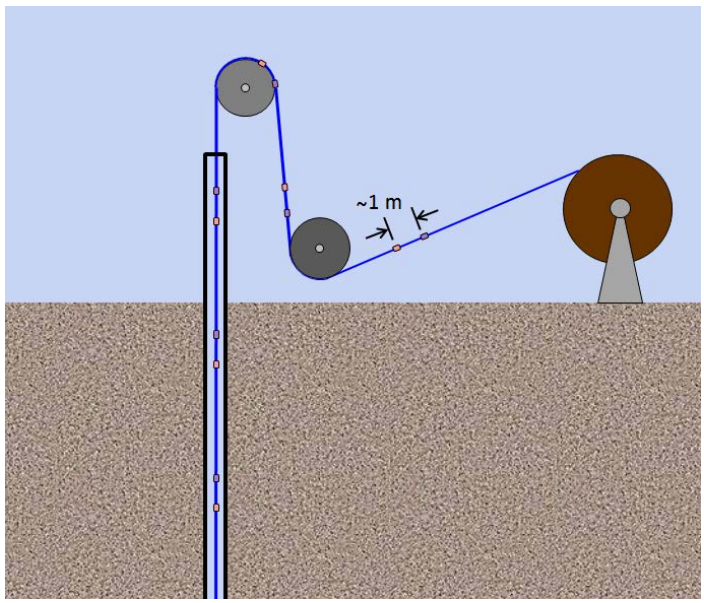

Fig. 34: Deployment of fiber cable in which there are separate packages for the splitter and the sensor die at each measurement point separated by a small section of cable to allow the cable to more easily roll over the sheaves.

The simplest way to split the light is to use either a wavelength division multiplexer (WDM) or a coupler/splitter. High temperature WDMs and splitters are sold by Comcore[11,12] and Gould.[13] Selection of the appropriate technique for splitting the light at each sensor should be guided by the following considerations.

1. WDMs

WDMs have two distinct advantages over splitters. First of all, they split nearly 100% of the light of a specific wavelength out of the fiber into one of the output fibers towards one sensor, while passing nearly all the light of other wavelengths into the other output fiber towards the remaining sensors. The reverse is also true: the WDM recombines the different light wavelengths very efficiently. As a result, if there are ten different sensors on the fiber cable, each one will receive and reflect nearly 100% of the specific wavelength of light associated with each WDM. The number of wavelengths that can be split/recombined depends on the type of WDM. "Dense" WDMs used in the telecom industry typically divide the wavelength band between 1520.25 nm to 1577.03 nm into 72 different channels.[14] Additional channels can be

obtained by extending the wavelength range into other telecom channels. The telecom channels are generally divided as follows:

- O-Band:1270nmto 1370nm
- E-Band:1371nmto 1470nm
- S-Band:1471nmto 1530nm
- C-Band:1531nmto 1570nm
- L-Band:1571nmto 1611nm

So, there are clearly many more individual channels available beyond the standard 72 channels.

"Coarse" WDM in the telecom industry refers to a wavelength division that is spread over fewer channels with broader linewidths. These are less expensive than DWDM and would be more likely to be applicable over an extended downhole temperature range. There are 18 CWDM channels between 1270 nm and 1610 nm spaced at 20 nm intervals as shown in Fig. 35.

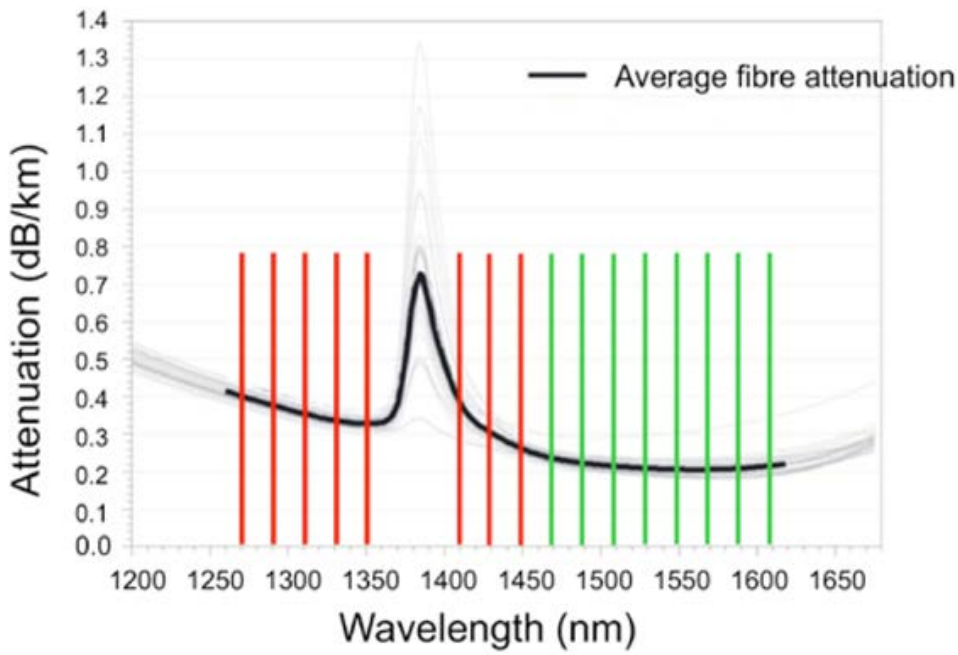

Fig. 35: Spacing of CWDM channels in wavelength.[15]

Some of these channels occur in wavelength regions where there is enhanced OH optical absorption. Hydrogen darkening is another issue that occurs when hydrogen diffuses over time into the core of the fiber and chemically combines with dangling bonds in the silica arising from Ge-doping that is sued to increase the refractive index of the core. In general, for downhole applications it is appropriate and necessary to use "pure-silica core" fiber in which there has been no Ge-doping. This fiber has been especially developed to resist increased absorption from hydrogen, though it does still exhibit some darkening that is generally reversible when the hydrogen source is removed, indicating that the darkening is not a result of chemical

recombination of the hydrogen with the silica. If the OH absorption band is avoided, there are still eight DWDM channels that are available at the wavelengths shown in Table 4.

Table 4: Wavelengths of several DWDM channels

DWDM Channel	Wavelength
47	1539.77 nm
49	1538.19
51	1552.52
53	1550.92
55	1549.32
57	1547.72
59	1546.12

The second major advantage of WDM light splitters over power splitters is that the light returning to the surface for detection can again be split by appropriate WDMs to be detected without interference from signals by other sensors. In other words, by using WDMs for light splitting, more light is returned from each sensor, and the light can be separately detected for each sensor. This should provide a much higher signal-to-noise ratio than when power splitters are used for multiplexing.

There are also several disadvantages of using WDMs for light splitting. First of all, a separate laser light source is required for each sensor or a tunable laser may be more cost effective if there are many sensors. A tunable laser can be scanned to address each sensor separately and can also overcome any problems with wavelength drift of the downhole WDMs due to temperature or aging. However, the sensors cannot be addressed simultaneously, which is probably not an issue if measurements need to be repeated infrequently (i.e., on an hourly or daily basis).

2. Power splitters/couplers

Multiplexing can also be accomplished using power splitters/couplers. These components also have some advantages and disadvantages relative to WDMs. A major advantage is that a single light source can be used, thereby making the overall system cost potentially much lower. However, the light source must have enough power so that it can provide sufficient SNR from each sensor. High power laser diodes are readily available and though they are more expensive than their lower power counterparts, they are still much less expensive than tunable lasers.

Couplers/splitters are generally available in a wide variety of coupling ratios. For example, to place ten sensors on a single fiber, we would ideally want splitting ratios in the sequence 10/90,

11.1/88.9,12.5/87.5, etc. until the ninth splitter is 50/50. In this manner, 10% of the light injected into the fiber (minus any losses in the fiber and splitters) is split off to each sensor. The fractional split ratios are not standard, however. Commercial, off-the-shelf (COTS) components more typically are available in decimal ratios of 10/90, 20/80, 30/70, ..., 50/50. Therefore, using these COTS values, one might design a cable with the splitter ratios found in Table 5. In this case, the amount of power on each sensor varies from 7.8% to 14.5%.

Table 5: Example of splitter ratios to address 10 downhole sensors

	Split ratio	**Light to sensor**	**Light to detector**
1	10/90	0.010	0.0100
2	10/90	0.090	0.0081
3	10/90	0.081	0.0066
4	20/80	0.145	0.0210
5	20/80	0.117	0.0137
6	20/80	0.093	0.0087
7	30/70	0.112	0.0125
8	40/80	0.105	0.0110
9	50/50	0.078	0.0061
10		0.078	0.0061

Probably more critical than the fraction of the light power that gets delivered to each sensor is the fraction which returns to the surface. The surface fraction is obtained simply by squaring the fraction of the light delivered to the sensor. If we deliver 10% of the light to the sensor, then only 1% at most gets returned to the surface. In the example above, the last column shows the fraction of light returning to the surface, and this ranges from 0.61% to 2.1%. This calculation illustrates one of the primary disadvantages of using splitters for multiplexing – very little of light injected into the fiber actually returns to the surface for detection and measurement. The amount of light available for surface measurement is inversely proportional to the number of sensors on the cable. If only four sensors are required, then even the “conventional” dual laser interrogation technique has been found suitable for the measurement. However, using more sensors on a fiber than this may be impossible using power splitting multiplexing by itself.

One final advantage of using splitters for multiplexing is that this approach is compatible with the interferometric interrogation technique. The interferometric interrogation technique makes use of a broadband light source for readback. The bandwidth of the light source is typically ~50 nm in order to ensure that the light reflecting from various surfaces in the sensor is incoherent. In particular, there are strong reflections from the outer surface of the sensor die cap, the inner

surface of the sensor die cap, and the resonator inside the sensor die itself. The optical path difference between the resonator and the inside surface of the sensor cap is ~200 μm. The coherence length as a function of bandwidth is given approximately by the equation

$$L = \frac{2\left(\ln 2\right)\lambda^2}{\pi\, n\left(\Delta\lambda\right)} \tag{3}$$

where n is the refractive index of the medium. A 50 nm broad light source at a wavelength of 1550 nm in vacuum has a coherence length of ~21 nm. Therefore, the optical path distance between the resonator and cap is an order of magnitude greater than the coherence length of the broadband source. By using different cap thicknesses and cap-to-resonator distances for each sensor, it is possible to interrogate just the desired sensor by adjusting the path difference of the interferometer to select the appropriate path difference for that sensor. In that case, as long as the other sensors have gaps that are well outside of the coherence length of the broadband source, there will be no interference at the detector from light reflected by the resonator and another surface in the sensor and thus there will be no detectable signal at the detector from the other sensors.

The interferometric approach, therefore, relies on the incoherence of the broadband source to enable sensor multiplexing. The broadband source, however, cannot be used with either DWDM or CWDM components due to their limited bandwidth. The pass band of CWDM components is typically ~13 nm,[16] which corresponds to a coherence length of 80 μm. This long coherence length in turn would require differences in the resonator-to-cap distance for each sensor of several times this length in order to multiplex sensors without excessive interference and crosstalk, which quickly becomes impractical.

3. Combination power splitters/couplers

There is a third approach to multiplexing that combines both WDMs and splitter/couplers. Different wavelengths of light are used for reading each sensor, requiring different lasers or a tunable laser as before. However, driving the sensor at its resonant frequency is accomplished with a single laser that is multiplexed by power splitters rather than WDMs. An example of this approach is shown in Fig. 36. The light splitter for each sensor (contained within the dashed lines) is no longer a single component but instead contains multiple components.

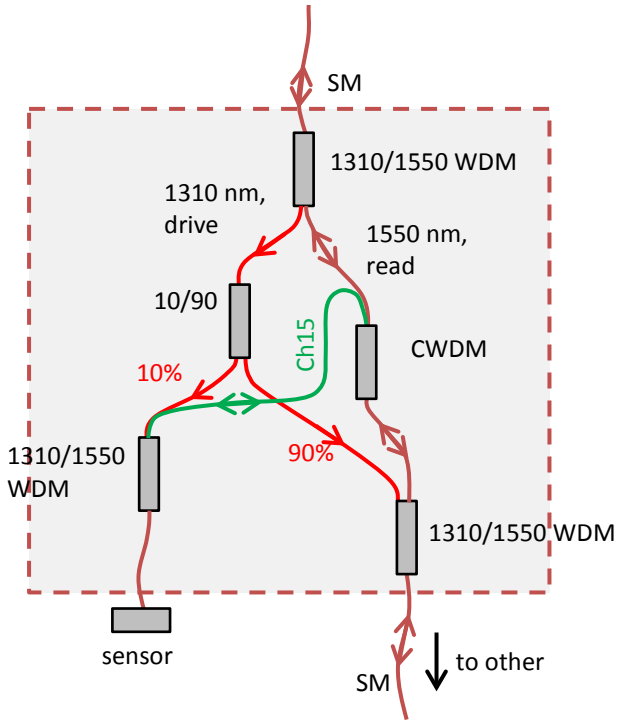

Fig. 36: Example design for multiplexing sensors.

As the light enters the multiplexer, it first encounters a broadband WDM. This serves to separate the read laser light (which is composed of multiple wavelengths in the C band in this example) from the drive laser light (at 1310 nm in this example). The drive laser light goes on to an appropriate power splitter. The read laser light continues on to a CWDM. *All* of the light for a *single* wavelength of a *single* read laser that is meant for this specific sensor is split off by the CWDM. In the example in Fig. 36, the light in channel 15 at 1551 nm is split off towards the sensor. The rest of the laser light in the C band at other wavelengths from the other read lasers and for the other sensors continues on down the fiber at the other output of the CWDM. If desired, the 10% drive laser power and specific read laser channel may be recombined as shown in Fig. 36 by another WDM on the bottom left before exiting the total component in a single SM (single mode) fiber to the sensor. However, this WDM may not be required if the sensor is designed to accept two separate fibers for drive and readback. The 90% drive laser power, on the other hand, is recombined with the remainder of the read laser wavelengths by another broadband WDM on the bottom right in Fig. 36 and the recombined laser light is sent on down the single SM fiber towards the next sensor. Although the entire component appears complex when split into its multiple subcomponents, it should be possible to assemble this as a single component.

The design shown in Fig. 36 is not unique. Another way of arranging the components is shown in Fig. 37.

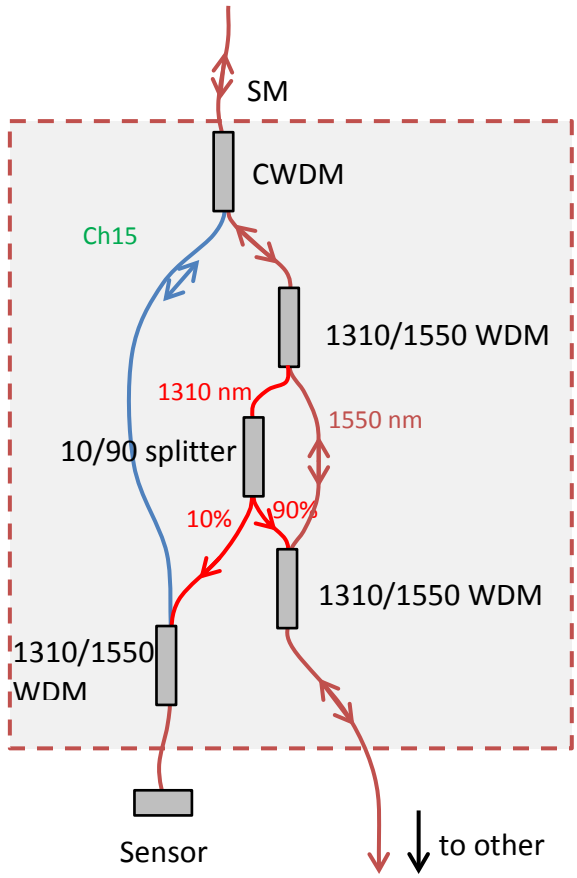

Fig. 37: Second example design for multiplexing sensors.

Once the type of multiplexer, a WDM, a splitter, or a combination, has been selected, then the component needs to be placed within a package as shown in Fig. 38.

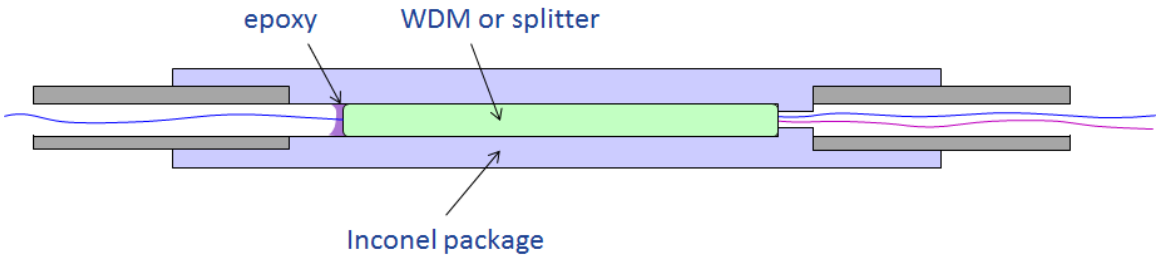

Fig. 38: Package for WDM or splitter. The Comcore high temperature WDM has a diameter of 3 mm and length of 54 mm. Including ~25 mm for ¼" tubing insertion at both ends, the total length of this part will be ~110 mm. A plug of high temperature epoxy is added after the WDM has been inserted to keep the WDM from moving.

Task 3: Design of Readout System

Measuring signals from multiple sensors on a single optical fiber requires a specific method of multiplexing, which may involve laser wavelength, sensor vibrational frequency, and/or sensor geometry in a manner that will be described. Different multiplexing techniques have various advantages and disadvantages. In some techniques there may be ample readback and drive laser power available for each sensor, but the optical coupling downhole to each sensor may be rather complex, or the interrogator may require separate lasers for each sensor, thereby increasing the complexity and cost of the system. On the other hand, some multiplexing techniques may enable the use of just one or two lasers for interrogating multiple sensors, but in this case there may be enhanced readback noise levels in the reflected light from the sensors as well as high power laser requirements which will ultimately limit the number of sensors that can be multiplexed. The best interrogation system for a given application will likely depend on the number of sensors and will not necessarily be the best system for every situation.

A. "Conventional" interrogator

The original interrogation scheme used for a previous project that developed a fiber optic interrogator for a *single point* pressure sensor is shown in Fig. 39 and requires two separate lasers operating at different wavelengths. The drive laser, which is shown in this figure at a wavelength of 1310 nm, is modulated at the vibrational frequency of the resonator in the sensor. The resonator absorbs some of this optical energy and is thermally excited and begins vibrating at the frequency of the drive laser. A second laser, which is shown at a wavelength of 1550 nm in this figure, is used to measure the vibrational frequency of the sensor. In particular, the resonator forms one side of an optical cavity with the other reflecting surfaces in the optical beam path. These surfaces are typically the top and bottom surface of the silicon cap of the sensor as shown in Fig. 40.

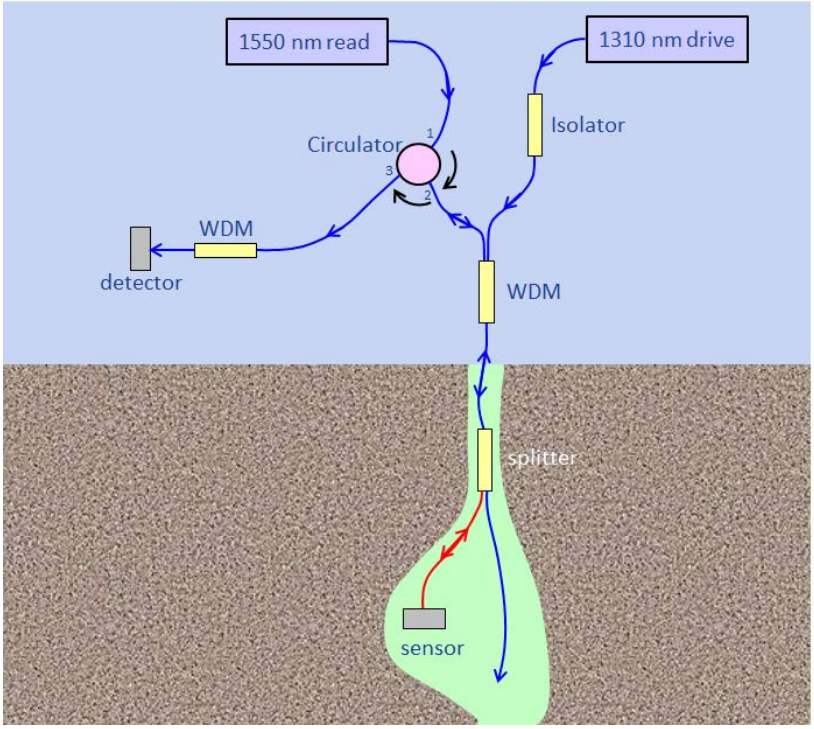

Fig. 39: Conventional sensor fiber optic interrogator design using two lasers.

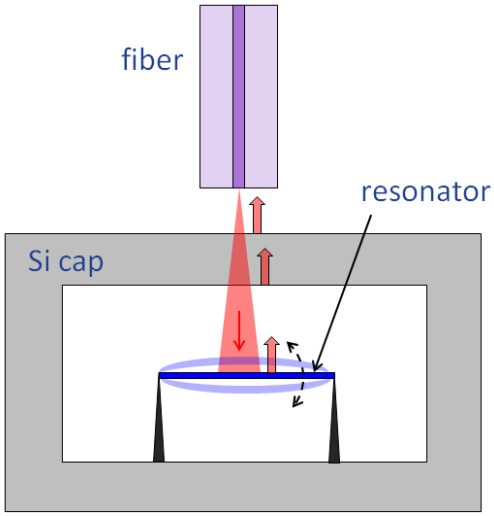

Fig. 40: Illustration of sensor optical cavity. Light emitted from the fiber is reflected at the top and bottom surfaces of the sensor cap as well as the vibrating resonator.

The vibrating cavity causes the intensity of the reflected beam to be modulated at the frequency of vibration. By using the telecom wavelengths of 1550 nm and 1310 nm for the lasers, the light is efficiently transmitted through the Si cap, because these wavelengths lie below the bandgap of silicon where it is substantially transparent. Changes in the external pressure cause the

vibrational frequency of the sensor to shift. A phase locked loop (PLL) or lock-in amplifier[17] is used to detect the modulated readback signal from the detector[18] – both its amplitude and its phase as shown in Fig. 41.

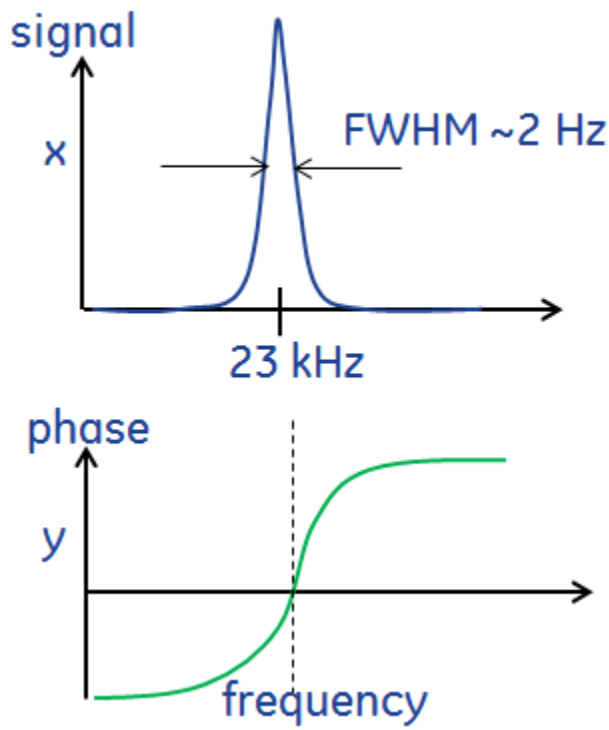

Fig. 41: Signal amplitude and phase are measured by a phase locked loop in the conventional interrogator approach. The phase signal provides the error signal for the feedback loop to keep the drive signal center at the resonant frequency of the sensor.

As the resonant frequency of the sensor shifts, the phase of the detected signal begins to quickly change also. Depending on the direction of the frequency shift, the phase either increases or decreases and, therefore, provides an error signal. The error signal is conditioned appropriately with filters and gain stages and then fed into a voltage controlled oscillator (VCO) which is used to modulate the drive laser. The lock-in amplifier conveniently includes a VCO. Thus, the frequency of the drive laser is locked to the vibrational frequency of the sensor. The frequency of the VCO is monitored and recorded by a PC to determine the vibrational frequency of the sensor and thereby log the pressure in the local environment of the sensor. The feedback circuit that was developed for this interrogation approach is shown in Fig. 42.

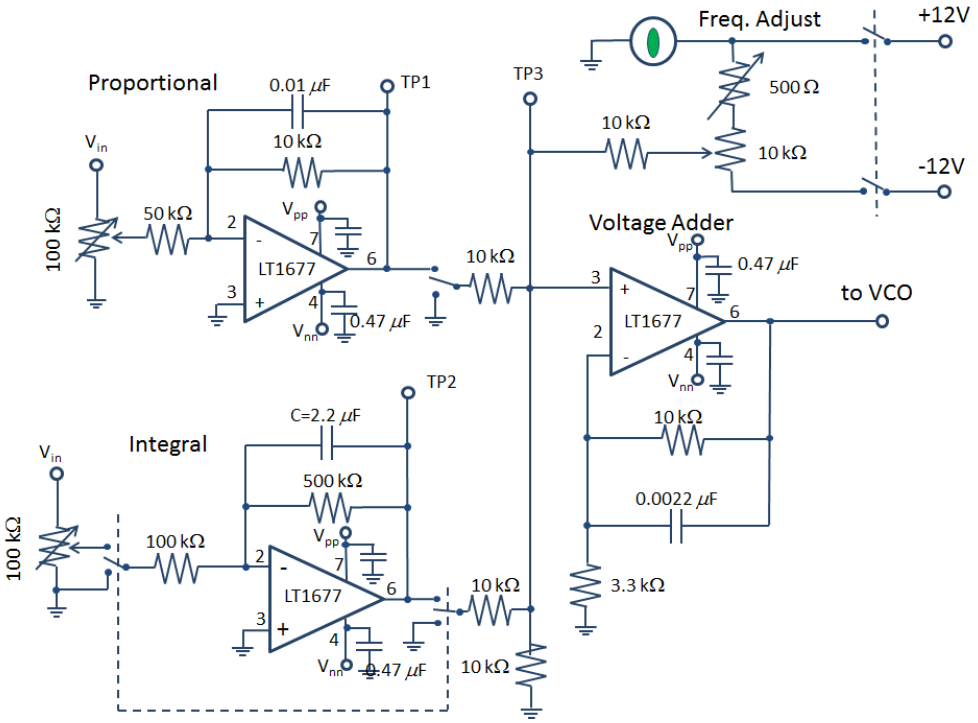

Fig. 42: Schematic of feedback circuit for VCO control of drive laser frequency. V_{in} comes from the *y* output of the SR530 lock-in as described in the text. The output of this circuit controls the VCO of the Stanford Research lock-in amplifier, SR530, which in turn is used to modulate the intensity of the drive laser at the resonant frequency of the sensor.

With two lasers at different wavelengths it is difficult or impossible to use wavelength for multiplexing sensors as WDMs are typically designed to split only a single wavelength channel from a band of wavelengths. However, if light splitters/couplers are used instead of WDMs, then it is possible to split off a portion of the total light intensity from both the drive and readback lasers at each sensor. There are some distinct disadvantages of doing this. First of all, the total laser power from each laser must be much larger to excite and readback the signals from all sensors than if all the light could be directed separately to each sensor. Secondly, more powerful lasers are more expensive. The total power inserted into the fiber at the surface must be sufficient to be subdivided at each sensor and still provide enough power to excite the sensor as well as to read the vibrational displacement of the sensor. A third disadvantage of using a power splitter instead of a WDM is related to the readback signal. If there are ten sensors on the fiber, for example, then the splitter for each sensor should split ~10% of the incident light into an output fiber directed to the sensor and send the remaining light into the second output to go on down the fiber. The light directed towards the sensor will reflect from the sensor and then reenter the splitter as shown in Fig. 43. However, again only 10% of that reflected light is coupled by the splitter back into the input fiber. Therefore, a 10/90 splitter will reduce the reflected readback signal intensity at the interrogator to less than 1% of the read laser light power that was injected into the fiber. This fact that the reflected light intensity is inversely

proportional to the number of sensors on the fiber is the primary limit on the number of sensors that can be multiplexed because the signal-to-noise ratio (SNR) of the measurement drops quickly within increasing numbers of sensors to levels that are insufficient for locking the feedback loop.

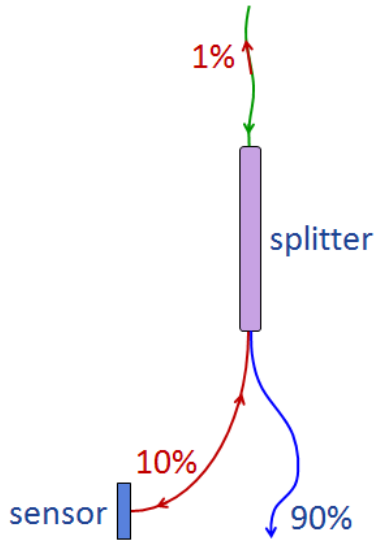

Fig. 43: Illustration of the effect of a power splitter on double-pass reflected light. The coupling efficiency in the 10% leg of the splitter operates in both directions, so the light reflected from a sensor back to the surface detector is reduced to ≤ 1% of the initial light propagating down the fiber.

Nevertheless, there are also some distinct advantages to using this approach if it can be made to work. The interrogation technique has already been demonstrated in a downhole environment and is reasonably robust and fairly simple, requiring only a single feedback loop. Only two lasers and one detector are required for measurements from all sensors, which reduce the cost of the equipment. Therefore, having already developed this interrogator for the previous measurements on single point pressure sensors, we investigated the ability of this approach to multiplex sensors via power splitters. Both read and drive lasers were specifically purchased for high output power (50 – 100 mW).[19] We were able to successfully track a sensor at the output of two 50/50 splitters as shown in Fig. 44. Therefore, this interrogation approach should be able to support at least four sensors on a single fiber. However, we were unable to successfully lock onto and track a sensor at the 10% end of a 10/90 splitter due to the lack of readback power from the sensor as described previously.

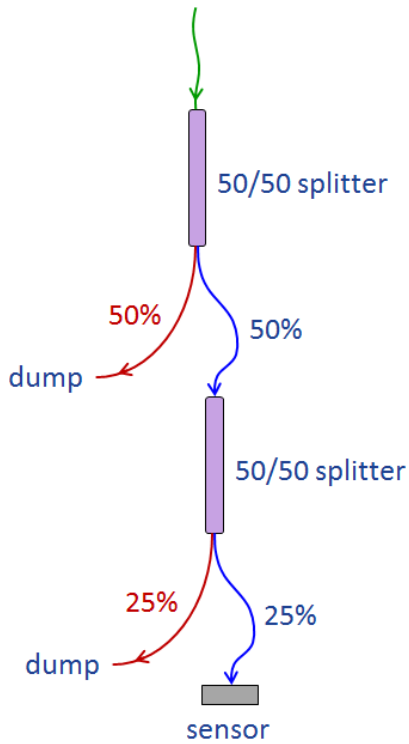

Fig. 44: Dual splitter arrangement used to successfully drive/readback a sensor.

B. Wavelength-dither interrogator

A second interrogation approach that was conceived early in this project is shown in Fig. 45. This approach is essentially modeled after that used in time-dependent laser absorption spectroscopy (TDLAS). The basic concept is that a triangle wave from a function generator is used to scan the modulation frequency of the VCO which is driving the drive laser. The drive laser is scanned over a frequency range that includes all the desired sensor vibrational frequencies. In addition to the slow frequency scan from the triangle wave (on the order of seconds), there is superimposed a high frequency modulation of the frequency from the VCO as shown in Fig. 45(b). When the laser hits a vibrational frequency of the sensor, it causes the sensor to start vibrating. The frequency dither, however, is meant to convert the reflected signal into a time derivative signal that eliminates much of the DC background noise. This interrogation approach has been successfully employed to obtain highly sensitive TDLAS measurements.

However, there are at least two significant differences between this concept and the typical TDLAS measurement. In TDLAS, the absorption line in the gas does not generate a modulated signal at the detector. However, with the Si MEMS die, the readback signal is modulated at the frequency of the resonance. Therefore, the signal coming from the detector is like that provided by the antenna of an AM radio. The low frequency envelope of the signal (blue line in top graph of Fig. 45(c)) is the real desired signal, not the high frequency component (red line in same

graph) that is actually detected. Therefore, for the sensor interrogator an AM detection circuit had to be added to the detector before the signal was fed to the lock-in amplifier. When this detection circuit was added to the interrogator, a signal was observed at the output of the lock-in when the frequency was scanned across the MEMS sensor resonance.

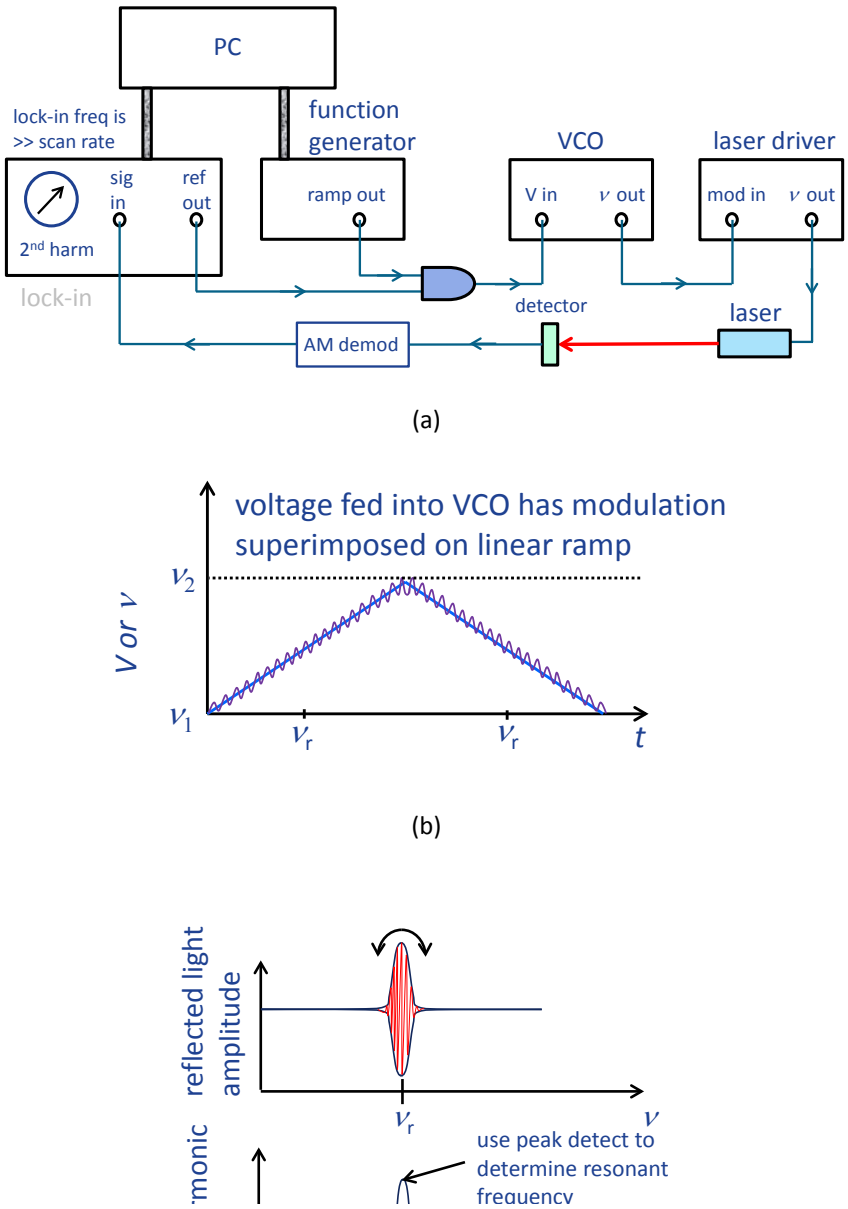

Fig. 45: (a) Concept for design of alternative interrogation technique. The drive laser is sinusoidally modulated. The frequency of the laser is swept across the frequency band of the resonance. During the sweep, the drive frequency itself is modulated at a lower frequency as shown by the purple line in (b). This generated a differential signal in the readback detector. The signal from the detector is at the resonant frequency as shown in red in (c). It is detected as shown by the bottom graph in (c) and fed into a lock-in amplifier. The output of the lock-in at the second harmonic then gives a peak signal at the frequency of the resonance.

However, the experimentally measured signal as shown in Fig. 46 was not of the expected shape, but was very asymmetric.

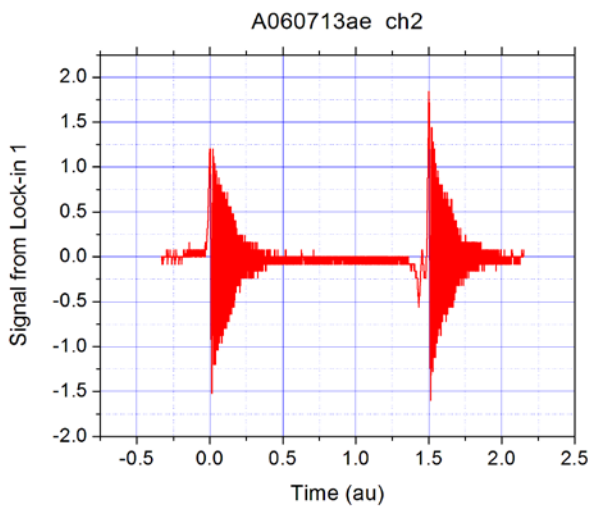

Fig. 46: Output from detector prior to the AM demodulation circuit. A triangle wave is fed into the frequency generator that drives the laser, so in one period the drive frequency sweeps across the resonance of the MEMS sensor twice, once as the frequency increases and once as it decreases.

By adjustment of sweep rates and modulation amplitudes it was possible to obtain a signal at the output of the lock-in at the second harmonic as shown in Fig. 47. While this signal looks very good, it is not clear if this approach can be used to reliably identify the resonant frequency. The signal detection scheme was modeled to obtain a better understanding of the issues. An example of the model calculation is shown in Fig. 48.

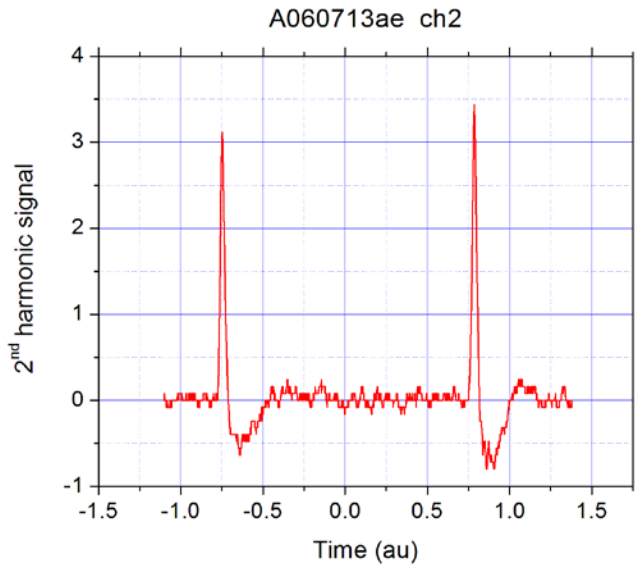

Fig. 47: Output from lock-in at second harmonic with adjustment of various parameters.

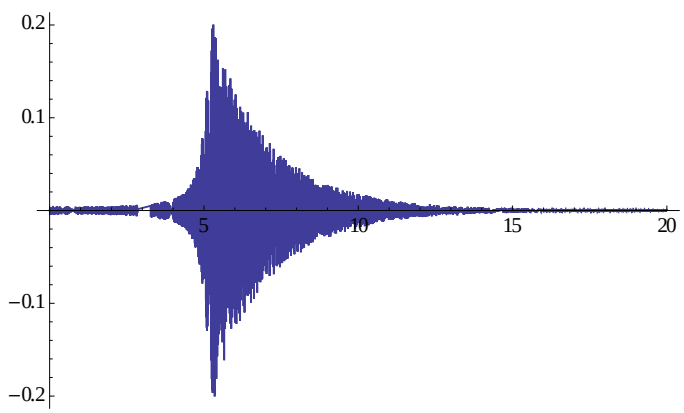

Fig. 48: Simulation of output from detector prior to the AM detector circuit.

The large asymmetry in the output waveform was not expected from the original concept shown in Fig. 45(c). It turns out that this asymmetry is due to the high Q factor of the MEMS resonators. With Q's between 10,000 and 20,000, once they begin to vibrate at the incident frequency of the laser drive, their ring down time is on the order of a second. This is on the same order as the time for a frequency scan across the resonance band. Therefore, once the drive laser begins to cause the resonator to oscillate, the resonator continues to oscillate with a complex phase relationship to the drive laser as the laser continues to scan frequency. This complex phase relationship between the ringing resonator and the laser modulation is what generates the

asymmetric signal response in time shown in Figs. 46 and 47. Another way to look at this is that the MEMS sensor does not dissipate the laser drive energy very quickly, unlike the atomic absorption line transitions in TDLAS, so the resonator does not follow the drive laser frequency exactly. This phase offset makes it much more difficult to precisely measure the resonant frequency in a frequency scan. As a result, this measurement technique was rejected as a potential approach for multiplexing sensors.

C. Interferometric interrogator

A third interrogation approach is shown schematically in Fig. 49. The optical layout in the lab for developing, optimizing, and testing the interrogator design is shown in Fig. 50. In this approach, the light from a 1310 nm laser is modulated and used to drive the resonator as in the first "conventional" approach. Readback, however, is not accomplished with a read laser, but rather with a *broadband* light source which may be either a superluminescent light emitting diode (SLED) or an amplified spontaneous emission (ASE) light source.

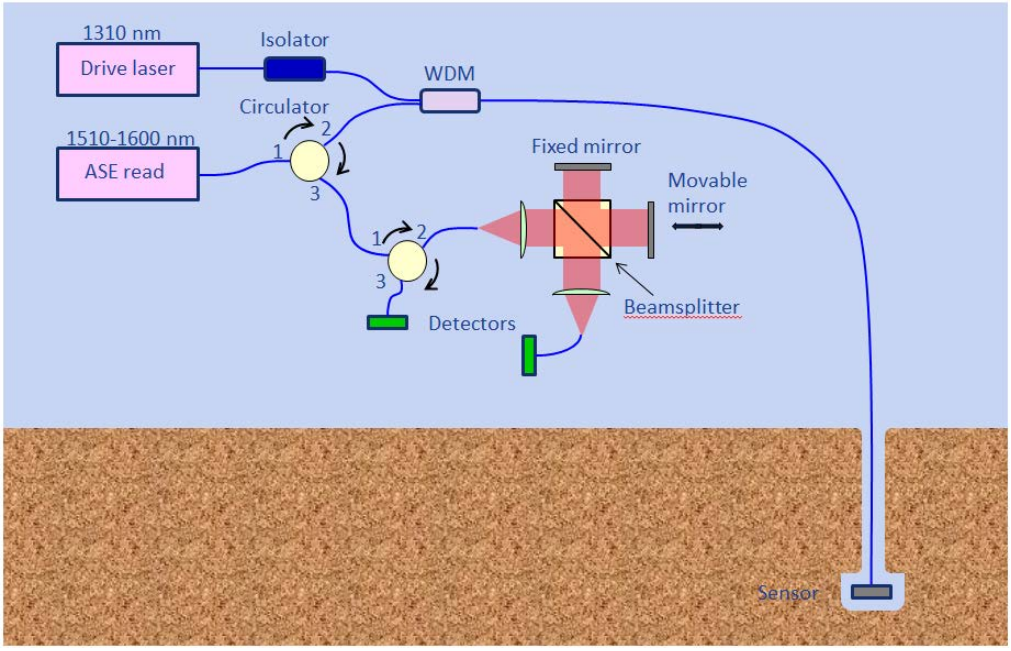

Fig. 49: Interferometric interrogator design.

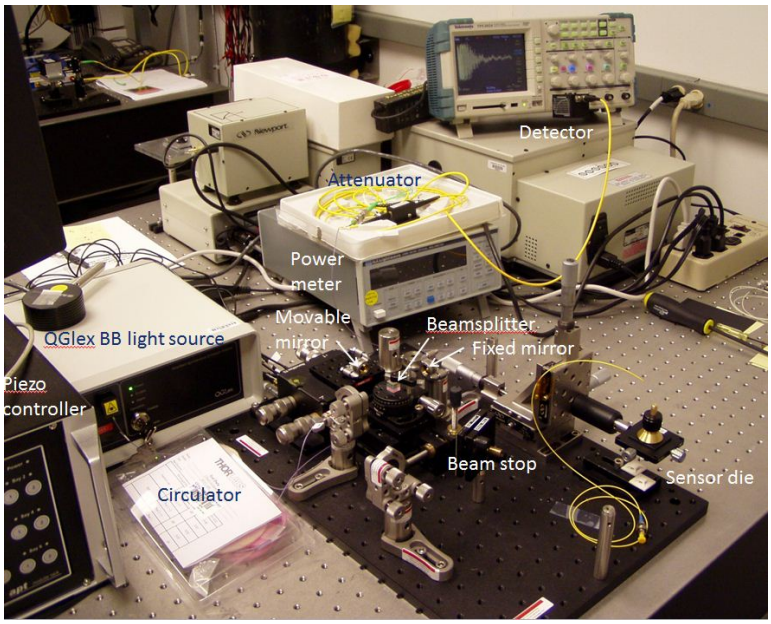

(a)

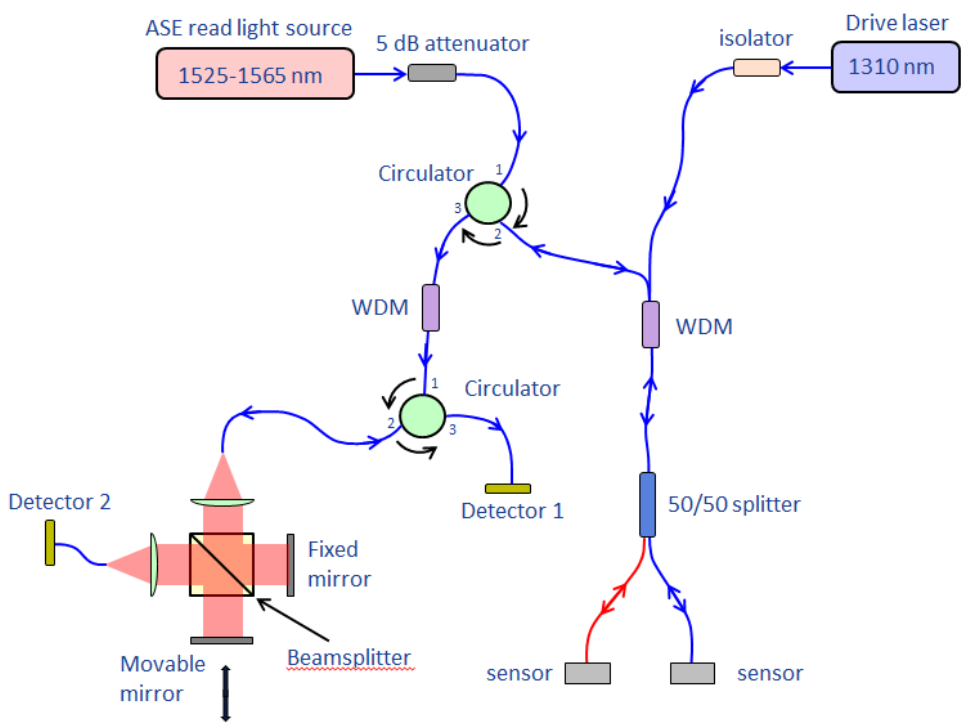

(b)

Fig. 50: (a) Photo of interferometric interrogation system in the lab. (b) Schematic layout of optical interrogator used for generating the data in this report.

A high power ASE broadband light source[20] was purchased by GE for this project. It outputs 250 mW between ~1525 nm and 1570 nm (Fig. 51). The light source can be connected to a computer via a USB cable and is operated using a vendor-supplied GUI.

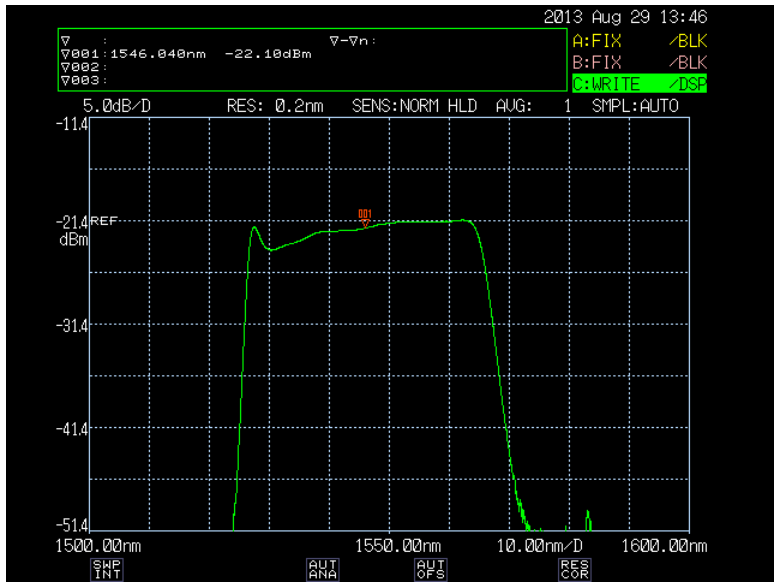

Fig. 51: Optical spectrum centered at 1550nm with FWHM of about 50nm.

Because the ASE light source is broadband, it has a short coherence length. The coherence length is generally related to the wavelength spectral range by the approximate relation

$$L = \frac{2\ln(2)}{\pi\, n}\frac{\lambda^2}{\Delta\lambda} \tag{4}$$

where λ is the center wavelength, Δλ is the spectral width, and *n* is the refractive index. Inside the vacuum of the sensor die the coherence length is ~24 μm for this light source. For a resonator-to-cap spacing of 100 μm, therefore, there should be little interference from this light source between the light reflected from the cap and the light reflected from the resonator, because the optical path length between these two reflections is much longer than the coherence length of the light source. This is in contrast to the "conventional" interrogator approach which uses a *coherent* readback laser diode as its light source in order to generate the interference signal between the resonator and the cap.

In order to generate the coherent interference for monitoring the vibration frequency of the resonator in the interferometric approach, the light which is reflected from the sensor die, including both the cap and the resonator, is split 50/50 by the beamsplitter in the Michelson interferometer and then an additional propagation delay is inserted into one of the two light paths of the interferometer before the beams in the two paths are recombined. Interference fringes can

then be observed when the delay between the two light paths matches that of the round trip optical path length between the resonator and cap.

A simple way to understand this is to consider the complete interferogram that is generated when the movable mirror is scanned. The various reflecting surfaces in the sensor are shown schematically in Fig. 52 and include the tip of the fiber ($R \cong 4\%$), the top surface of the sensor die ($R \cong 34\%$), the bottom surface of the sensor die ($R \cong 34\%$), and the resonator ($R \cong 34\%$). The light from these reflections is expected to generate an interferogram similar to that shown in Fig. 53(a). When the optical path difference between the two halves of the interferometer is zero, all of the reflected light from the sensor and any other surfaces in the beam path recombine coherently at the output of the interferometer to generate the so-called zero path peak (ZPP) and its nearby interference fringes.

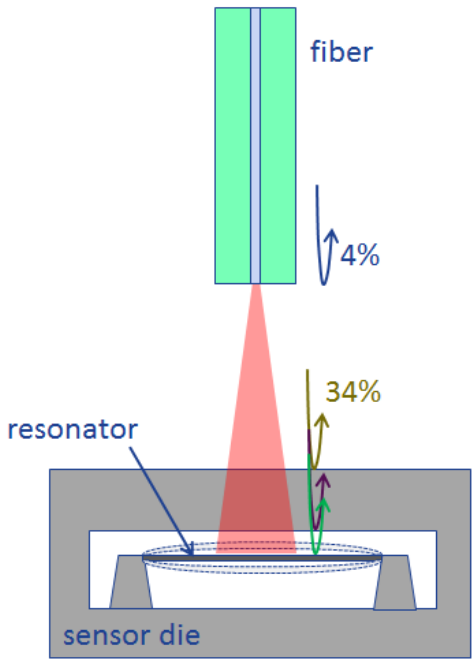

Fig. 52: Light from a cleaved fiber reflects from the end of the fiber at ~4%, and from the top and bottom surfaces of the sensor die and the top surface of the internal resonator at ~34%.

When the optical path difference in the interferometer becomes equal to the optical path difference between any two of the reflecting surfaces, there is again a set of interference fringes, but with reduced amplitude relative to the ZPP since only a portion of the reflected light is coherently interfering.

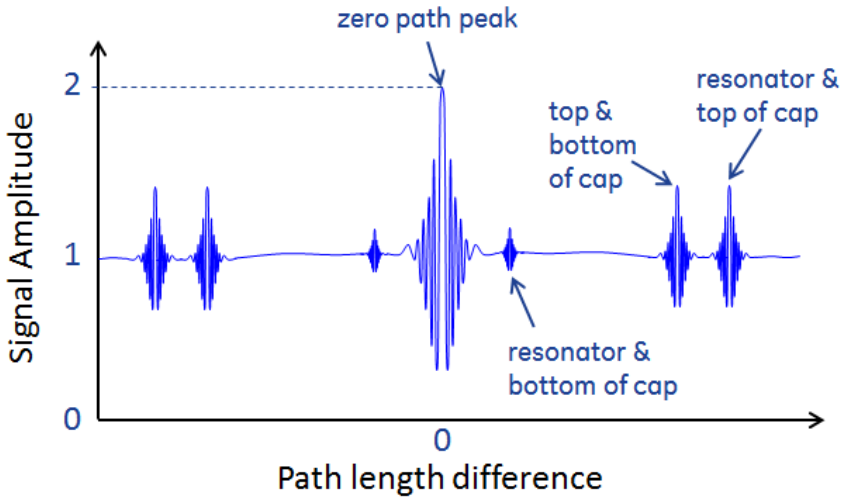

(a)

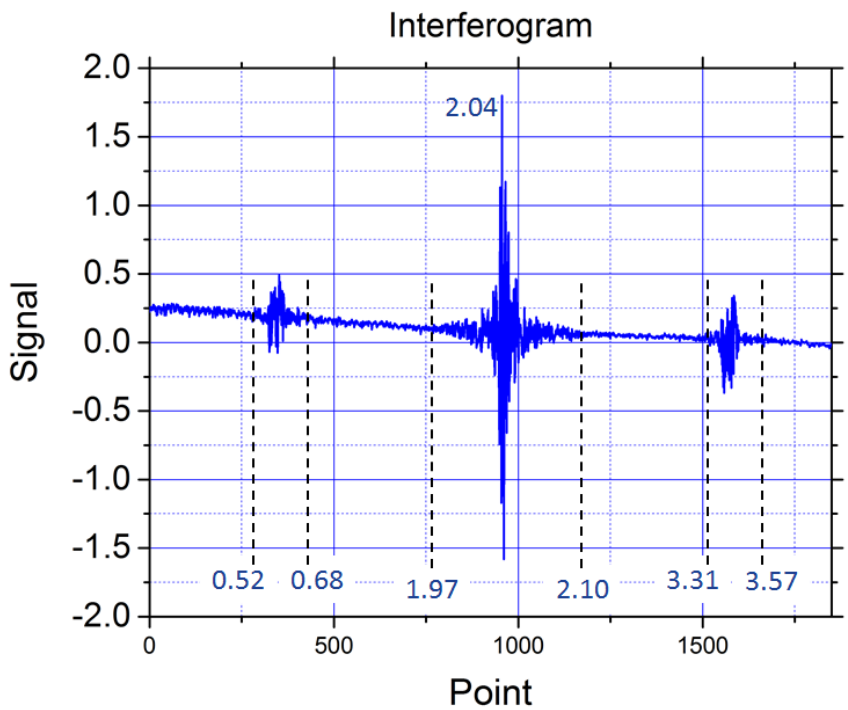

(b)

Fig. 53: (a) Schematic of interferogram from translation of movable mirror. Whenever the optical path difference of the two mirrors in the interferometer equals the path difference between any two reflections in the sensor system, a series of interference fringes is observed. (b) Interferogram measured by manually scanning the position of the movable mirror. The total scan length is 4 mm. Approximate micrometer readings of the fringe locations are also shown.

An experimental interferogram was measured by manually scanning the micrometer positioner for the movable mirror in the interferometer at approximately a constant speed. The interferogram is shown in Fig. 53(b). The *x* axis scale is mirror position in arbitrary units. The ZPP is evident at the center of the interferogram. There are also two smaller fringe systems on either side of the ZPP. These correspond to interference of reflections from the top of the Si cap and either the bottom of the cap or the resonator inside the sensor. The spacing of these fringes is ~1.42 mm from the ZPP. For a Si refractive index of 3.476, this corresponds to a Si cap thickness of ~400 μm.

When the smaller fringe system on the left of Fig. 53(b) is scanned using the piezo in higher resolution, the fringes appear as shown in Fig. 54. Clearly, there are two primary peaks that are separated by ~60 μm. These peaks apparently correspond to the distance between the resonator and the inner cap surface. As confirmation of this, the interferometer mirror position was adjusted to each peak separately and it was attempted to measure the resonator vibration signal. On the left peak a very strong vibration signal was observed at 11.845 kHz, while at the right peak no signal was observed. Because the piezo moves the mirror towards shorter path differences, the left peak corresponds to a larger optical path difference between the mirrors in the interferometer which is expected for interference between the top of the Si cap and the resonator. Of course, the interference between the top and bottom surfaces of the cap, corresponding to the right fringe peak, is not vibrating and should not produce a readback signal.

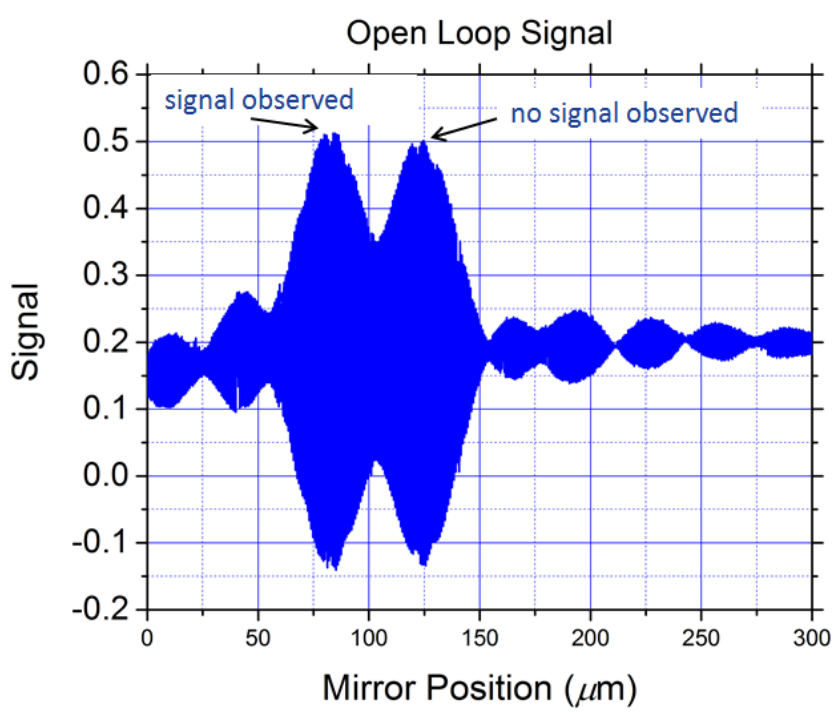

Fig. 54: Interferogram fringes measured by scanning the piezo in high resolution in the neighborhood of the left fringe system in Fig. 55(b).

In the standard Michelson interferometer, the light is detected at the output of the interferometer by detector 2 in Fig. 50. For a perfectly aligned interferometer with perfect mirrors, the intensity of the light at the ZPP at detector 2 is twice the intensity of the incoherent light at large optical path differences as shown in Fig. 53(a). At the ZPP, there is no light reflected out the *input* port of the interferometer because at this position all of the light destructively interferes at the input port. However, when the path length is adjusted so that the light is incoherent, then half of the light entering the interferometer through the input port will also be reflected back out of the input port. This is how energy conservation is maintained by the interferometer.

The vibration of the resonator is detected by its effect on the reflected light from the optical cavity formed by the top surface of the sensor die and the resonator as shown in Fig. 52. This fringe system is shown in expanded form in Fig. 57.

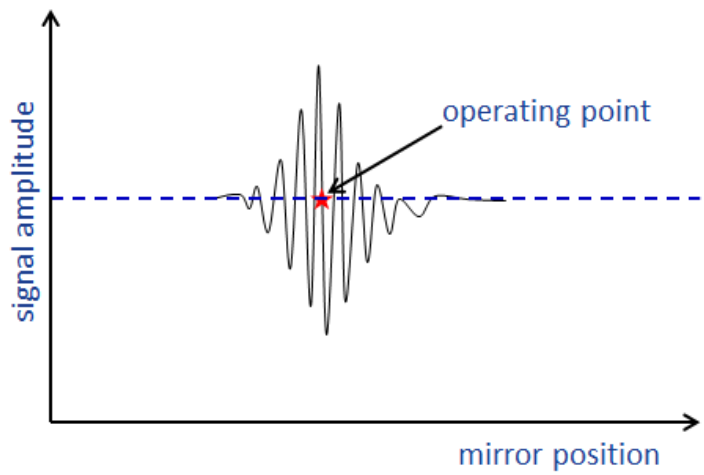

Fig. 57: Expanded view of interference fringe system for the optical cavity formed by the top surface of the sensor die and the resonator. The operating point is at the highest slope region of at the center of the fringe system as shown.

As the resonator vibrates, it changes the optical path length of the cavity by typically a fraction of a wavelength. This causes the fringe system to shift back and forth along the *x*-axis at the vibration frequency of the resonator. If the movable mirror is fixed at the position of the red star in Fig. 57, then as the resonator vibrates, the signal amplitude also vibrates at the frequency of the resonator. The average path length of the cavity, however, is subject to drift when, for example, the temperature of the sensor changes. Therefore, it is necessary to implement a feedback loop with the movable mirror so that if the position of the fringe system slowly drifts, the position of the movable mirror can also change with it to maintain the operating point at a fixed fringe position. The position of the movable mirror in our setup is determined by both a manual micrometer with a 4 mm travel, and a piezo with a 20 μm total path offset. The latter can be adjusted automatically over this entire range via an analog input signal to its controller.

The error signal for the feedback loop is simply the difference signal of the two detectors shown in Fig. 55(c). As the fringe system begins to drift, the difference signal will either increase or decrease depending on the direction of drift. This signal is filtered and inserted into both a proportional and integral circuit and finally into the analog input to the piezo with the proper phase for negative feedback. The mechanical system of the interferometer was found to have a number of mechanical resonances from vibrating mirrors, etc., including a very strong resonance at ~570 Hz. Therefore, an electronic filter was included in the feedback circuit to ensure that the closed loop feedback at this frequency was highly attenuated to prevent oscillation within the feedback loop. A better way to handle this would be to actually move the mirror by the piezo to cancel the motion of the mirror vibration at this frequency. However, in our current design, the mass of the translation stage and mirror that must be moved by the piezo is sufficiently large that it introduces its own time constant into the feedback loop that reduces the response time of the actuator, and we were unable to develop a circuit that could overcome this delayed response.

The electronic feedback circuit design for the piezo is shown in Fig. 58. The low pass filter is set for a cutoff frequency of 300 Hz, so it is much lower than the vibrational frequency of the resonator. Therefore, the resonator signal has no effect on the feedback circuit for the mirror position and continues to generate a high frequency signal in the difference output of the two detectors. If the mechanical Michelson interferometer were to be replaced by an interferometer with an electronically adjusted phase delay, then in principle the feedback loop could also eliminate the signal oscillation due to the resonator. In that case, the actual signal would be generated by the feedback circuit rather than the detectors.

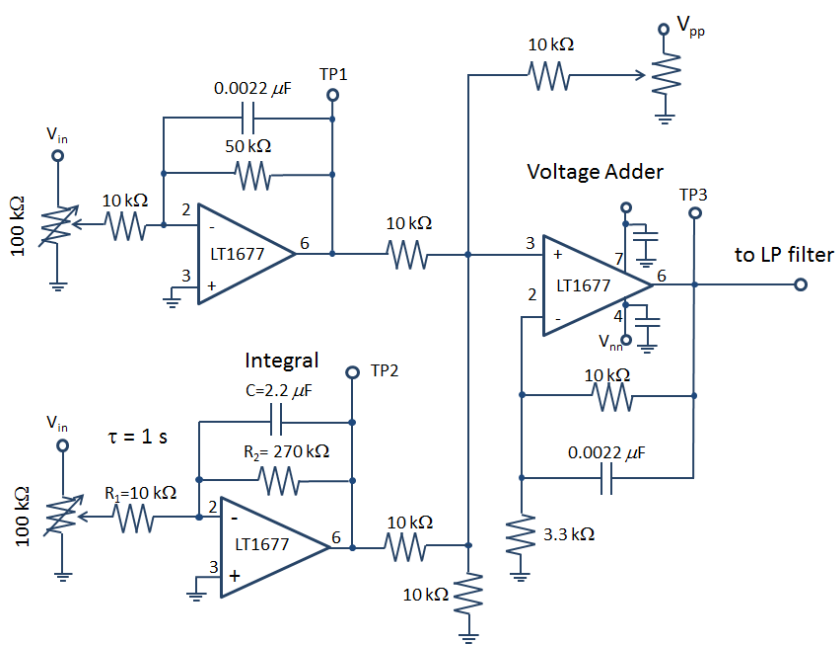

(a)

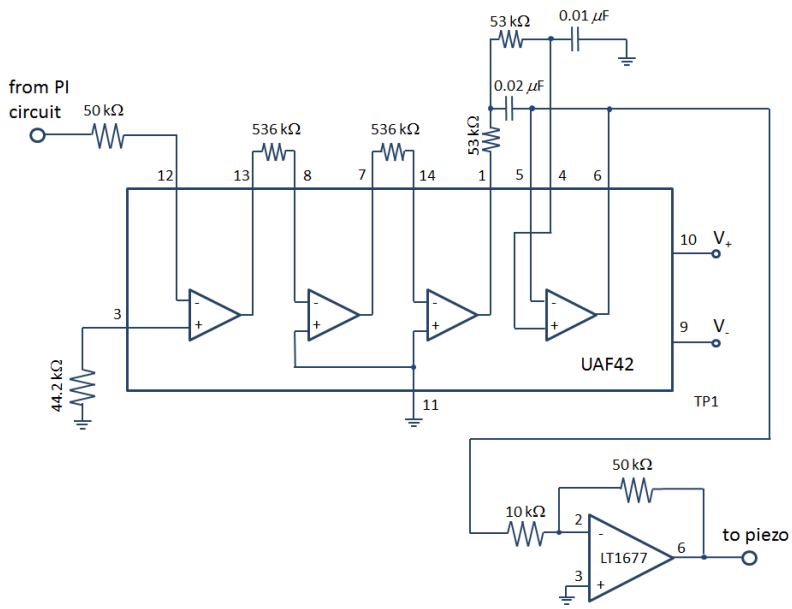

(b)

Fig. 58: Feedback circuit to the piezo for adjusting the movable mirror position in interferometer to maintain the operating point as shown in Fig. 18. (a) Input stage of feedback circuit including a signal proportional to the error signal and a signal proportional to the integrated error signal. There is also a third signal that injects a DC offset into the feedback signal that can be manually adjusted in order to move the mirror to the best operating point in the fringe system. (b) Feedback signal is then filtered by a 3-pole low pass Butterworth filter[21] at 300 Hz and amplified before being inserted into the analog input to the piezo.

The feedback loop was tested in the following manner. First, with the loop unlocked, the piezo was stepped in 0.4 V increments corresponding to ~0.1 μm/step. This caused the differential readout signal to map out the interference fringes as shown in Fig. 20(a). The feedback loop to the piezo was then closed and again the piezo was "stepped" via computer control in 0.4 V increments. However, as shown in Fig. 59(b), the feedback circuit automatically generated a negative offset voltage to cancel the computer-generated voltage to maintain the position of the mirror as indicated by the lack of change in the differential signal level. When the feedback loop was opened at ~point 3700, however, the mirror immediately jumped by ~6 μm.

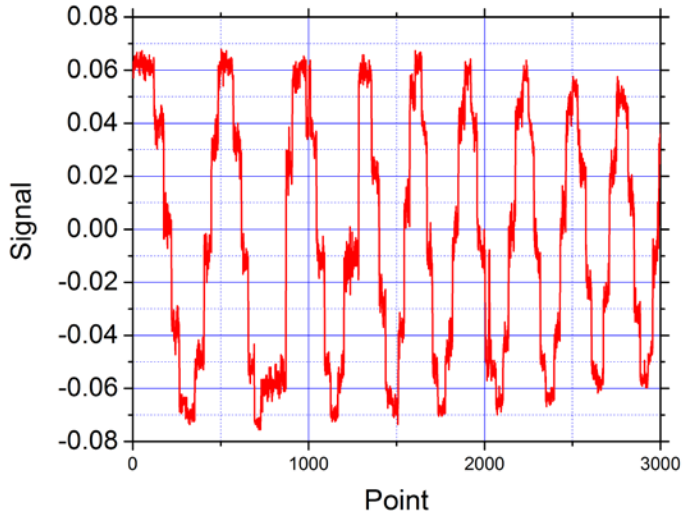

(a)

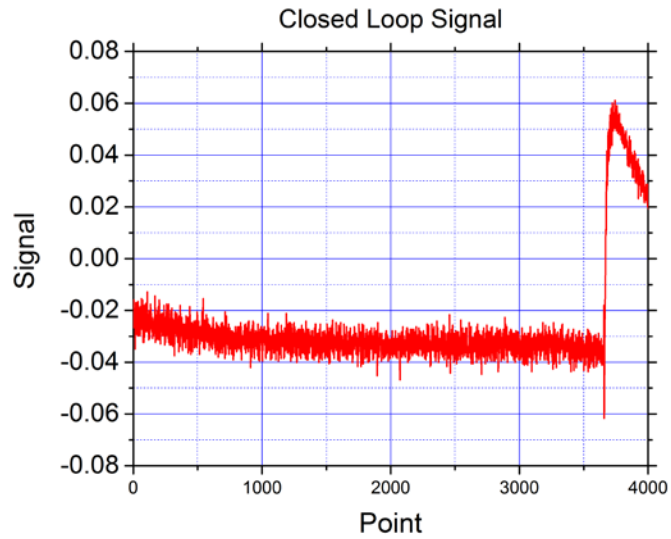

(b)

Fig. 59: (a) Open loop signal as the piezo was stepped in increments of 0.4 V. (b) Closed loop signal as the piezo was stepped in increments of 0.4V beginning at point 700. At ~point 3700 the loop was unlocked and the piezo jumped from a position of 11.24 μm to a position of 17.14 μm.

Once the feedback loop has been implemented for the piezo mirror, a second feedback loop must also be implemented. As in the conventional interrogator design, a laser driver is required to output an intensity-modulated drive signal at the frequency of the resonator vibration. This laser operates at a different wavelength than that of the broadband light source so that it can be subsequently filtered out of the reflected read signal light to the detectors. A 130 mW drive laser

operating at a wavelength of 1310 nm was used to do this.[22] The laser was modulated by a voltage controlled oscillator (VCO) output from a Stanford Research SR530 lock-in amplifier.[23] This modulated signal was fed into a laser driver[24] which combined it with a DC offset to generate a sinusoidally modulated light intensity from the laser. The VCO reference signal was also used as the reference for the lock-in amplifier. The difference signal from the two detectors was fed into the lock-in and synchronously detected at the VCO frequency. The VCO frequency is manually adjusted to maximize the amplitude of the detected signal and to set the reference phase shift of the detected signal to zero. At this point, when the resonator frequency begins to change, due to a change in external pressure for example, the phase of the signal detected by the lock-in also changes rapidly. Depending on the direction of the frequency shift, the phase will either increase or decrease as shown in Fig. 60.

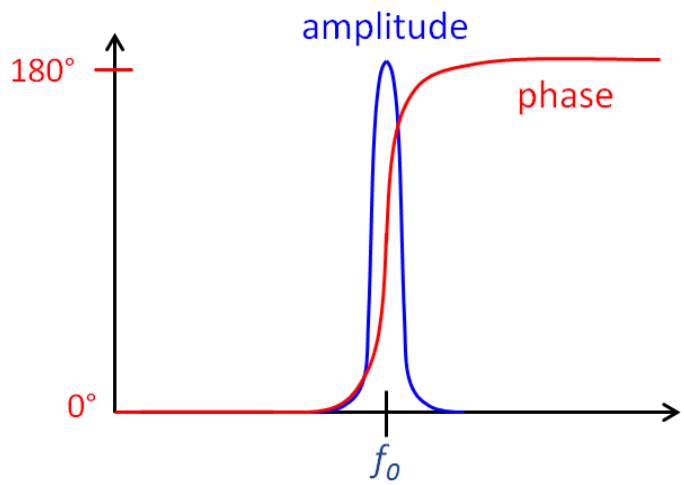

Fig. 60: Schematic of response of sensor resonator to drive frequency. Maximum amplitude occurs at the resonant frequency of the sensor, f_0. The resonant frequencies of the sensors for this project typically lie between 10 kHz and 100 kHz. The full width at half maximum (FWHM) for these sensors is typically 1 – 2 Hz, corresponding to extremely high Q oscillators. At frequencies well below resonance, the phase shift between the drive laser and the sensor response is close to 0°. At frequencies well above the resonance of the sensor, the phase shift approaches 180°, out-of-phase. At the resonance, the phase changes very quickly from ~0° to ~180°.

In the SR530 lock-in there are outputs for both amplitude and phase (R and ϕ), or for x and y. The x output is simply ($R \cos \phi$), and the y output is ($R \sin \phi$). If the relative phase shift in the lock-in, ϕ, is adjusted to maximize R and to make x positive, then the x output can be used to measure amplitude and the y output can be used as the error signal. For the SR530, this is important because the x and y outputs are updated at a 1 kHz rate, while the R and ϕ outputs are only updated at a 60 Hz rate, and the faster response time was found necessary for closing the feedback loop. The y output signal is amplified and again fed through a proportional and integral

stage to generate the output signal for controlling the VCO in the lock-in. The circuit diagram for this feedback loop was shown previously in Fig. 58.

There is one final note regarding the detectors. The detectors in the current system are Thorlabs PDA10CS InGaAs detectors with switchable gain.[25] The built-in gain makes these detectors convenient to use, but their noise equivalent power (NEP) is relatively high, 2×10^{-12} W/$\sqrt{Hz}$. As previously mentioned, we are using much lower noise, nonamplified detectors for the pulsed laser interrogator with NEP of 4.5×10^{-15} W/$\sqrt{Hz}$. In the current system, other noise sources: vibration unbalances of the detectors, laser intensity noise, etc., are the dominant noise sources, but if these can be sufficiently reduced, then switching to a quieter detector may be beneficial.

D. Pulsed laser interrogator

The pulsed laser interrogator approach is illustrated in Fig. 63. A pulsed laser outputs a high power polarized laser pulse into a polarization maintaining (PM) fiber. A continuous laser also emits polarized light at the same wavelength, which is combined with the pulsed laser light using a polarization combiner.[26] (Alternatively, it may be possible to use a single laser diode to generate both pulses and the DC light level, but this has not been tested in the laboratory.) The combined laser light is passed through a circulator and then to an arrayed waveguide grating (AWG). The AWG is used to combine the laser light from this system with that from laser systems operating at slightly different wavelengths, before the combined laser light is injected into the downhole fiber cable. Once downhole, a CWDM is used to split off the appropriate laser wavelength at each sensor. Light reflected from the sensor is reinserted into the fiber via the CWDM and returns to the surface, where it is split off by the AWG to its appropriate wavelength detector. In this arrangement, therefore, there are two lasers for each sensor both operating at the same wavelength. The laser pulse excites the resonator of a particular sensor and causes it to vibrate at its normal mode frequencies. The vibrating resonator modulates the optical cavity formed with its sensor cap as in the conventional interrogator approach and the DC laser read beam is used to measure the vibration of the resonator between pulses. The detector signal is sampled at a rate that is at least twice the rate of the highest resonator frequency. Laser pulses are spaced at approximately the decay time of the resonator. A sufficient number of reflected scans are averaged and then a Fourier transform of the averaged scan determines the resonator vibrational frequencies.

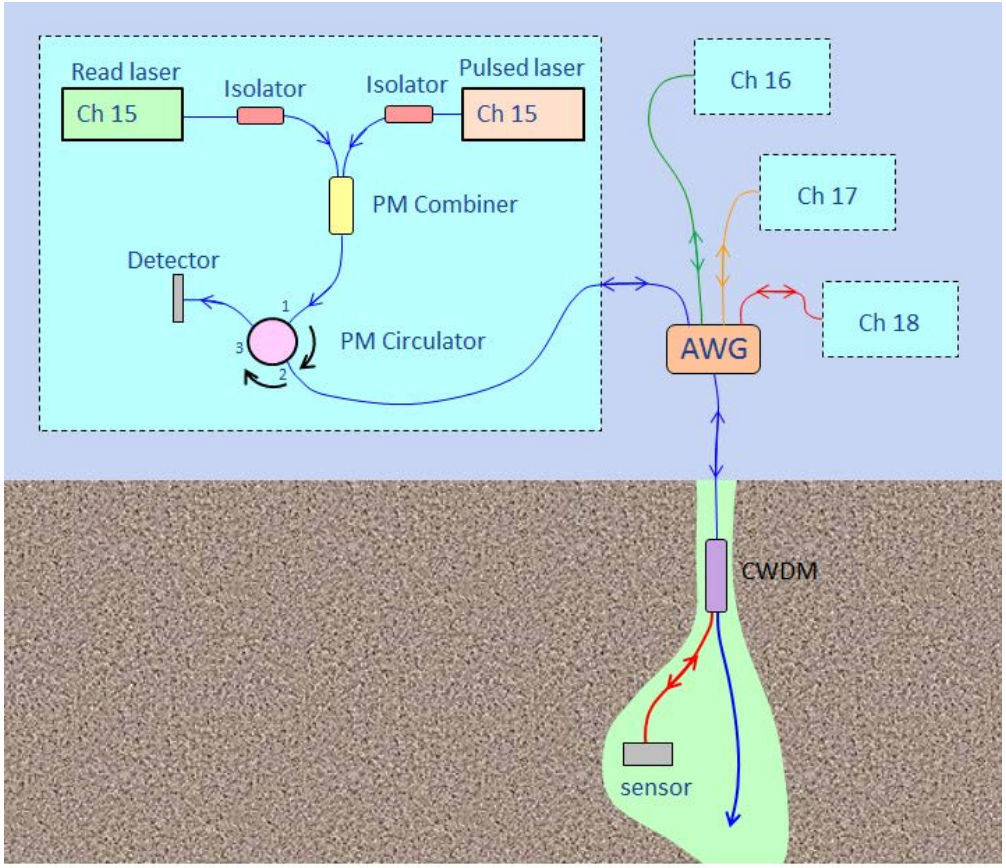

Fig. 63: Design of pulsed laser interrogator for multiplexing.

A Cybel fiber laser[27] at 1550 nm was used as the pulsed laser light source. This laser outputs pulses at 10 kHz that have a 10 μs pulse length. The averaged output power of the laser is 250 mW. The energy per pulse is, therefore, 25 μJ. The laser was successfully aligned with an acousto-optic modulator to inject pulses into a fiber at a rate which could be selected from 1 Hz to 10 kHz.

A photograph of the experimental setup is shown in Fig. 64. The setup includes the pulsed fiber laser, a 10 kHz frequency generator, a 1 Hz pulse generator, an acousto-optic modulator unit, a laptop, power supplies, a collimator lens, a photodetector, and an oscilloscope.

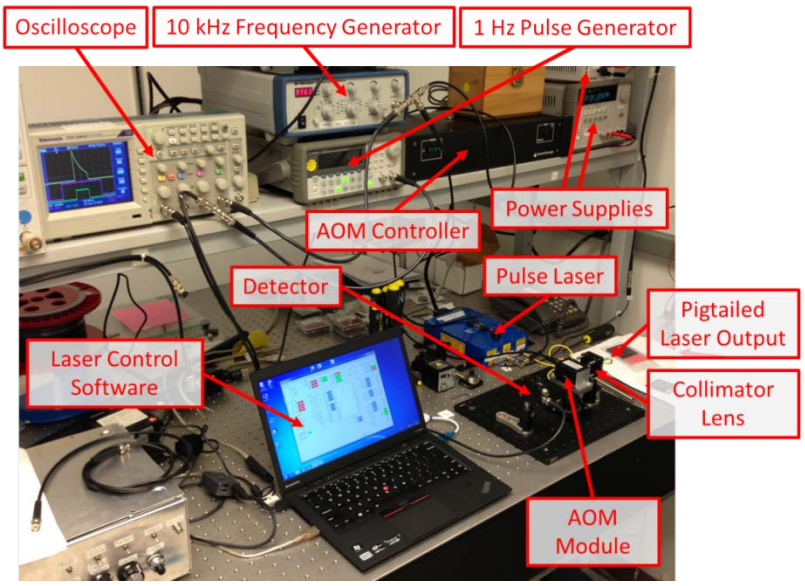

Fig. 64: Photograph of experimental setup.

Fig. 65 shows the front and the back of the laser unit. One can control the Cybel laser through the supplied control software as shown in Fig. 66. The output power of the Cybel laser can be controlled using the pump current sliding bar. It is important to not exceed a pump current of 4 A to prevent the laser unit from being damaged.

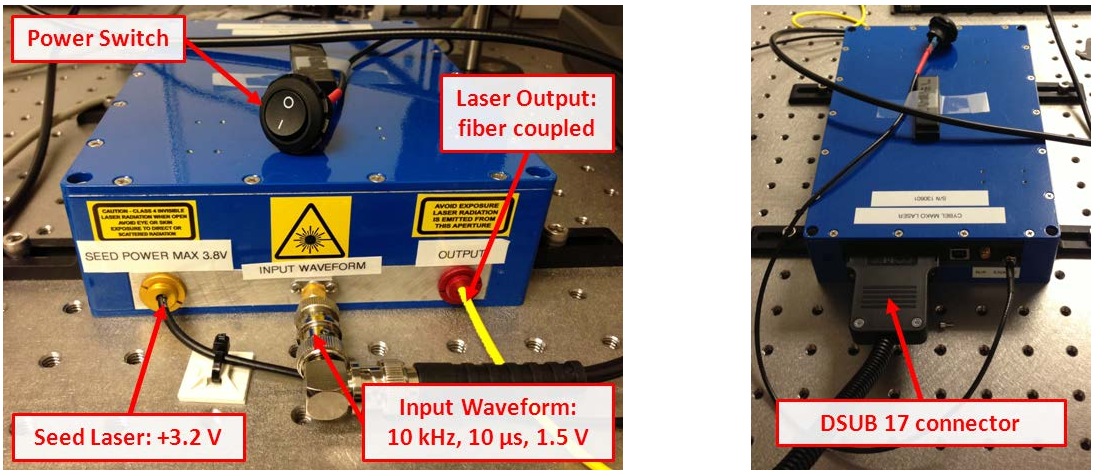

(a) (b)

Fig. 65: Photograph of Cybel pulse laser: (a) front-side and (b) back-side view.

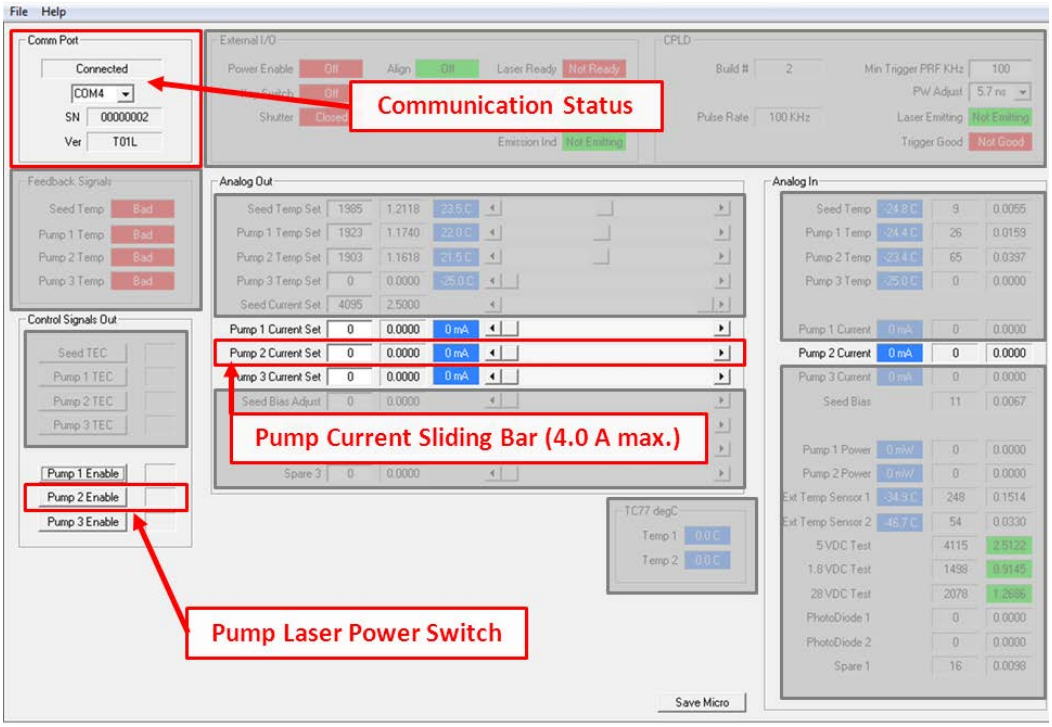

Fig. 66: Screen shot of the graphical interface of the Cybel laser control software. The non-functional windows are greyed out. The Pump current must not exceed 4.0 A.

The high Q sensors when struck with a pulse of light will require ~1 s in order to ring down. As shown in Fig. 67, an acousto-optic modulator (AOM) is used to select only one pulse per second from the pulse train emitted by the laser.

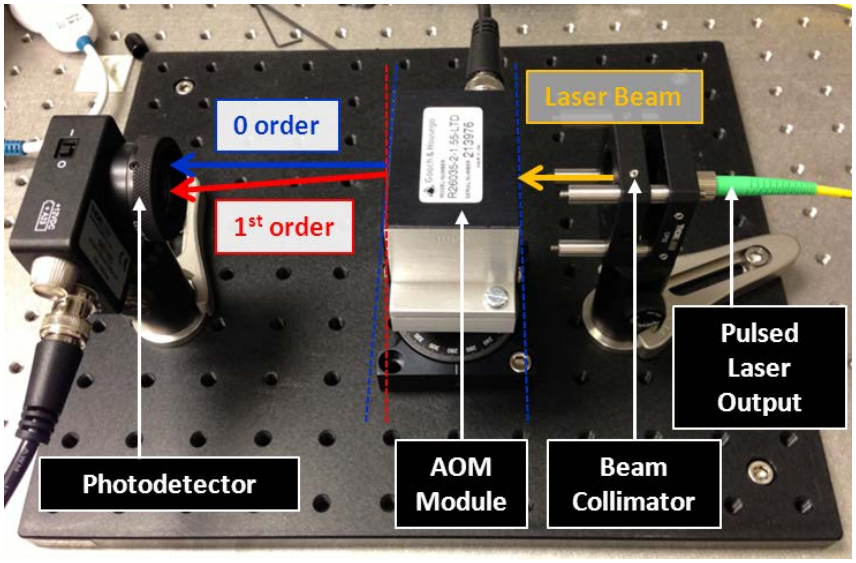

Fig. 67: Experimental setup of pulsed laser approach for the CO_2 sequestration project.

The transmitted pulse is then detected by a photodetector and displayed on an oscilloscope. The curves of the pulse laser output signal, the 10 kHz trigger pulse signal, and the 1 Hz pulse picker signal are displayed in Fig. 68.

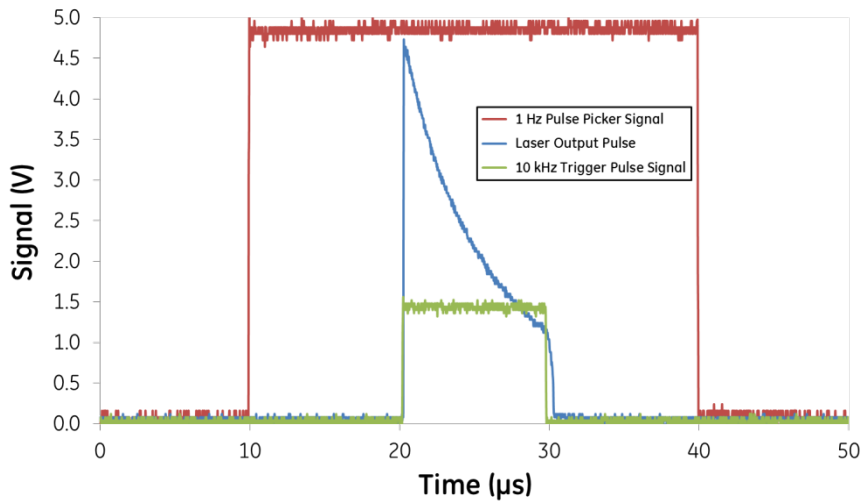

Fig. 68: Signal curves laser output pulse, laser trigger signal, and AOM pulse picker signal.

The laser output beam is then focused into an optical fiber so that the laser power can be coupled to the pressure sensors.

The initial pulsed laser system that was constructed used a 1310 nm laser for the CW readback light source rather than a 1550 nm laser at the same wavelength as the pulsed laser. This approach enabled using a 1310/1550 WDM to combine the read and pulse laser power without losing any power from either source, similar to that of the polarization combiner shown in Fig. 63. This setup is shown in Fig. 69. Of course, using a polarization combiner has the advantage of providing a single wavelength for both pulse and readback, thereby enabling a simple WDM downhole multiplexing technique. A read laser at the same wavelength as the pulsed laser may also be combined by a 10/90 beam splitter/coupler, for example, which would, however, require a high power read laser so that even 10% of the laser power would provide sufficient SNR for readback. Initial results indicate that it is important to have a relatively large read laser power to overcome various noise sources, so using a 10/90 beam combiner may not be suitable.

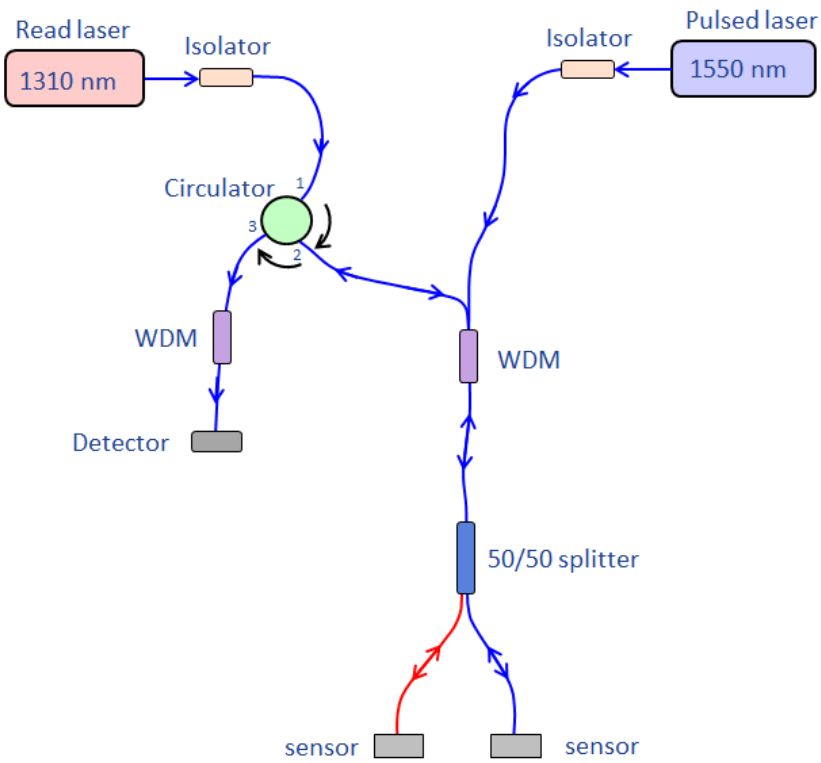

Fig. 69: Pulsed laser interrogator design for initial laboratory testing.

In Q4, 2013, the pulsed laser interrogator was used to make measurements on individual sensor die for the first time and initial results were reported. A 10 Hz pulse rate was used. A sampling rate of 200 kHz was also used to ensure that the known resonant modes at frequencies up to ~95 kHz could be measured. The average optical power from the pulsed laser that was actually coupled into the fiber was ~54 mW. In order to improve the SNR, 10,000 scans were averaged over 17 minutes. A Fourier transform of the averaged scan was then performed and the result is shown in Fig. 70(a). The same data plotted on an expanded vertical scale are shown in Fig. 70(b). Several of the resonator frequencies are clearly visible above the background noise level, not just the dominant low frequency resonance at ~12 kHz.

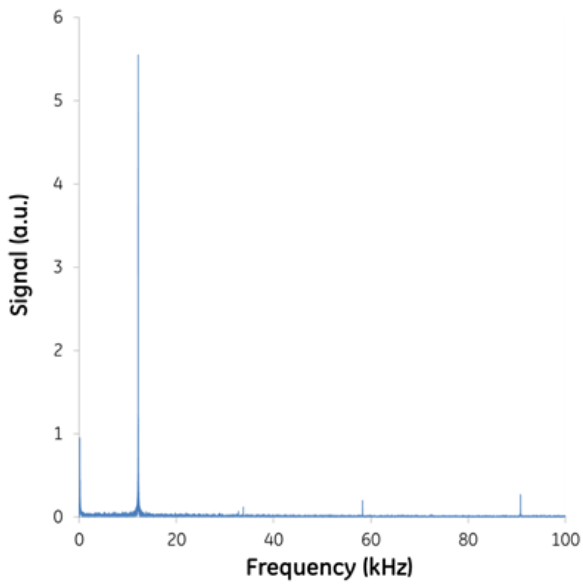

(a)

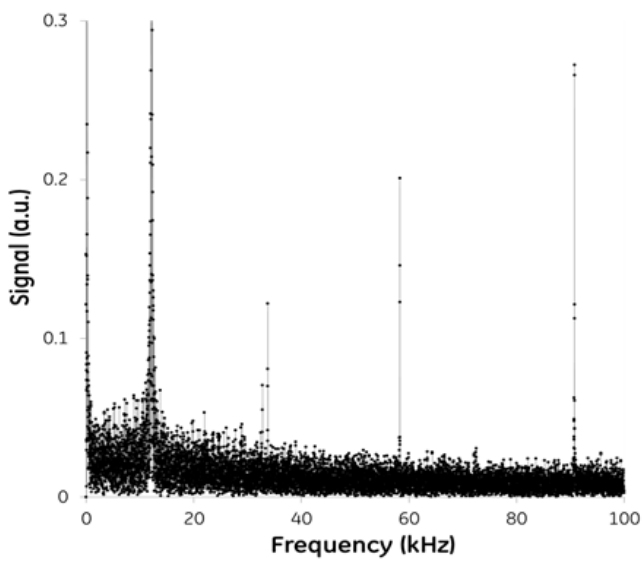

(b)

Fig. 70: (a) Fourier transform of 10,000 averaged scans between laser pulses. (b) Expanded vertical scale of (a).

Although 10,000 scans were averaged to obtain the result in Fig. 70, it was found that even a single laser pulse/scan captured in 0.1 s was sometimes sufficient to discern the resonant frequencies. An example of a single scan capture is shown in Fig. 71. This indicated that there were spurious noise sources in the instrument that could potentially be eliminated for faster data acquisition.

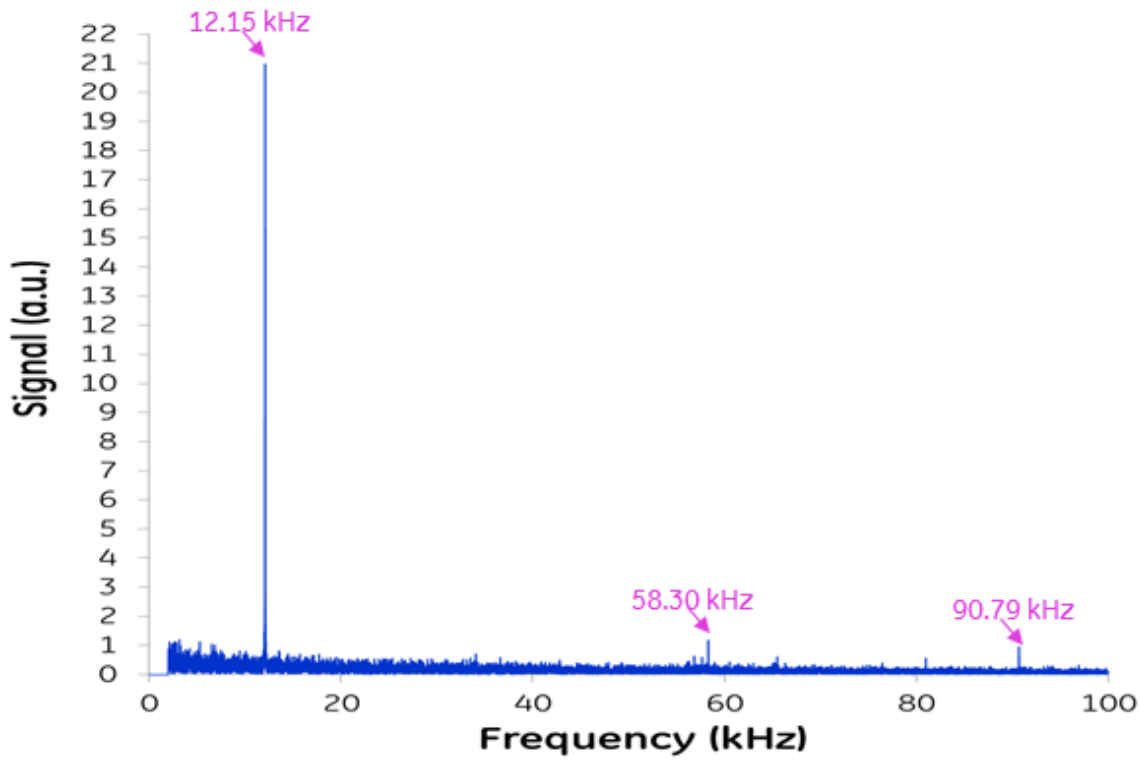

Fig. 71: Fourier transform of scan following single laser pulse.

Subsequently, it was determined that the primary noise source was frequency mode hopping of the laser. The output spectrum of the laser was measured on an optical spectrum analyzer and is shown in Fig. 72. The spectrum is obviously much broader than can be tolerated for a readback light source. Even though the laser was temperature stabilized, the spectrum was almost constantly changing. The reflectance of the optical cavity formed by the resonator and the inside surface of the sensor cap with a gap of 160 μm is shown in Fig. 73. A 2 nm shift in wavelength is sufficient to cause the reflected light intensity to change from a maximum to a minimum. Thus, because the laser is constantly switching between different modes with wavelengths over a 15 nm spectrum, this adds a large amount of noise to the signal while simultaneously averaging the reflected light over multiple reflectance minima and maxima, which reduces the signal level from the resonator vibration. In order to measure vibrational frequencies with this read laser, signal averaging is a necessity unless one happens to capture the scan during a rare quiet period between mode hops.

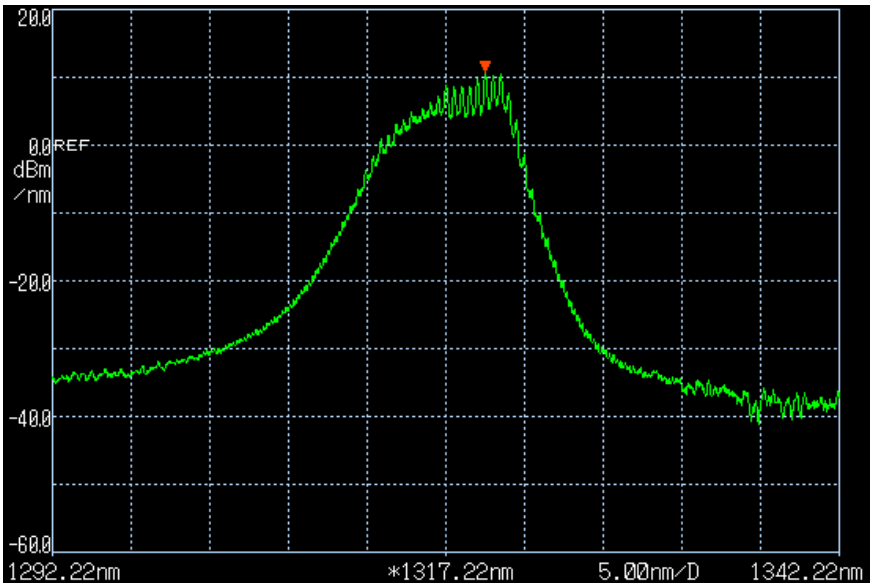

Fig. 72: Spectral output of 1310 nm laser used initially for readback. The full width at half maximum of the laser spectrum is ~15 nm.

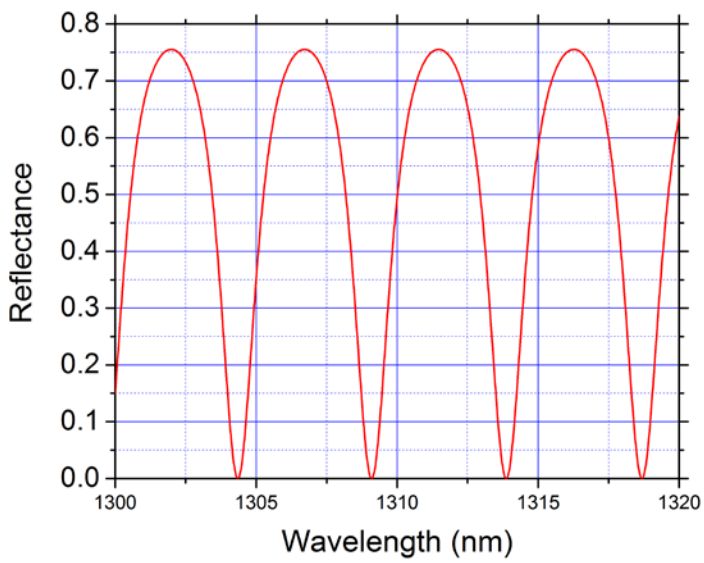

Fig. 73: Calculation of reflectance of vacuum cavity in Si (corresponding to the cavity between the inside surface of the sensor die cap and the resonator) with a gap of 160 μm as a function of wavelength.

As a result, a distributed feedback read laser diode[28] was installed in this apparatus with a linewidth specified to be typically 50 kHz, corresponding to 0.0004 pm, and a typical output power of 40 mW.

In addition, for the previously captured data, the Fourier transform was calculated by averaging the square root of the sum of the squares of the sine and cosine transforms for each scan. This

was done under the assumption that the various frequency components of each scan would have random phases from scan-to-scan. By averaging the raw time scan data, any signal with a random phase from scan-to-scan would eventually average to zero. However, it was subsequently discovered that the signal frequency components in each scan maintain a nearly constant phase relation with respect to the laser pulse, so individual time scans can indeed be averaged *before* performing the Fourier transform. This has three effects. First of all, random noise sources average to zero, while the signal frequencies do not. Secondly, the background noise level also averages to zero rather than to a nonzero level. In Fig. 66(b), for example, it can be seen that there are no negative signal values, and even the average noise level is significantly greater than zero, because taking the square root of the sum of the squares of cosine and sine transforms to generate the frequency spectrum always produces positive values for both signal and noise. By averaging time scans first before performing the Fourier transform, the background noise tends to go to zero. Thirdly, data capture and calculation are faster when the Fourier transform of each scan does not need to be calculated before averaging is performed, but only one Fourier transform at the end of the data acquisition after averaging of the raw data.

An example of a time-averaged scan with the new read laser is shown in Fig. 74. This scan is a result of 1000 averages at a 2 Hz repetition rate, for a total time of 8.3 minutes. The exponential ring down decay of the resonator is clearly evident. The 1/e ring down time constant is ~150 ms. This is in line with expectations for this sensor with a Q factor on the order of 10,000 and a resonant frequency of 12 kHz.

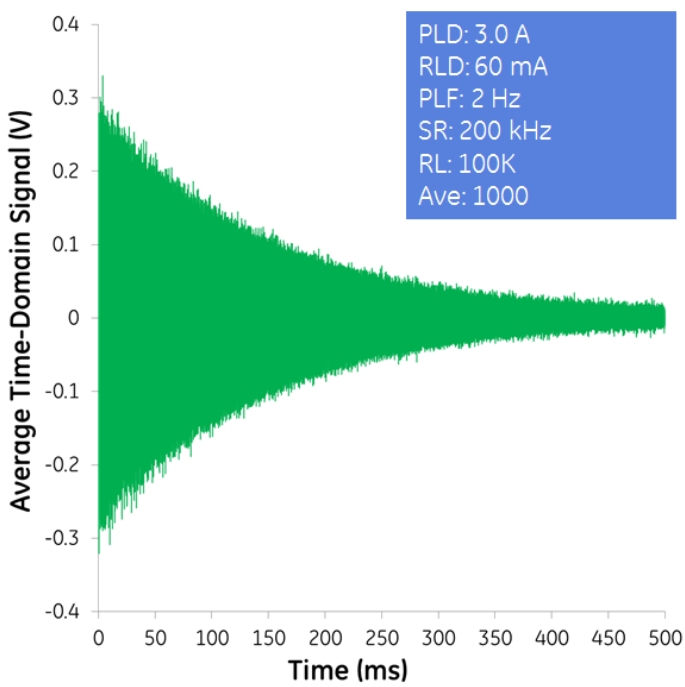

Fig. 74: Time-averaged scan of reflected light from 1000 scans between laser pulses. The approximate 1/e ring down time constant is 150 ms.

The characteristic ring down time has an exponential dependence,[29]

$$a(t) = a_0 \exp(-{}^{t}/_{\tau}) \tag{4}$$

where

$$Q = \pi\, f_0\, \tau. \tag{5}$$

From Eq. (5), we would predict $\tau \cong 270$ ms for a sensor Q of 10,000. Therefore, the Q factor for this sensor is probably closer to 5000.

The Fourier transform of the data in Fig. 74 is shown in Fig. 75.

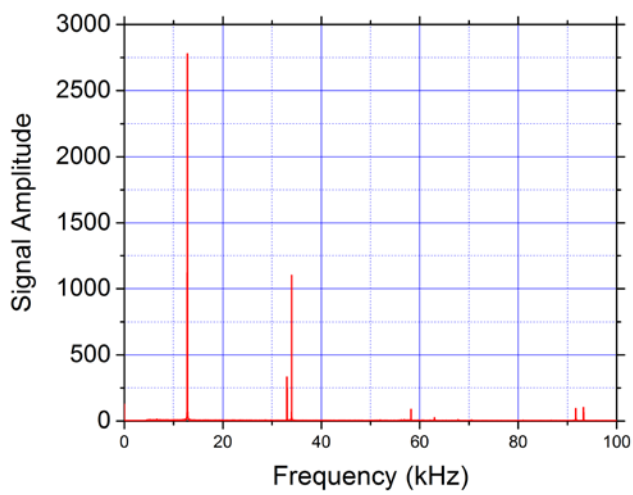

(a)

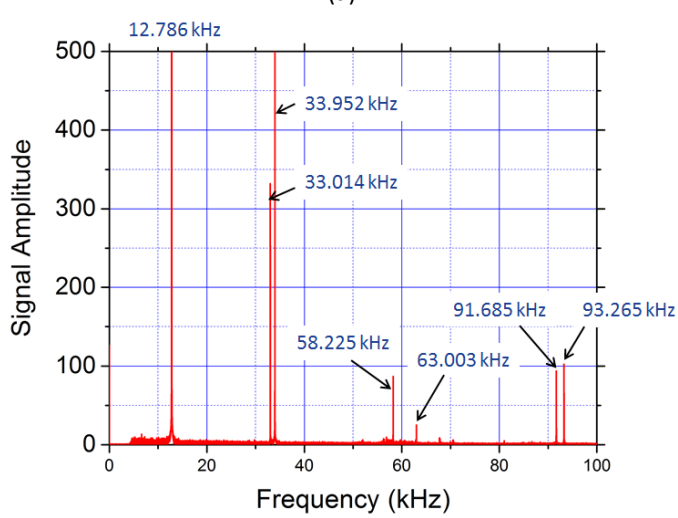

(b)

Fig. 75: (a) Fourier transform of time-averaged data in Fig. 69. (b) Expanded vertical scale showing resonant modes.

Multiple resonant frequencies of the sensor are now clearly visible with SNR~500 for the primary resonance at 12.8 kHz. The importance of being able to measure multiple resonant frequencies is that this should enable simultaneous determination of pressure and temperature of the sensor – particularly if the sensor resonator is designed with multiple eigenmodes that have substantially different temperature and pressure dependencies.

In order to test the capability for multiplexing, a 50/50 beamsplitter was installed in the setup as shown in Fig. 69. This has the effect of reducing the laser pulse power to each sensor by 50% and reducing the readback signal by 75%. When one side of the splitter was shunted to a beam dump and the other to a sensor die, the vibrational spectrum that was measured is shown in Fig. 76(a). When the beam dump as replaced with a second sensor die and the first die was replaced with the beam dump, the spectrum in Fig. 76(b) was obtained. Finally, when both sensors were attached to the splitter, the spectrum in Fig. 76(c) was obtained. All vibrational modes of both sensors are observable and distinguishable, thereby confirming that this technique can be multiplexed for at least two sensors using simply a power splitter rather than needing to use wavelength division.

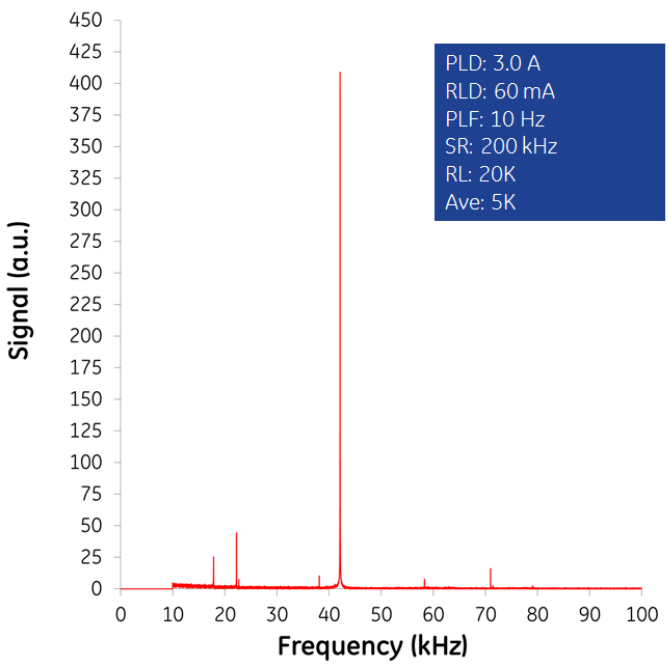

(a)

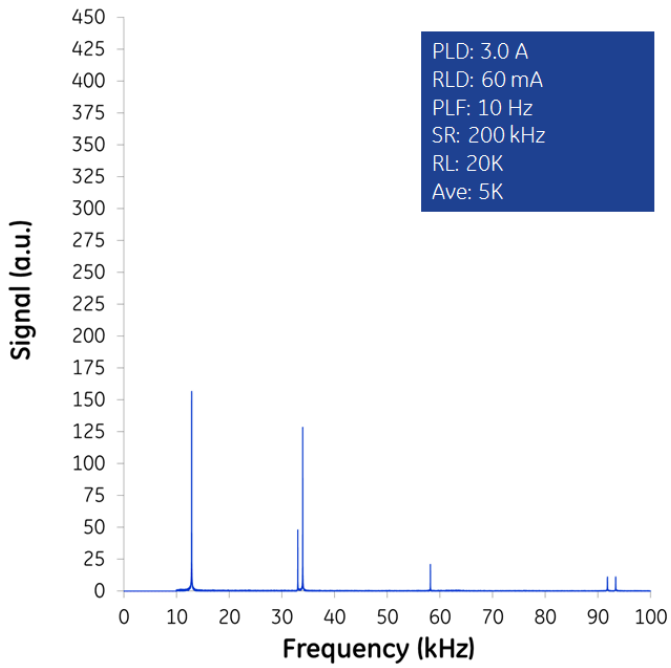

(b)

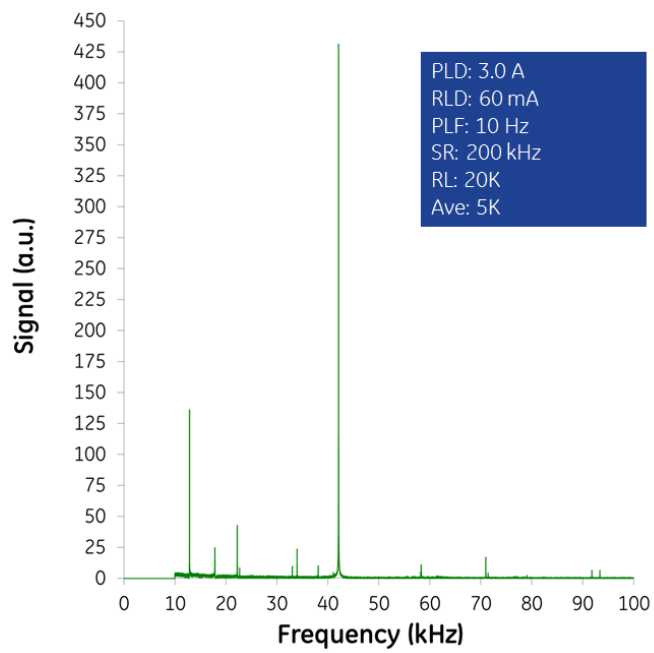

(c)

Fig. 76: Fourier transform of the average of 5000 scans taken with a 10 Hz repetition rate (8.3 min scan) using a 50/50 splitter with (a) sensor die J2 and a beam dump, (b) sensor die J3 and a beam dump, and (c) sensor die J2 and J3.

In a second experiment, a 10/90 splitter was used with a beam dump placed on the 90% side and the J2 sensor die connected to the 10% side. In this situation, the laser pulse power to the sensor die is only 10% of the incident pulse power and the readback power is < 1% of the incident power. Nevertheless, as shown in Fig. 77, it was still possible to measure the primary vibrational mode of one sensor die, and multiple modes of a second sensor die.

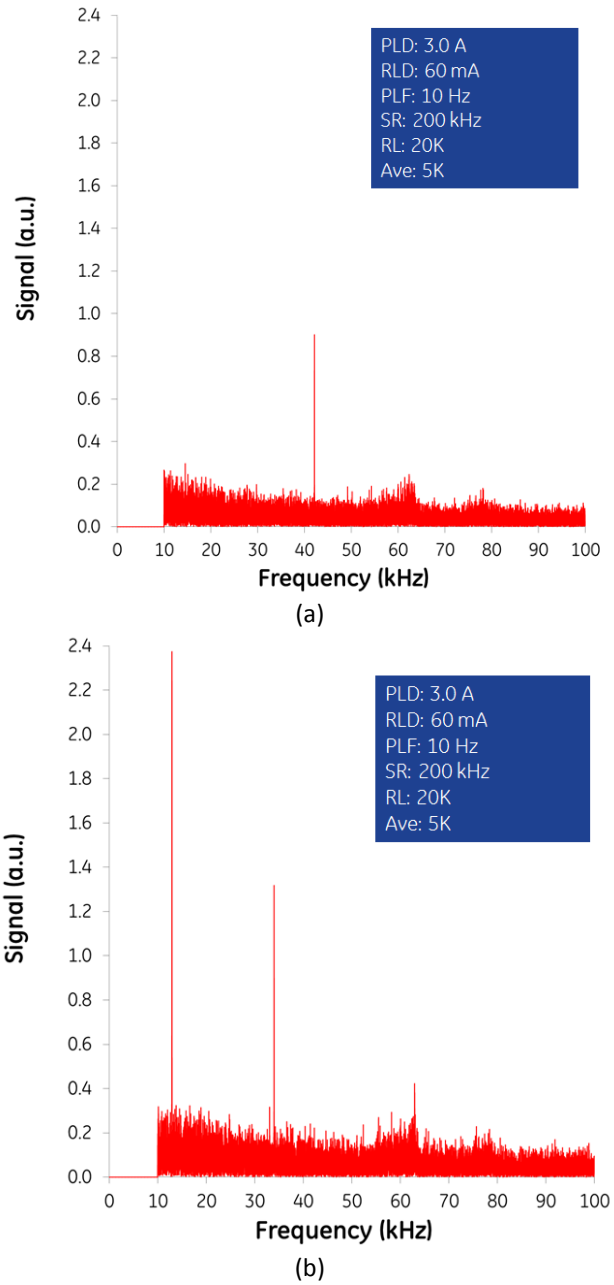

Fig. 77: Fourier transform of the average of 5000 scans taken with a 10 Hz repetition rate (8.3 min scan) using a 10/90 splitter with (a) sensor die J2 on the 10% side or (b) sensor die J3 on the 10% side, and a beam dump on the 90% side.

If the beam dump is replaced by other sensors, then the readback background light level will be ~10 times higher, which introduces additional noise into the scan and increases the required scan averaging time.

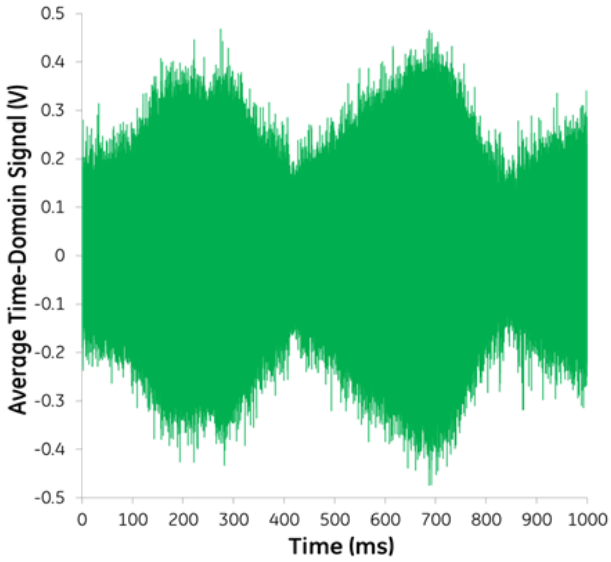

(a)

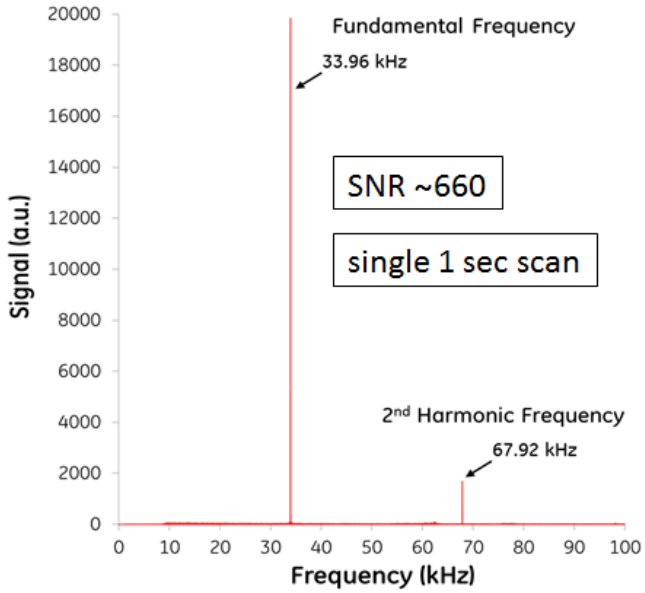

(b)

Fig. 78: (a) Read out signal from a continuously oscillating sensor using only a CW read laser. In one case, the sensor was found to oscillate for several days without change. (b) Fourier transform of signal exhibits a dominant single frequency as well as some higher harmonics.

Finally, one unexpected result was discovered when working with the pulsed laser interrogator. When the optical fiber was especially well aligned to the sensor die, there were times when a CW read laser with no pulsed laser component was also found to generate a modulated read back signal. An example of one such measurement is shown in Fig. 78.

The explanation of this unusual effect was finally realized. As shown in Fig. 79(a), the reflectance of the cavity formed by the resonator and the sensor cap is a periodic function of the gap between them. Therefore, the amount of light absorbed by the resonator is the inverse function of this.

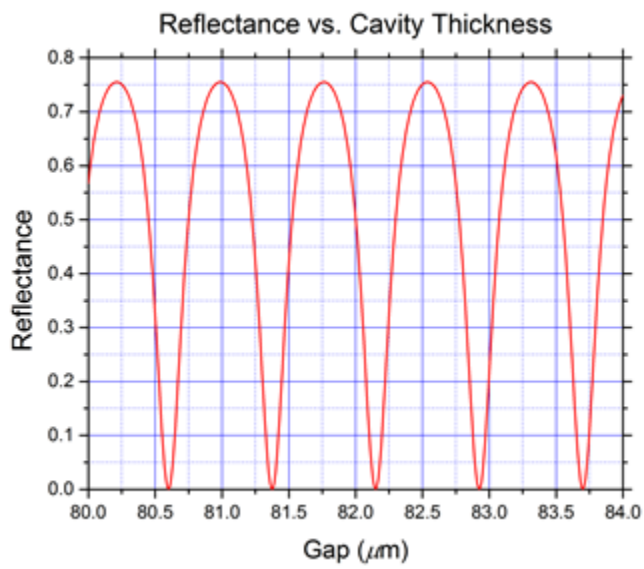

(a)

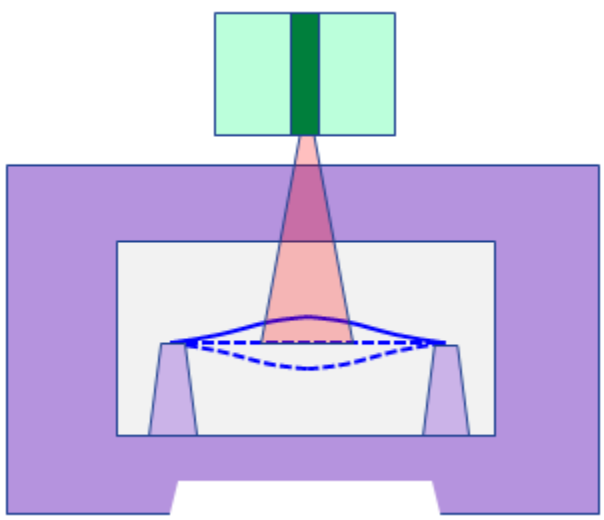

(b)

Fig. 79: (a) Calculation of reflectance as a function of resonator-to-cap distance. (b) Vibrating resonator causes the gap distance to change periodically.

As the resonator vibrates, during one part of its cycle it is absorbing energy from the laser beam and during another portion of its cycle it absorbs much less energy. Due to thermal expansion from heating, the absorbed laser light causes the resonator to bend, and if the right phase relationship can be established between the thermal bending and the optical absorption, then the oscillation can be self-sustaining. This effect has also been discussed in the literature.[30,31,32,33,34]

E. WDM/Splitter combination for downhole multiplexing

As previously mentioned, WDMs cannot be used in any interrogation approach that uses more than one laser wavelength or a broadband light source. On the other hand, splitters cannot be used by themselves with many sensors because of the drop in readback signal with the square of the number of sensors. However, a combination WDM/splitter system was devised that can be used to partially ameliorate the difficulties with both WDMs alone and splitters alone. By using the combination WDM/splitter as shown in Fig. 80, it may be possible to extend the conventional interrogation approach to many more sensors on the same optical fiber. The SM couplers/splitters are replaced by WDMs for the read laser, while splitters are still used for the drive laser. This approach requires greater complexity in the downhole fiber optics, although it is likely that all the downhole fiber components enclosed by the dashed box in the figure could be combined into a single component and still be made robust at high temperatures.

One disadvantage of this multiplexing technique is that a separate read laser or a tunable laser is required for multiplexing between sensors at different wavelengths. On the other hand, each sensor can be interrogated independently via different wavelengths, so the resonant frequencies of the sensors do not have to be multiplexed and the entire intensity of the reflected readback signal from each sensor is captured and detected separately (there is no splitter in the read path) and there is no background light in the read signal from the other sensors. This technique, therefore, should greatly enhance the signal-to-noise ratio for each sensor compared to the single splitter technique. As a result, it may be possible to use lower power, lower cost lasers for readback.

In principle it should also be possible to replace the splitter for the drive laser with a coarse WDM so that different drive lasers are used for different sensors or combinations of sensors if, for example, the drive laser does not have sufficient output power to drive multiple sensors. One can also envision a single mode, single fiber cable in which five sensors, for example, are all driven by a laser at one wavelength and read back at five different CWDM wavelengths, followed by the next five sensors driven at a different CDWM wavelength and read back at the same five CWDM wavelengths, and so on for five different drive lasers. In this manner it would be possible to multiplex twenty-five sensors on a single SM fiber using five drive lasers and five read lasers, or perhaps one tunable drive laser and one tunable read laser.

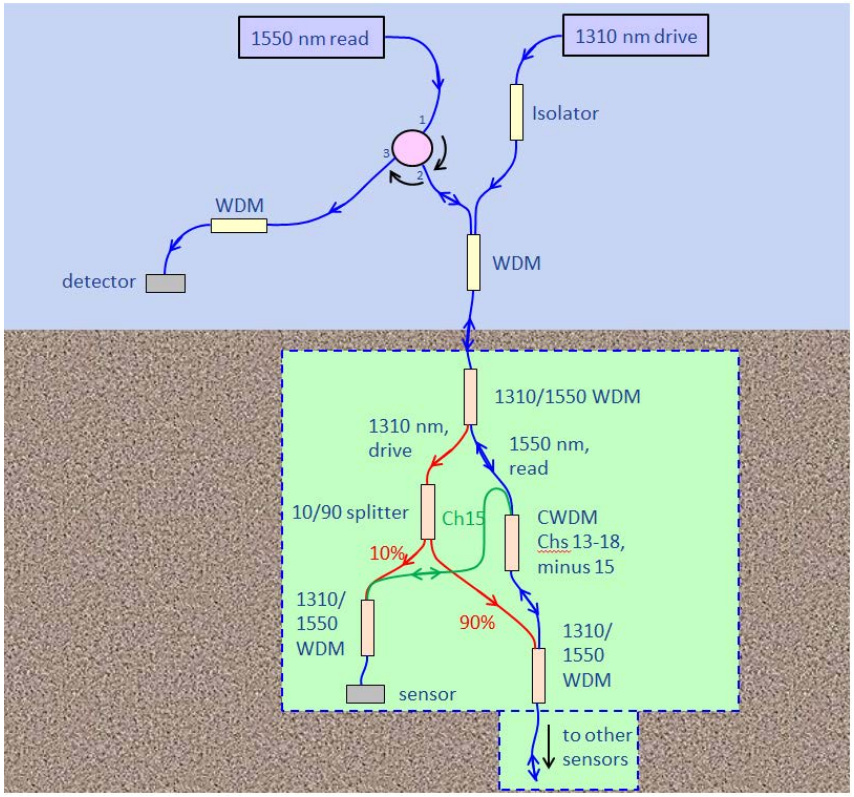

Fig. 80: Conventional interrogator concept using SM fiber with a combination WDM/power splitter downhole component for each sensor as shown in the dashed box for multiplexing.

III. Interrogator comparison and summary

In the previous section we have discussed several different multiplexing schemes. In this section we recount and summarize these schemes and compare interrogator approaches.

A. Wavelength division multiplexing

Interrogating each sensor at a different wavelength is probably the most straightforward technique for multiplexing sensors on a single fiber. There are 16 coarse WDM channels in the 1300 – 1600 nm wavelength band. This technique has certain definite advantages and disadvantages. The advantages include the high optical power delivery both to the sensor and back to the detector, since the optical power is not being divided at each sensor. A disadvantage of this approach is the necessity for an interrogator that uses a single wavelength per sensor. Therefore, only the pulsed laser interrogator is a candidate for this multiplexing technique. A second disadvantage is that a dedicated drive and read laser for each sensor can become expensive. The expense can be somewhat mitigated by making use of a tunable laser, at least for the readback, when the number of sensors exceeds somewhere in the neighborhood of 7 to 10.

B. Wavelength / power multiplexing

As described in Section II E, it is possible to combine wavelength and power division multiplexing, using power division for the drive laser and wavelength division for the read laser. This technique can be used with both the conventional interrogator and the pulsed laser interrogator. The primary advantages of this technique are that it conserves readback power by applying the most efficient wavelength multiplexing to the read laser, while only requiring a single drive laser. The disadvantage is that a more complex optical component is required downhole, and that a separate read laser is required for each sensor or a tunable laser for all sensors. It is estimated that only 4 to 10 sensors can be multiplexed at each wavelength using this approach.

C. Sensor frequency or power splitting multiplexing

The resonant frequencies of the MEMS sensors have typically very narrow linewidths, on the order of 1 to 2 Hz. Moreover, inevitable manufacturing variations cause the resonant frequencies of the sensors to vary by hundreds or even thousands of Hz even for devices fabricated on the same wafer. Therefore, if the readback signal contains resonant frequencies from multiple sensors, it is still possible to decipher which resonance belongs to which sensor. In particular, if a single laser wavelength is used for readback, and the optical power, rather than the wavelength, is split or divided for each sensor, and the reflected light from each sensor is recombined into the fiber for detection, then a single read laser can be used to interrogate all sensors simultaneously. The primary advantage of this approach is that it reduces the total number of read lasers to just one, along with a single detector. The primary disadvantage is that the read laser power from each sensor that is reflected to the surface is inversely proportional to the number of sensors squared, while the background noise power from all sensors only drops linearly with number of sensors. So the overall SNR for each sensor is inversely proportional to the number of sensors. For ten sensors on a single fiber, the reflected read power will be less than 1% of the incident laser power. Therefore, this approach cannot be used with a large number of sensors because the read signal quickly falls below the background noise level. This technique can potentially be used with both the conventional and pulsed laser interrogator approaches, and has in fact been demonstrated for the conventional interrogator approach using power splitters that split off only ¼ of the light in the fiber to a specific sensor and for the pulsed laser approach with a 50/50 power splitter. However, for the conventional interrogator approach the reflected signal was extremely small and without further improvements in SNR of the system, it would not have been possible to interrogate many more than four sensors on a single fiber. On the other hand, there is a good chance that the pulsed laser approach can be made to work with up to ten sensors in this manner. The interferometric approach does not generally work with this technique because the interference fringes from two or more sensors with the same cap thickness will overlap and make it impossible to close the feedback loop at the operating point of a specific fringe over a long time period. However, over short time periods this multiplexing technique was demonstrated for two sensors using the interferometric interrogation approach. It is likely that only four sensors at

most can be multiplexed in this manner as their resonant frequencies will start to overlap and become difficult to distinguish.

Four different interrogator approaches have been assembled and tested in the laboratory. Only one approach, the "wavelength-dither approach," was found not to work. The conventional, the pulsed laser, and the interferometric approaches have all been demonstrated in the lab for interrogating at least two sensors. The conventional approach has been multiplexed with two sensors and will likely work for up to ~4 sensors with simple power splitting or ~10 sensors using the complex WDM/splitter downhole coupler as described in Section II E. The interferometric interrogator has also been multiplexed with two sensors and can likely be multiplexed with 4-10 sensors using the cap thickness multiplexing technique. Finally, the pulsed laser interrogator has been has also been multiplexed with two sensors and multiple vibrational modes could be observed on one sensor die even when it received only 10% of the pulse and read laser light. Therefore, by combining wavelength multiplexing with power multiplexing, it is likely that ~16 × 4 or more sensors can be combined onto a single fiber.

It is also possible to multiplex by simply adding fibers to the cable. This is quite expensive as the specialty pure silica core fiber necessary for resisting the effects of hydrogen darkening is very expensive. Moreover, with more fibers, more fiber slices are required at each sensor location. Three or four fibers may be the largest practical number of fibers in a single cable. Using the pulsed laser approach, however, with three fiber it should be possible to interrogate hundreds of individual sensors on a single cable.

Task 3.1—Optical Modeling

Prior to constructing the pulsed laser interrogator, it was essential to carry out a simple estimate of the laser power that would be required. MEMS sensors that are interrogated using a continuous sinusoidal laser drive power require a minimum of ~2 mW for the drive laser. The readback time constant which provides sufficient SNR to close the feedback loop is 1 ms. This provides an estimate of 63 μJ required over 1 second to drive the MEMS resonator.

The Q of the resonators is typically 10,000 to 20,000. If we assume the latter Q for a MEMS device with a resonance at 20 kHz, then the time constant is given by the equation

$$Q = \pi \ f_{0\tau}. \tag{6}$$

The time constant for the MEMS die is ~0.3 sec. If we average the signal for 100 sec, then the SNR increases as the square root of this time, so that we will only need about one tenth of the drive power, or 6.3 μJ. For one laser pulse/sec, the average power required is 6.3 μW.

The pulse length must be short compared to the resonant frequency. Because the MEMS devices may have resonances up to ~80 kHz, we require a pulse length of 5 μs or less. For this pulse length, the peak laser power in the pulse should be ~1.3 W, corresponding to an energy/pulse of 6.5 μJ. This compares well with the pulsed fiber laser in the interrogator that has an output energy of 40 μJ/pulse.

Task 3.2—COTS Survey and Characterization

The goal of this subtask is to survey existing COTS parts for suitability in the downhole optical cable and verify their performance at high temperatures in the laboratory. The fiber cable must contain optical components for splitting light off a single fiber to each sensor.

Commercial WDMs and splitters underwent long term survivability testing at high temperature. Power splitters from Comcore and Fiber Instrument Sales failed, but a power splitter from Gould continued to survive at 250°C for a total of 66 days. When the oven was opened in order to insert some new components, the steel casing on the Gould splitter was discovered to have come loose as shown in Fig. 89(b). In the process of removing the failed splitters from the oven, the loose steel casing on the Gould splitter, which was otherwise still working as shown in Fig. 90, slipped and broke the fiber extending out the right side of the splitter in the photo, unfortunately precluding continued testing of the part. For actual downhole operation, these parts would be ordered without the steel casing and the glass shell would be placed directly within the sensor package to avoid this problem.

(a)

(b)

Fig. 89: Gould high temperature splitter (a) before high temperature testing, and (b) after removal from oven following testing for 69 days at 250°C.

Although Gould does not sell COTS WDMs for high temperature, Gould was contacted to see if they could fabricate custom parts for this project. As a result, Gould was able to develop and provide 5 WDMs for testing. The components make use of the same high temperature fusing process that is working successfully for their splitters at 250°C, but the WDMs are not guaranteed for high temperature operation as these are just prototypes. The parts were tested for >1600 hours at 250° as shown in Fig. 91 without failing.

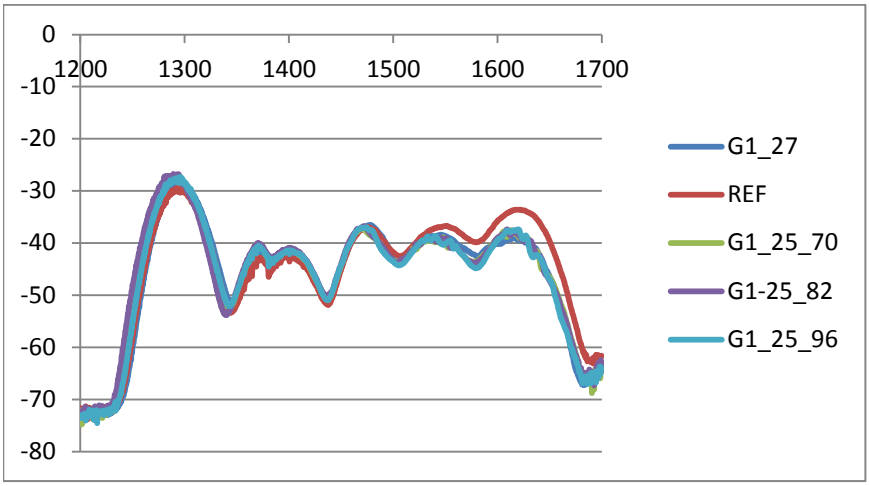

(a)

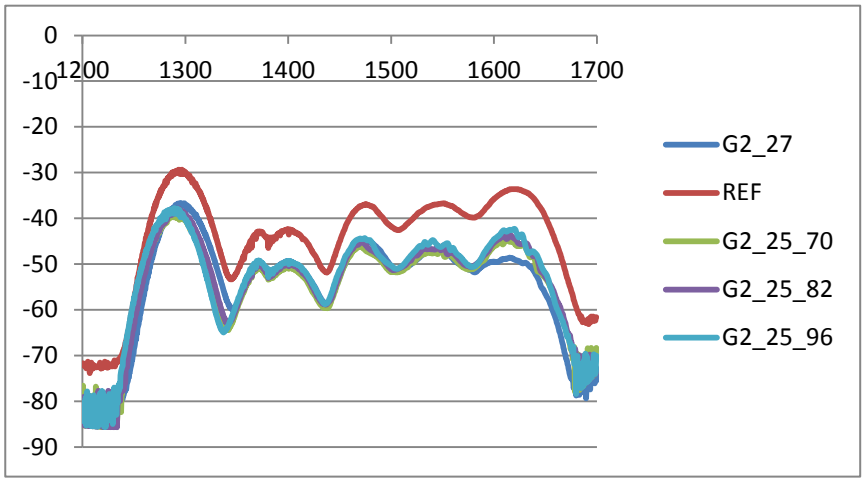

(b)

Fig. 90: (a) and (b) are spectral transmittances measured through either side of a Gould 50/50 splitter. Red curves are the initial spectra. The other curves are measured after 27, 70, 82, and 96 days, respectively. For the first 30 days, the splitter was at 200°C. The remainder of the time the splitter was at 250°C.

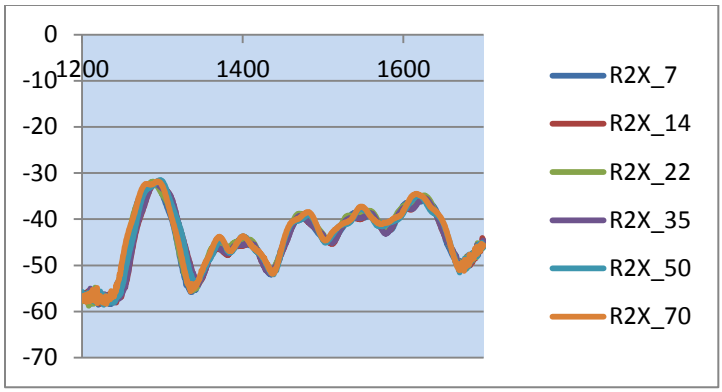

(a)

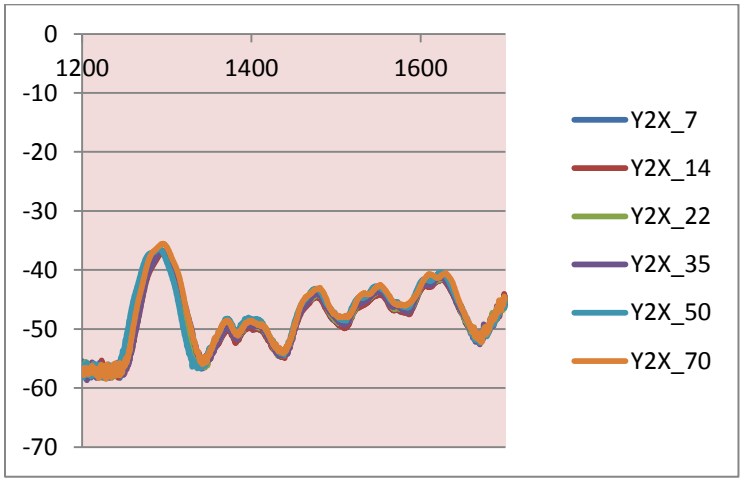

(b)

Fig. 91: Graphs (a) and (b) are spectral transmittances measured through two Gould WDMs in an oven at 250°C. The final number in the graph label indicates days at temperature. There is no significant variation in the spectral transmittance with time.

The original couplers supplied by Comcore were only rated for 200°C maximum temperature and, not surprisingly, they did fail at 250° as shown in Fig. 92.

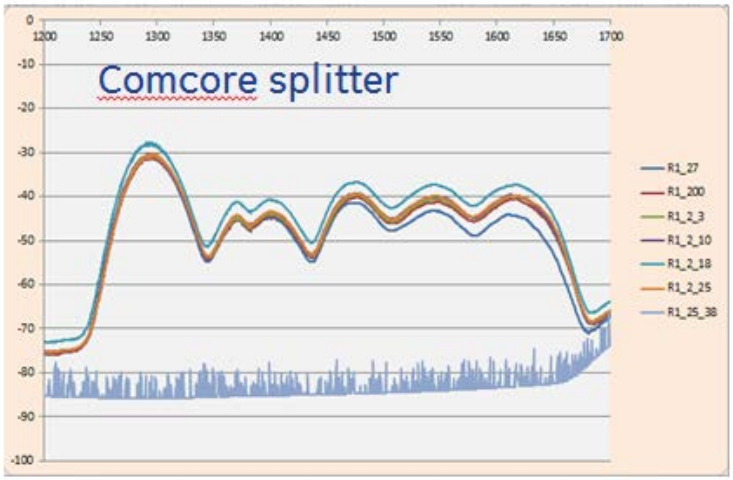

Fig. 92: Splitter from Comcore tested at 250°C. The final number in the graph label indicates days at temperature. The splitter survived 30 days at 200°C, followed by 7 days at 250°C, before finally having been found to fail before 11 days at 250°C.

As a result of this test, Comcore specially developed a new high temperature splitter as shown in Fig.93 and provided this for testing just prior to the end of the project.

Fig. 93: New high temperature splitter developed for Comcore rated for 250°C

These splitters were placed in the oven at 250°C. After 42 days of testing, they exhibited no degradation in their transmittances as shown in Fig. 94. There does appear to be an increase in transmittance over some wavelength ranges, although it is not clear what this is due to, and the transmittance has evidently stabilized.

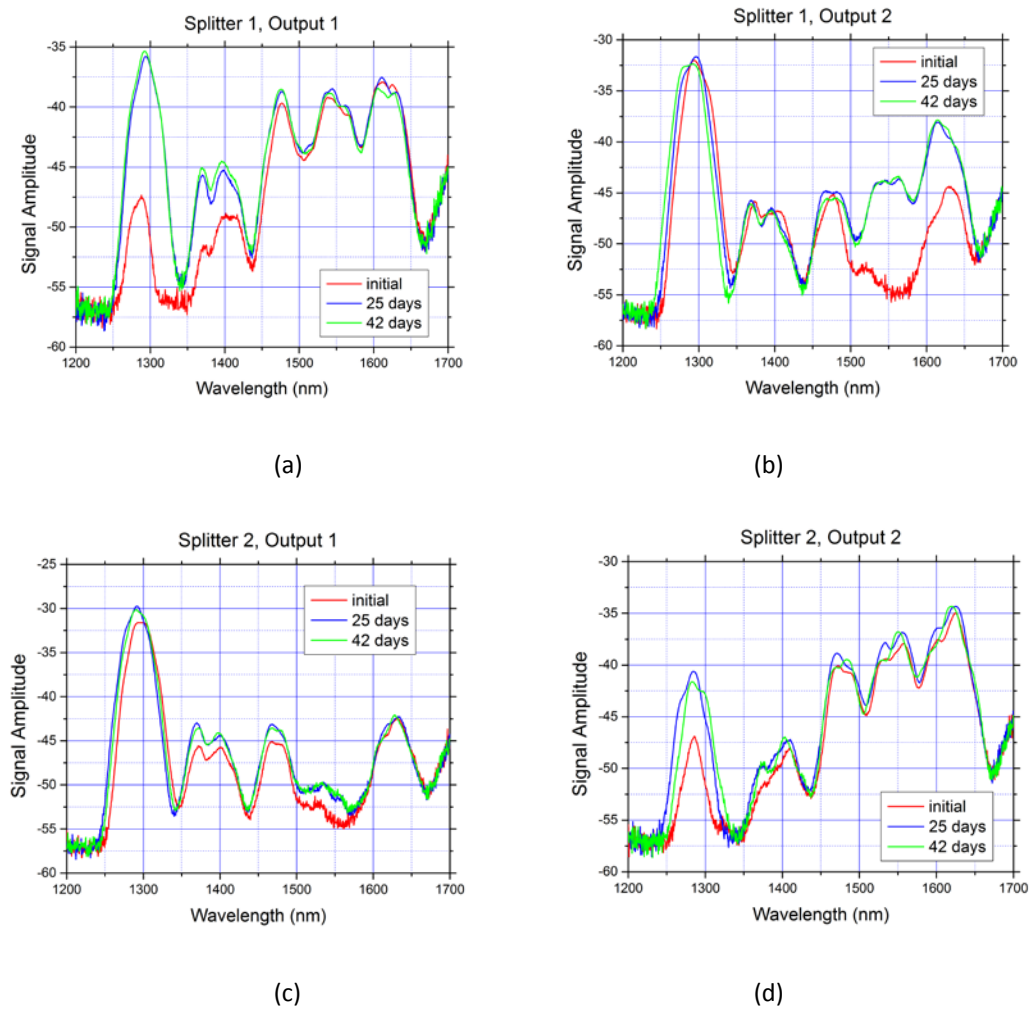

Fig. 94: Graphs (a) and (b) are spectral transmittances measured through each output of a high temperature Comcore 50/50 splitter in an oven at 250°C. Graphs (c) and (d) are for a second splitter. There is no degradation in transmittances over the 1000 hour measurement.

Task 4: Fabricate and Test Fiber Sensor Cable

Task Completion Date: 12/31/2014
% Complete: 100%

The main deliverable for this task is a report describing fabrication of the fiber cable with two or more MEMS sensors, particularly describing the splicing technique, the equipment and technique for testing the survivability of the sensor as it passes over the sheave, the outcome of

the testing of the mechanical integrity of the cable, sensor, and splicing, and the results for the lifetime estimate from accelerated testing of cable and sensor.

Two sensor packages as shown in Figs. 95(a) and (b) were completed during the final quarter of the project and spliced onto a single fiber within a section of ¼” stainless steel cable as shown in Fig. 95(c) that had been removed from a cable that had been previously deployed for a downhole measurement.

(a)

(b)

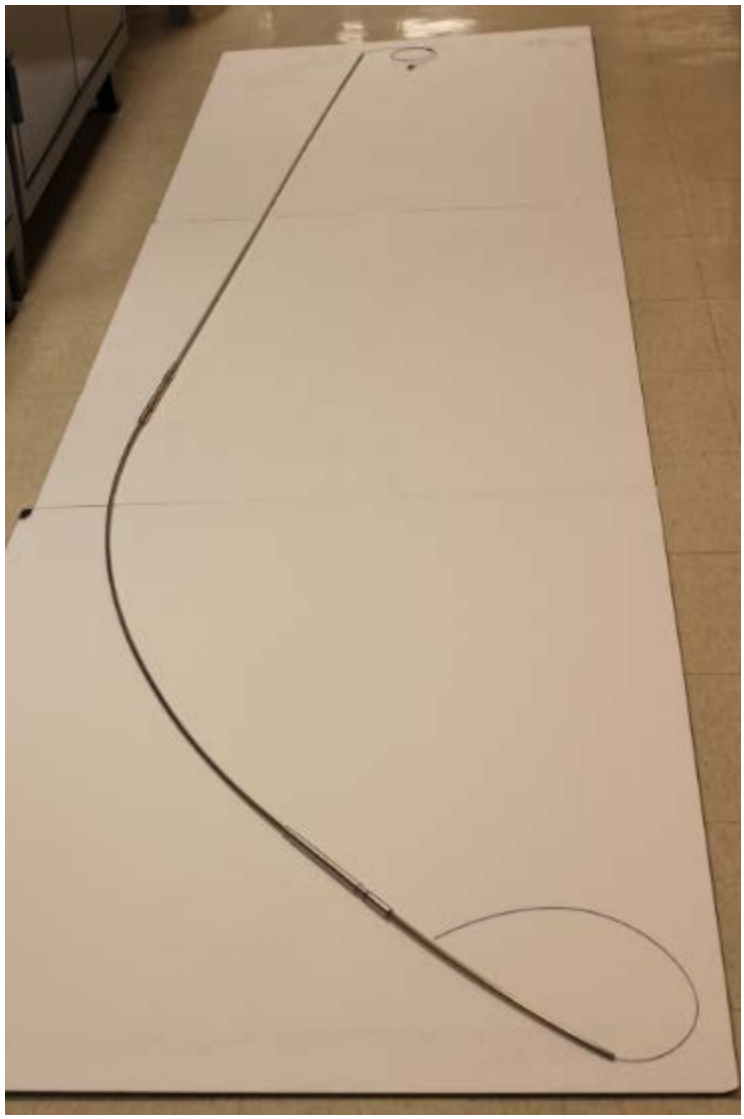

(c)

Fig. 95: (a) Early version of sensor package containing a low Q sensor die for high pressure, high temperature testing, (b) final version of sensor package containing a high Q sensor die for sheave stress testing, and (c) both sensor packages spliced onto a single fiber and connected with standard ¼" segments of downhole stainless steel tubing. Light is injected through the fiber connector at the top of the photo to interrogate both sensors. The fiber emerging at the bottom of the photo from the cable is for illustration only. During assembly of the lower sensor package in the photo, the "pass through" fiber for this package was broken.

The fiber cable with both sensors shown in Fig. 95(c) was brought into the lab and connected to the pulsed laser interrogator, and both sensors were *simultaneously* measured. The results are shown in Fig. 96.

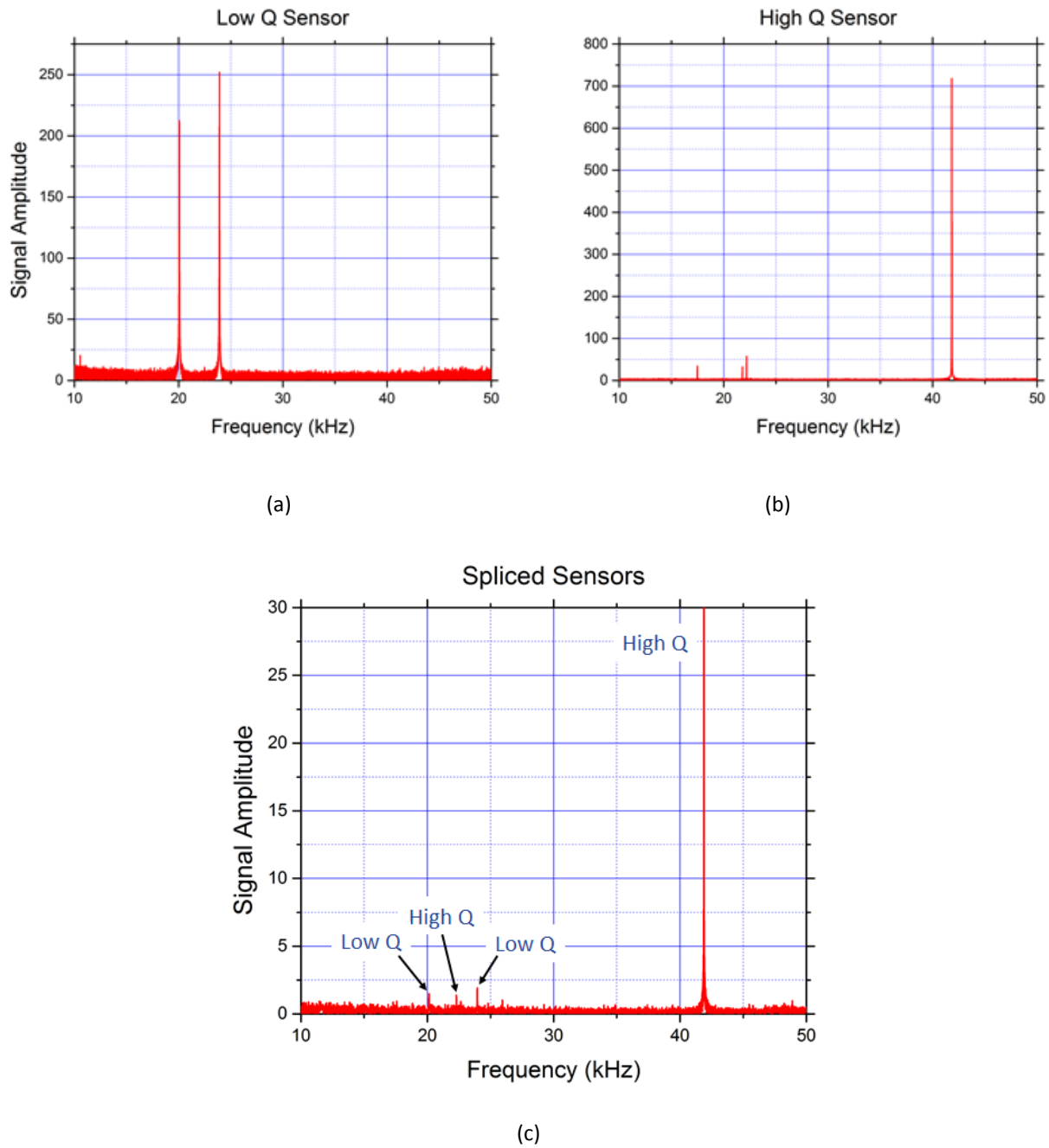

Fig. 96: Sensor signals after welding the package from the individual (a) low Q and (b) high Q sensor die. (c) Sensor signals from spliced sensors using a 50/50 power splitter demonstrating the dramatic improvement in SNR of the high Q sensor die over the low Q sensor die.

One of the two sensor die was from an earlier lot of dies developed under a previous single point sensor project. This die had a high Q ~10,000, indicating that there was a good vacuum within the die package. This sensor had an extremely strong and narrow resonance at 41.836 kHz, as well as three smaller resonances at 17.481, 21.785 and 22.192 kHz as shown in Fig. 96(b). However, this sensor die was only designed in the earlier project for a peak pressure of 3000 psi

and did not have an attached Si spacer to isolate it from external stresses. Therefore, this sensor package was subsequently used for the sheave mechanical stress test rather than the high temperature, high pressure environmental test.

The second set of sensor die were especially developed and fabricated by the GE Measurement and Control business for this project in order to withstand the 10 kpsi pressures and 250°C temperatures involved in this project as shown in Fig. 97. Therefore, one of these sensor die was used in the sensor package for the high temperature and high pressure testing.

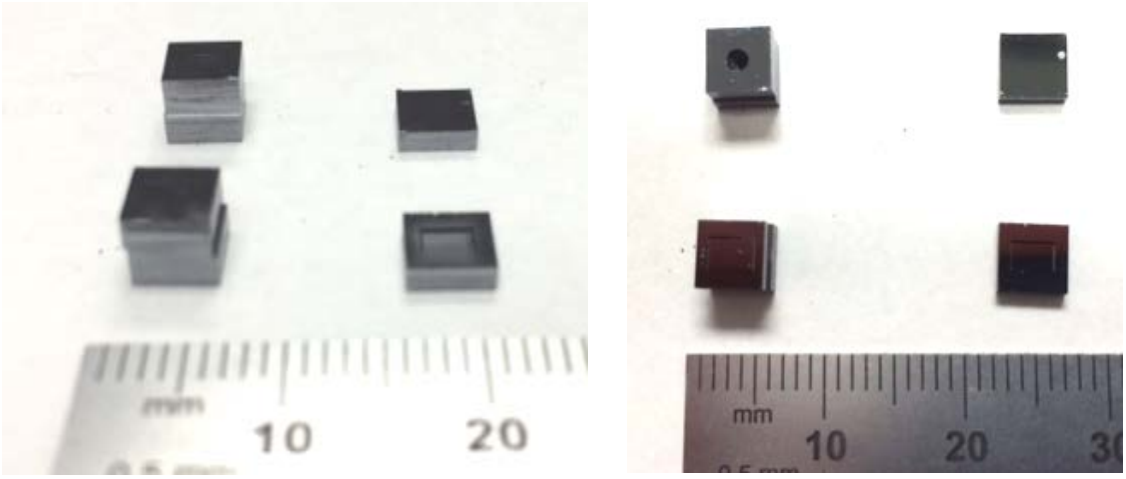

(a) (b)

Fig. 97: (a) Side view and (b) top view of new sensor die attached to Si spacer (left) and old sensor die without spacer (right). Back row in (a) and top row in (b) are the top surfaces of the sensor die, while front row in (a) and bottom row in (b) are the back surfaces o the sensor die. As can be seen in the upper left die in (b), the spacer has a 1 mm hole in the center to allow access for the optical fiber to the die. The back side of both die have a shallow well that adjusts the thickness of the bottom Si cap and hence the sensitivity of the sensor to applied pressure. The slight offset visible in the die on the far left is a result of imperfectly aligned dicing of the die from top and bottom, but has no effect on sensor performance.

Unfortunately, all of the high pressure sensor die fabricated by GE Measurement and Control exhibited low Q ~200 to 1000 due to problems during manufacture that led to a poor vacuum within the sensor die. These sensor die, therefore, exhibited much smaller and broader signal resonance amplitudes than those of the earlier die. The low Q die used for the second sensor package had two resonances at 20.062 and 23.913 kHz as shown in Fig. 97(a).

Four resonances are visible in Fig. 97(c) in the signal frequency measurement using the pulsed laser interrogator with the two sensor packages spliced onto the same fiber within a single cable. The resonant frequencies are 20.136, 22.295, 23.949, and 41.895 kHz. The dominant resonance at 41 kHz is from the high Q sensor and illustrates the large improvement in signal-to-noise ratio (SNR) that is possible with high quality sensor die. Nevertheless, it was still possible to track the resonant frequencies from the low Q sensor for the subsequent temperature and pressure

measurements even with the lower SNR. For multiplexing sensors on a single cable, however, it will be extremely important to have sensor die with high Q so that signals can be obtained with sufficient SNR even when power splitters are used for the multiplexing technique.

After demonstrating multiplexing of the two sensor packages onto a single fiber, the packages were again separated.

A. Pressure / temperature testing

The sensor package with the low Q sensor die designed for 10 kpsi was placed within a high pressure chamber inside of the oven as shown in Fig. 98.

(a)

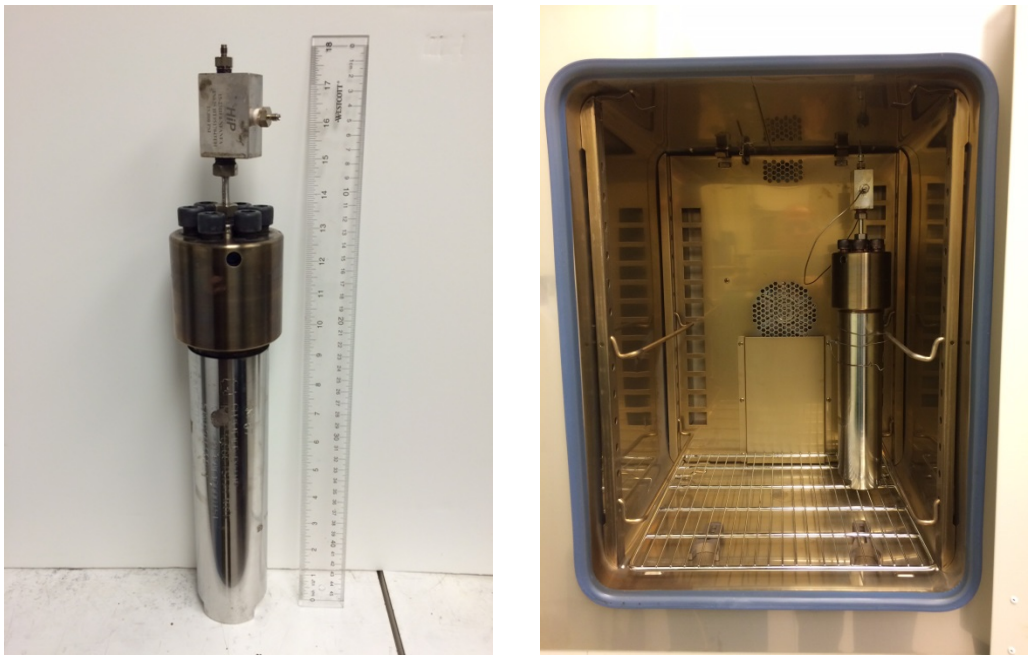

(a) (b)

Fig. 98: (a) Environmental chamber for sensor calibration / testing. The oven on the left can be set between 50 and 250°C. The unit in the center of the table is the syringe pump which can generate pressures up to 10 kpsi. The unit on the right is a water chiller to maintain the temperature of the syringe during compression at ~5°C. The CO_2 gas cylinder is on the left. The pump and plumbing are contained behind a plexiglass / sheet steel shield. (b) High pressure vessel made of Inconel 625 and rated for 15 kpsi. Fiber from sensor emerges through 1/16" stainless steel tubing from top of rectangular block above the pressure vessel. The tubing passes through the block into the vessel and is welded to the sensor package. Gas is injected through right side port of block and flows inside of 3/8" tube connecting rectangular block into pressure vessel, and around outside of 1/16" tubing containing the fiber. (c) Pressure vessel installed in oven. A 1/16" stainless steel tubing from syringe pump which carries the high pressure CO_2 is visible connected to side port of rectangular block above vessel. Both 1/16" tubes – for the fiber and the the pressurized CO_2 – exit the oven through a small opening in the back, not visible.

The fiber from the sensor was gold-coated to withstand temperatures of 400+°C. After emerging from the oven, the fiber was spliced to a conventional polyimide fiber cable to carry the light ~10m to the interrogator located on a separate table. A conventional interrogator with drive and readback lasers had been previously set up on the table (as described in Task 3A, p. 44) and tested with bare sensor die. A LabView program was written to continuously monitor the sensor resonances and store the data. The resonance signals were captured by a network analyzer which scanned frequency. For these broad resonances, relatively low reslutions scans were suitable. As shown in Fig. 99, a single scan from 19 to 25 kHz with 801 points was used to determine both resonant frequencies. Scans of the individual resonances at higher resolution are also shown in the figure.

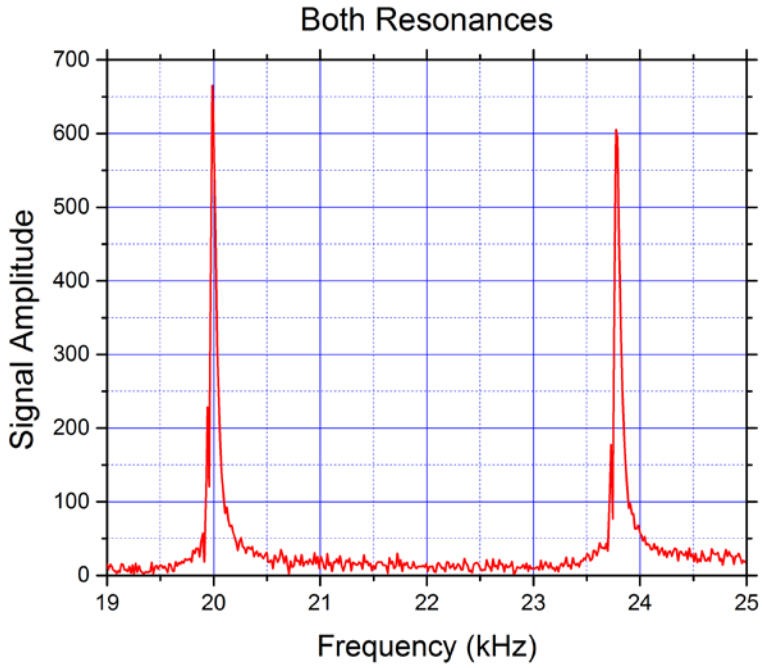
Both Resonances
Signal Amplitude
Frequency (kHz)
0
100
200
300
400
500
600
700
19
20
21
22
23
24
25

(a)

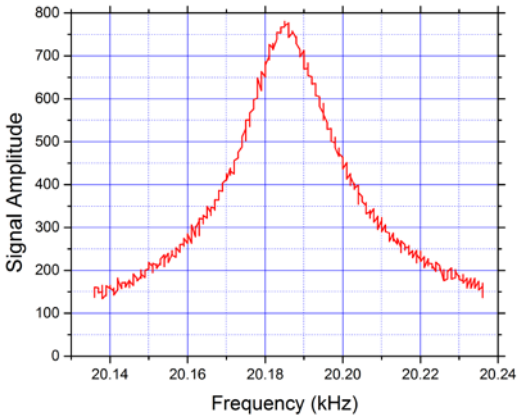
Signal Amplitude
Frequency (kHz)
0
100
200
300
400
500
600
700
800
20.14
20.16
20.18
20.20
20.22
20.24

(b)

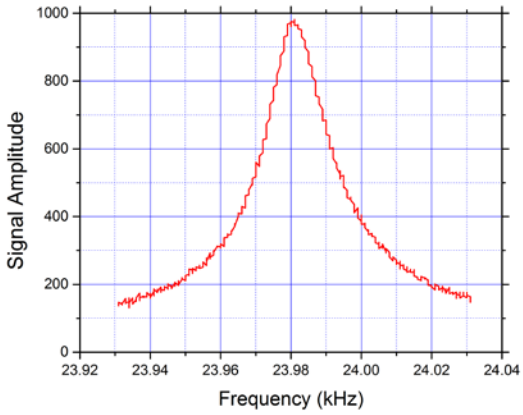
Signal Amplitude
Frequency (kHz)
0
200
400
600
800
1000
23.92
23.94
23.96
23.98
24.00
24.02
24.04

(c)

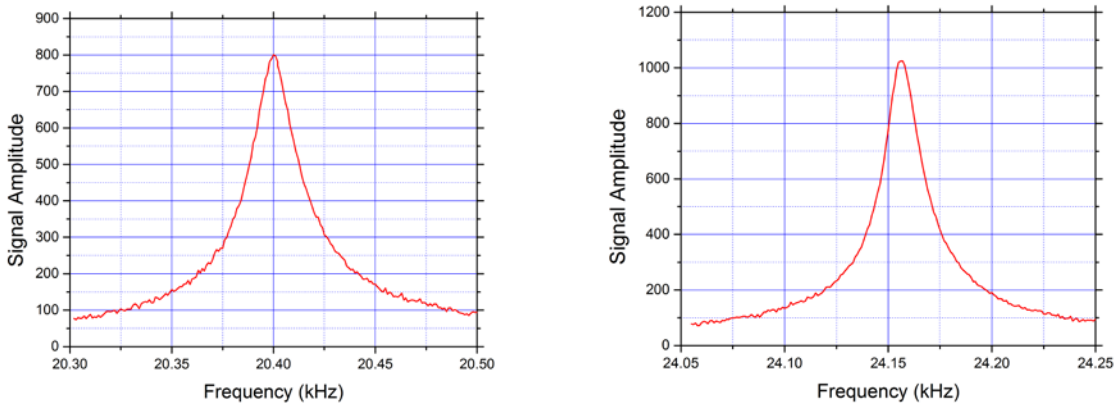

(d) (e)

Fig. 99: (a) Single frequency scan of network analyzer used to determine frequencies of both sensor resonances. (b) and (c) higher resolution scans of individual resonances. These scans were measured at room temperature and 0 psi, and integrated for ~1 min to improve the SNR. However, at other temperatures and pressures the SNR could be much higher, as shown in (d) and (e) which were measured at room temperature and 500 psi.

The mass of the pressure vessel is quite large, ~50 kg, and consequently although the oven reaches its setpoint within minutes, the vessel itself takes several hours to equilibrate as shown in Fig. 100 which is a plot of resonant frequencies as a function of time for a 25°C tempeature change in the oven. Therefore, it was decided to make all measurements after the oven had stabilized for at least twelve hours at its setpoint, and to vary the CO_2 pressure applied to the sensor. CO_2 pressure changes of course will also entail a small temperature change in the sensor: compressing the fluid will generally cause a small temperature rise and vice versa, but this temperature change was sufficiently small and the CO_2 fluid inside the pressure vessel has a relatively low thermal mass so that thermal equilibration after pressure changes was achieved within minutes.

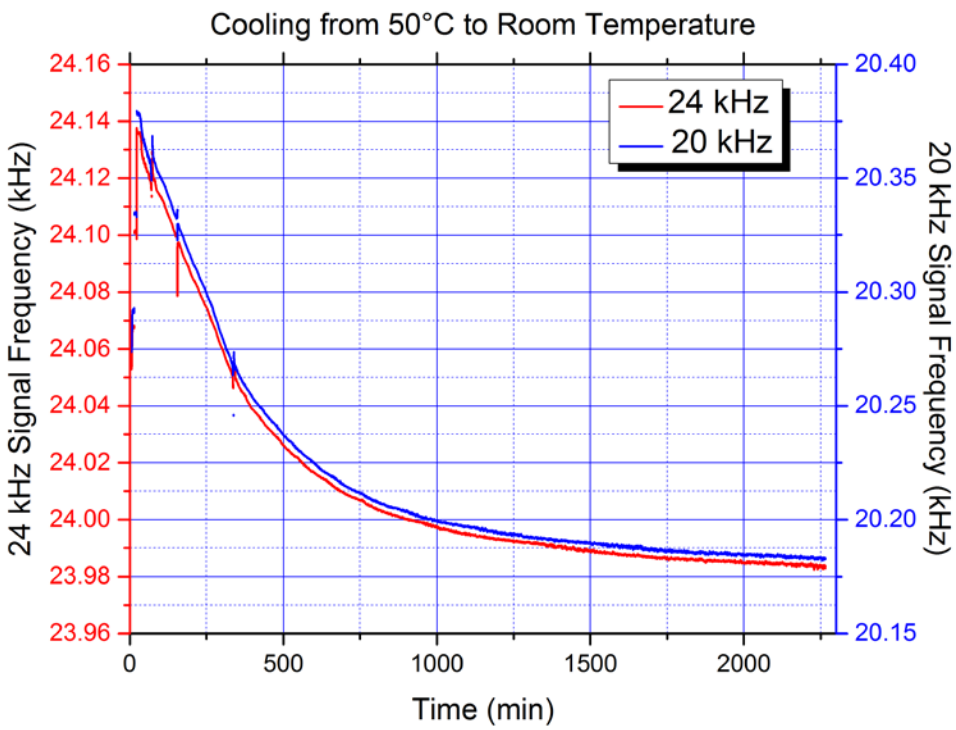

Fig. 100: Measurement of the two sensor resonant frequencies shown in Fig. 99(a) as a function of time as the pressure vessel and sensor package were cooled from 50° to 25°C. The two resonances track each other very closely.

A typical pressure ramp at constant temperature is shown in Fig. 101(a). By measuring the resonant frequencies at each pressure step after the signal has stabilized, it is possible to determine the sensitivity of the sensor to pressure as shown in Fig. 101(b). This pressure ramp appears to generate a somewhat nonlinear frequency response to pressure. However, it is possible that the pressure reading of the syringe pump meter is not accurate at these low pressures. A much more linear response was found at higher pressures.

A second pressure scan at room temperature, dropping from 500 psi to 0 psi is shown in Fig. 102(a). The signal amplitude for this interrogation approach can vary considerably as pressure or temperature is changed, and for a short time at ~point #160 the signal became too small to give reliable frequency measurements.

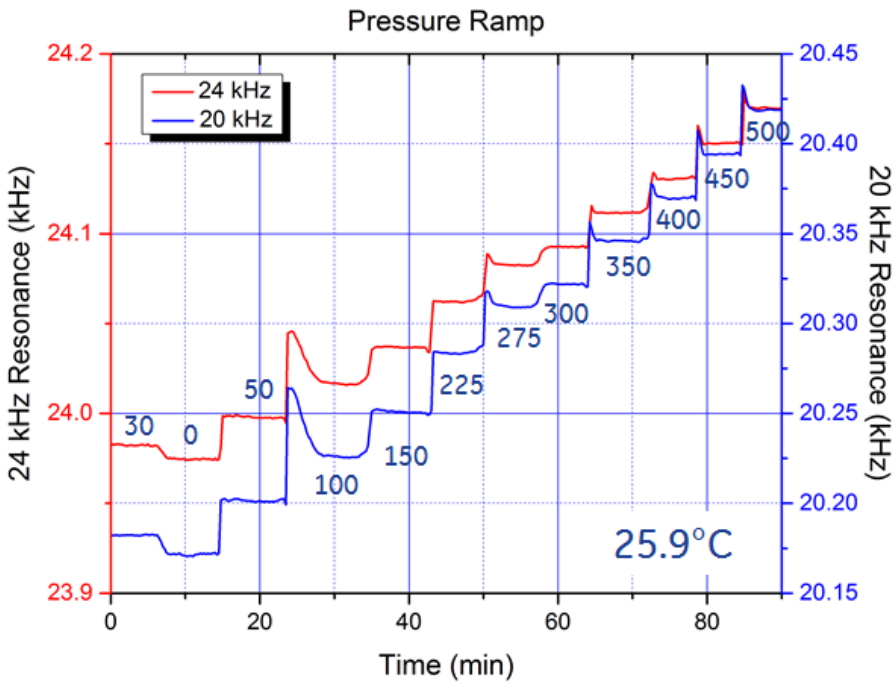

(a)

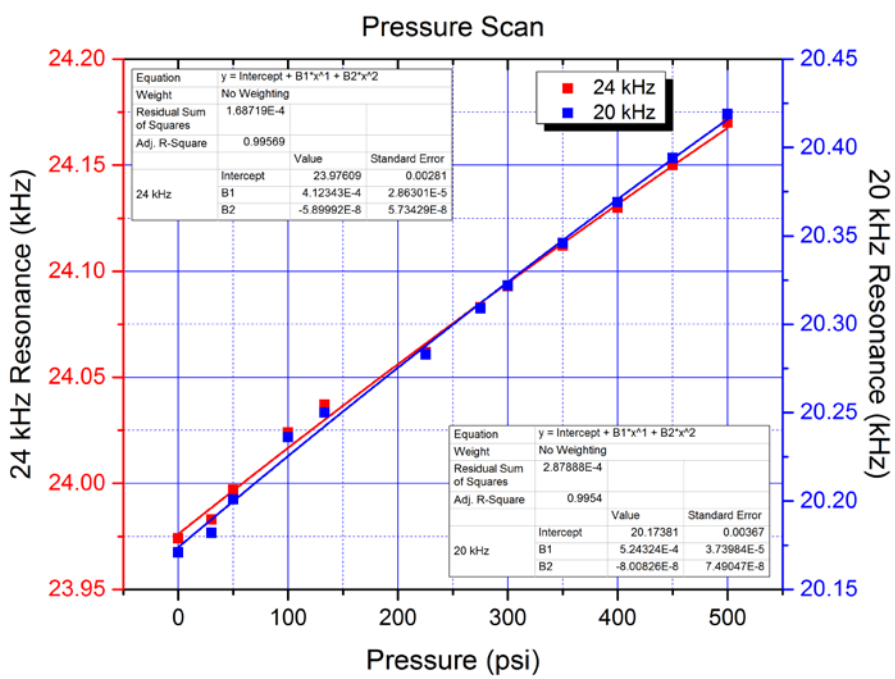

(b)

Fig. 101: (a) Variation of resonant frequencies with pressure at a constant temperature of 25.9°C as the pressure is successively stepped from 0 to 500 psi. The overshoot is caused by the PID feedback loop in the CO_2 syringe pump.

Between 50 and 100 psi, the syringe needed to be refilled with CO_2 which caused a longer delay than usual in reaching the setpoint pressure. Frequency readings measured after pressure equilibrium was reached are plotted as a function of pressure. A quadratic curve fit was applied to fit the data, though the nonlinear effect is small and may be simply due to inaccuracy of the pressure reading in the syringe pump, which is designed to work at higher pressures. The linear term in the fit corresponds to 0.41 Hz/psi for the 24 kHz resonance and 0.52 Hz/psi for the 20 kHz resonance.

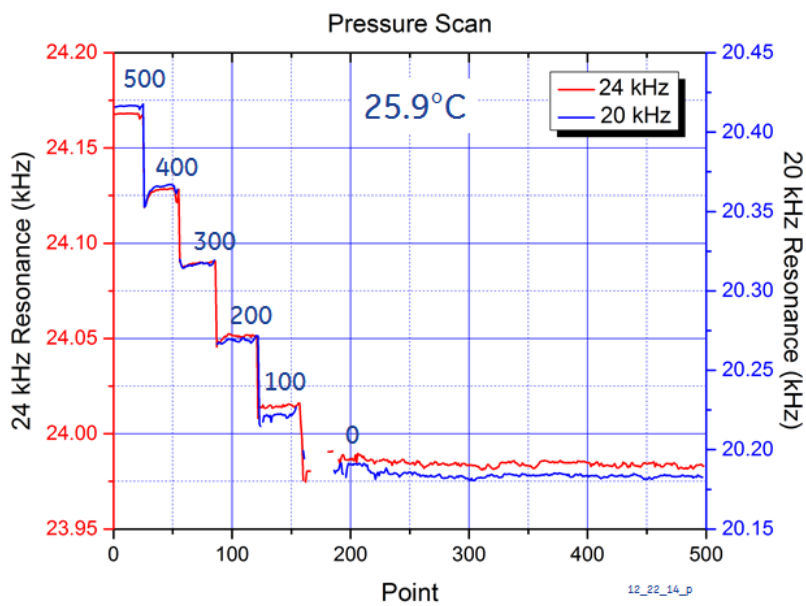

(a)

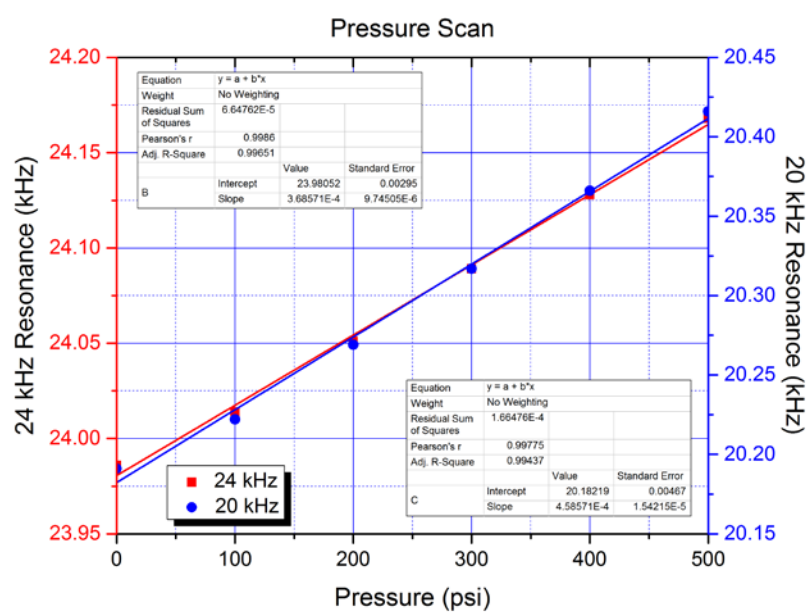

(b)

Fig. 102: (a) Variation of resonant frequencies with pressure at a constant temperature of 25.9°C as the pressure is successively stepped from 500 down to 0 psi. (b) In this case, a linear least squares fit was used to fit the data, corresponding to 0.37 Hz/psi for the 24 kHz resonance and 0.46 Hz/psi for the 20 kHz resonance.

The sensor resonances were subsequently measured at 50°C to pressures up to 900 psi as shown in Fig. 103.

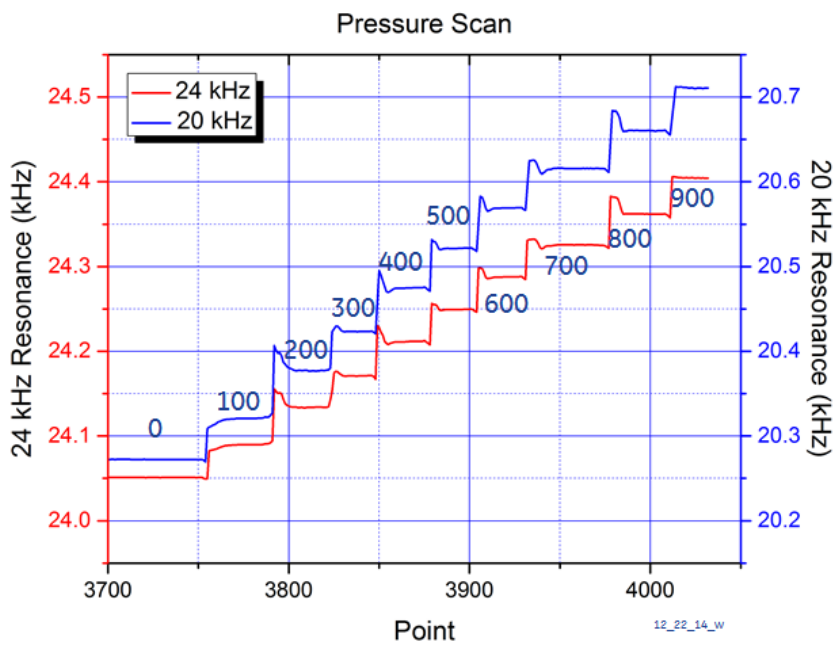

(a)

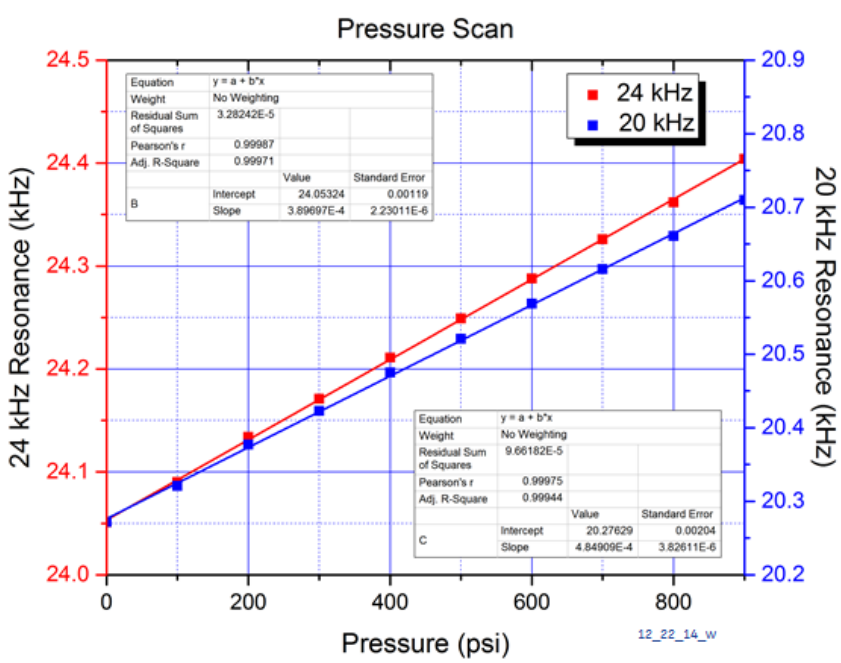

(b)

Fig. 103: (a) Variation of resonant frequencies with pressure at a constant temperature of 50°C as the CO_2 pressure is successively stepped from 0 up to 900 psi. (b) A linear least squares fit gives 0.39 Hz/psi for the 24 kHz resonance and 0.48 Hz/psi for the 20 kHz resonance.

The oven temperature was again raised to 100°C and allowed to stabilize overnight. The data are shown in Fig. 104.

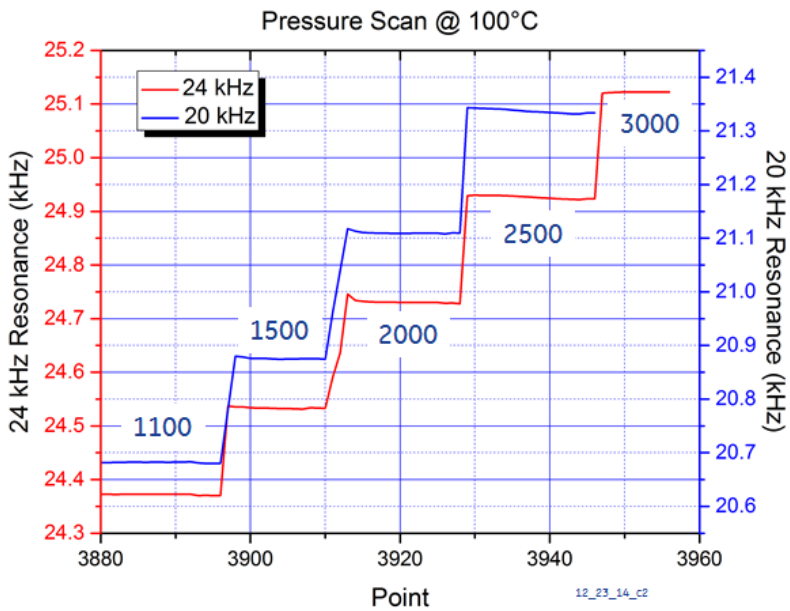

(a)

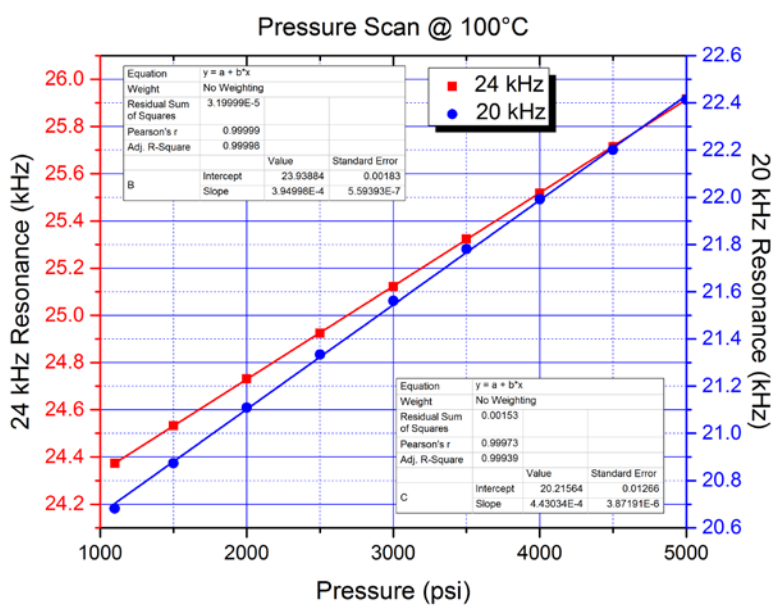

(b)

Fig. 104: (a) Variation of resonant frequencies with pressure at a constant temperature of 100°C in sc-CO_2 as the pressure is successively stepped from 1100 up to 3000 psi. (b) On the following day, the pressure was increased to 5000 psi to collect additional data for the linear least squares fit, which gives 0.39 Hz/psi for the 24 kHz resonance and 0.44 Hz/psi for the 20 kHz resonance.

At the temperature of 100°C, after the pressure had been raised to 5000 psi for ~50 minutes, the syringe pump began to slowly compress to maintain a constant pressure indicating that a leak may have developed in the package. In order to attempt to acquire a pressure reading at 5000 psi and a higher temperature, the oven temperature setpoint was then set to 200°C. After ~10 minutes, however, the CO_2 pump syringe level began dropping more quickly and a "hiss" from a leak was actually audible outside of the oven. The resonance signal level dropped precipitously as shown in Fig. 105 and did not recover even after reducing the pressure and temperature back to 0 psi and 25°C, respectively.

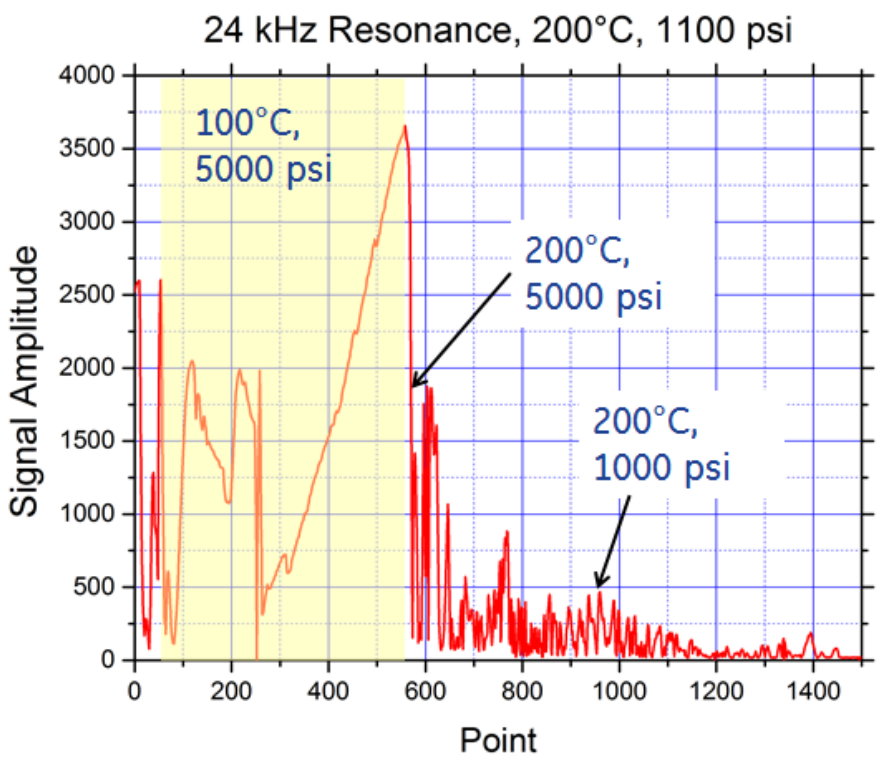

Fig. 105: Chart of signal amplitude over time (points are collected every 15 s) for high pressure run at 100°C during which a leak occurred in the sensor package at ~point 570. Signal did not recover after returning sensor to ambient temperature and pressure.

Prior to the leak developing in the sensor package, the short term stability of the sensor signal was measured with the sensor immersed in supercritical-CO_2 at 100°C and 1100 psi. The data are shown in Fig. 106.

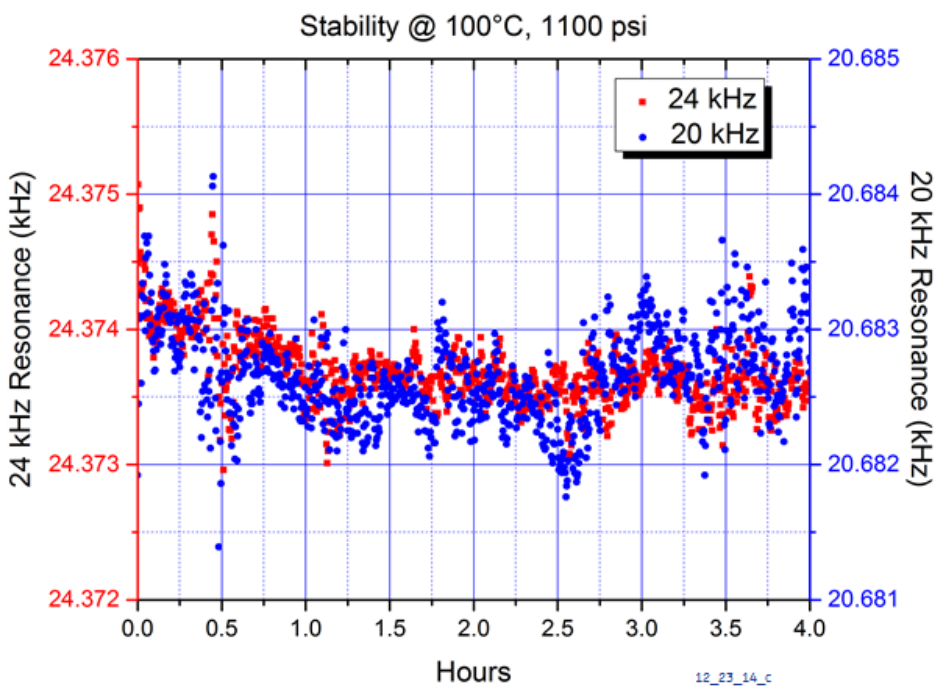

Fig. 106: Short term stability of sensor signals measured with the sensor in sc-CO_2. Variation in sensor frequency for both resonances is <2 Hz, corrsponsing to a pressure variation of <1 psi over this 4 hour measurement.

The sensor package was subsequently removed from the pressure vessel and examined. Silicone oil was found in the cavity below the sensor as shown in Fig. 107, indicating that oil had passed through the hypodermic tube.

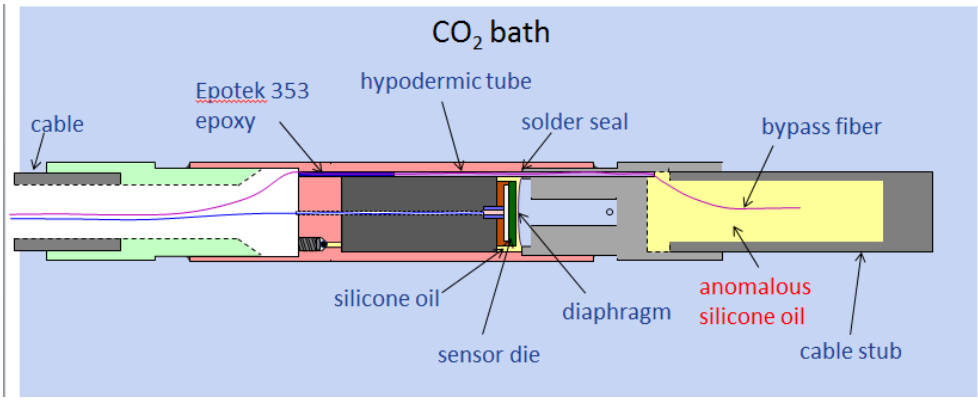

Fig. 107: Schematic of sensor package that was immersed in CO_2 bath at high temperature and pressure. The sensor die is surrounded by high temperature silicone oil to transduce the external pressure to the silicon die. However, after failure of the sensor, when the cable stub on the right side was cut open, the stub was discovered to be filled with silicone oil. Apparently, the hypodermic tube connection was not well sealed.

The variation of the resonant frequencies with temperature was determined from the data collected at 25°C and 50°C and is shown in Fig. 108.

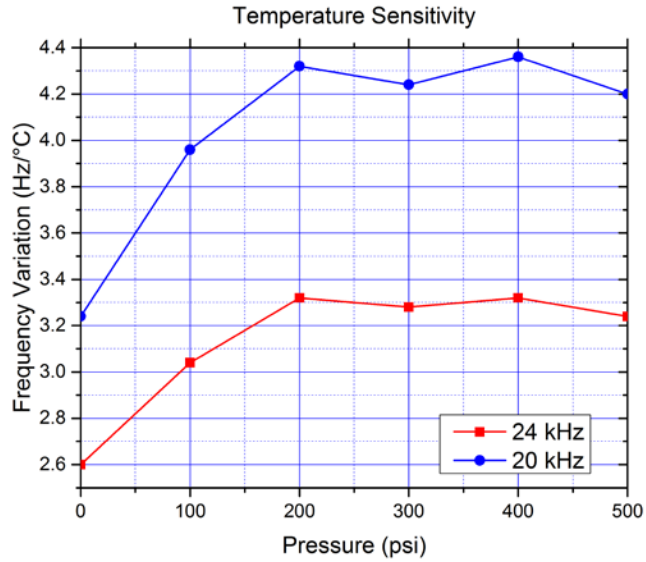

Fig. 108: Variation of resonant frequency with temperature at pressures between ambient and 500 psi.

The sensor package was designed with an Invar insert meant to precisely counteract the effect of thermal expansion of the silicone oil. In previous single-point pressure sensor packages without the Invar rod, as the temperature rose, the silicone oil expanded, thereby causing enormous pressure within the silicon sensor die cavity and causing the resonant frequency of the sensor to increase. This issue limited the dynamic temperature range of the sensor and required that the volume of oil in the sensor cavity be kept as small as possible. If the Invar rod were counteracting the oil expansion properly in this package test, then the resonant frequency of the sensor should have dropped at ~1 Hz/°C due to thermal expansion of the silicon die itself. Because a frequency *rise* was in fact measured, it is clear that the amount of oil in the cavity had to be more than had been calculated for the package design. This is also consistent with the supposition that oil leaked through the hypodermic tube into the cavity below the sensor.

B. Mechanical stress testing

The sensor package with the high Q sensor die was welded into the sheave tester as shown in Fig. 109 for the mechanical stress test.

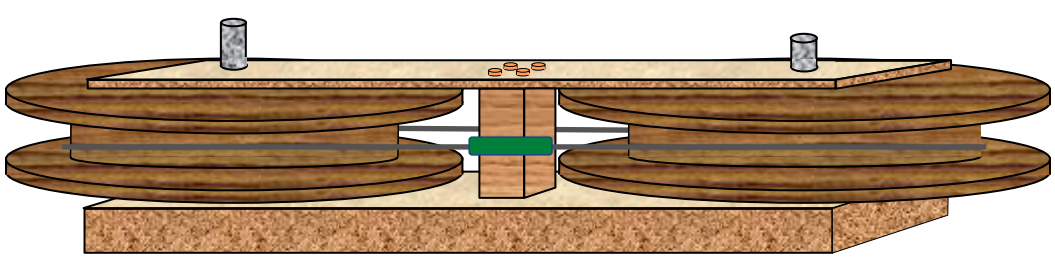

(a)

(b)

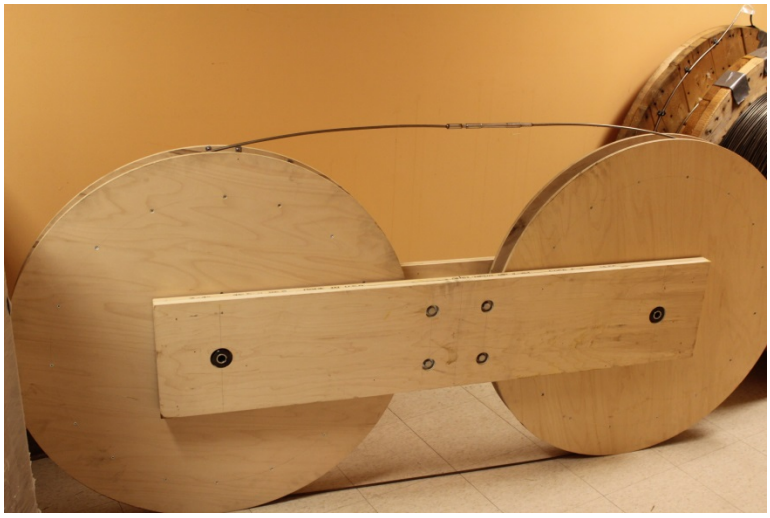

(c)

(d)

Fig. 109: (a) Drawing of original sheave tester design. (b) Completed sheave tester with ¼" stainless steel cable wrapped around both sheaves. (c) Sheave tester with sensor package spliced/welded into cable. (d) Close-up of sensor within cable.

During cable deployment, the cable rolls across two sheaves as shown in Fig. 110.

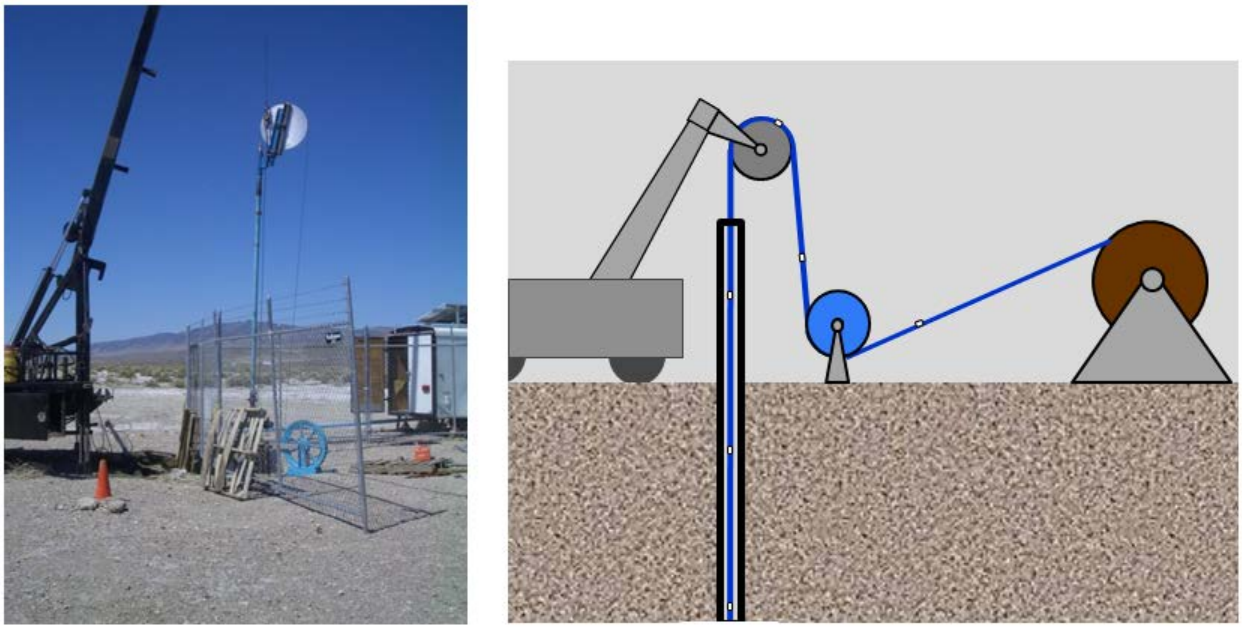

(a) (b)

Fig. 110: (a) Example of field deployment of sensor cable showing blue sheave with spokes on ground and aluminum sheave without spokes in the air and held by crane. ¼" stainless steel cable is barely visible going to upper sheave. (b) Schematic diagram of deployment process in which cable wraps ~90° around first sheave as it comes off the spool and then wraps ~180° around the upper sheave before entering the well.

The cable makes a ~90° bend around the first sheave and ~180° bend around the second sheave. To apply a mechanical stress test to the sensor package, therefore, it is necessary to ensure that the package can roll around a sheave for at least 180° without being bent and destroying the alignment of the fiber to the sensor die.

To apply the mechanical stress test to the sensor package, the sheave tester was simply rolled along the floor so that the sensor package passed around a sheave until it was visible coming up between the sheave and the center wooden block, thereby making a total rotation of >180° around the sheave. In Fig. 111(a) the sensor package is shown just entering the sheave during its first roll. Unfortunately, almost immediately the weld where the cable was attached to the sensor package cracked as shown in Fig. 111(b). In retrospect, this weld should have been better designed to protect this joint as the cable tube was undoubtedly weakened by the high temperature welding process. This weld, however, is unimportant for the essential purpose of this test to see whether the stress of deployment causes the sensor package itself to bend and destroy the connection between the fiber and sensor. Therefore, standard filament tape was wound around both welds where the cable entered the sensor package as shown in Fig. 111(c), and fortunately this was sufficient to hold the package to the cable for the remainder of the test.

(a)

(b)

(c)

(d)

(e)

(f)

Fig. 111: Process of rolling sensor package around sheave. (a) Sensor package as it approaches the first sheave. (b) Leading weld cracks immediately as package begins to rotate around sheave. (c) Welds at both ends of the package are "fortified" with filament tape. (d) Sensor package is again rolled around sheave. (e) Sensor package appears in space between sheave and inner connecting block indicating rotation of sensor by ~270° around the sheave. The sensor is then unrolled to its initial position in Fig. 16(c) and the complete rolling process was repeated five times. (f) After completion of the test, a support bracket was attached to the sensor package, brackets were used to attach the cable to the side of each sheave, and tubing cutters were then employed to remove the package from the cable.

With the filament tape around the outer two welds, the sheave tester was rolled along the floor until the sensor appeared in the space between the sheaves as shown in Fig. 111(e). Then the sheave tester was "unrolled" until the sensor was again at the top, in the space between the two sheaves. In this way, the sensor package experienced a complete "deployment" process of rolling around a sheave twice for a total rotation angle of ~270° each time, which should be at least comparable to the stresses experienced by a sensor package during a deployment process as shown in Fig. 110. This sheave tester rolling process was then repeated for a total of five times before the sensor package was removed from the cable as shown in Fig. 111(f). There was no obvious bending of the sensor package as a result of this test. It appears that the sheave diameters and the tension in the cable were chosen appropriately to enable the sensor package to roll over the sheave without damage, although it is also true that the cracked weld enabled most of the bending process to occur at the crack itself as is evident in Figs. 111(c) and (e).

After removing the sensor from the sheave tester, a new connector was spliced onto the fiber and the sensor was again measured on the pulsed laser interrogator. The sensor signals before and after the test are shown in Fig. 112. The signal amplitude after the test is slightly larger than that

before the test, but this is primarily due to a slightly different readout laser power used to obtain the best SNR (67 mA laser current before and 88 mA after) and perhaps a better connector splice. In any case, there is no significant drop in the SNR after the test, which is perhaps the most important result. There are small shifts in resonant frequencies, with the 17 and 41 kHz resonances shifting down in frequency and the two 22 kHz resonances shifting up in frequency. The frequency shifts are likely due to small temperature changes in the sensor die due to variation in laboratory ambient temperatures or due to the different laser powers. Because of the manner in which the sensor die is attached to the sensor package only at one point, via a ferrule epoxied to the die, it is unlikely that any bending of the outer package would be able to induce stain into the sensor die to shift the resonant frequencies, but this is an aspect that should be investigated further.

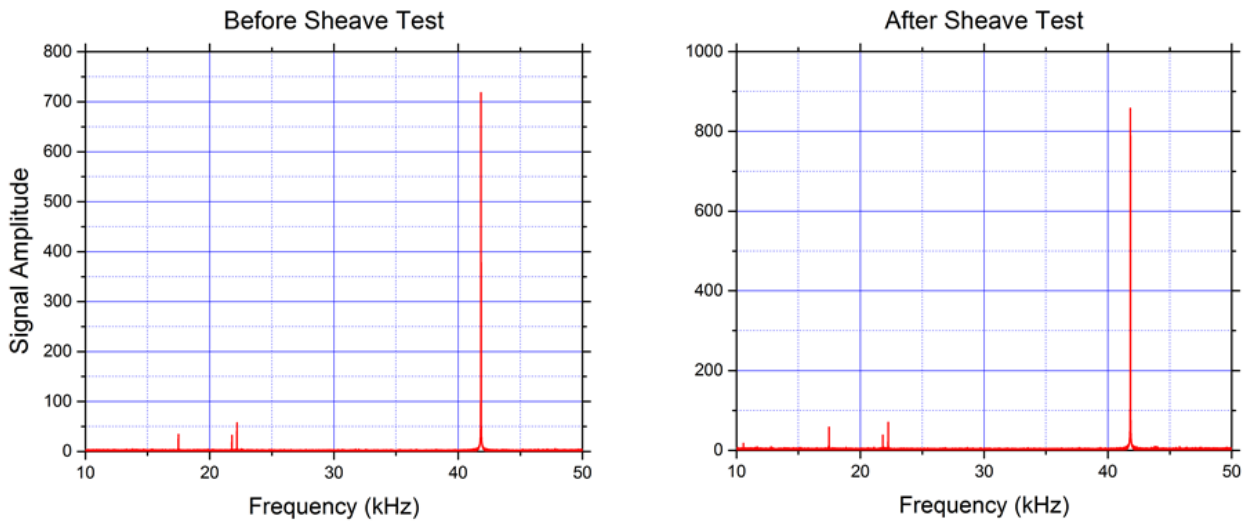

(a)

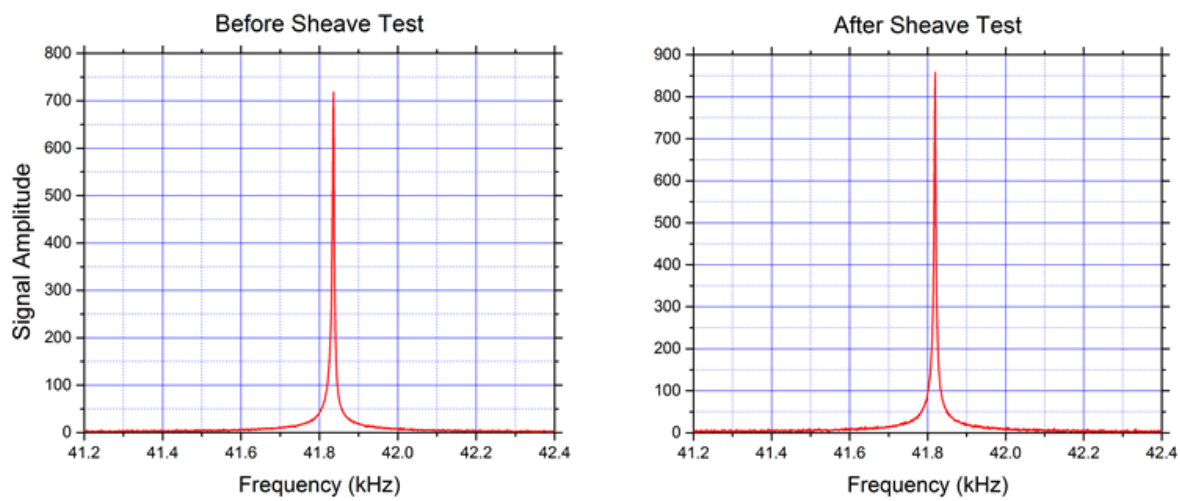

(b)

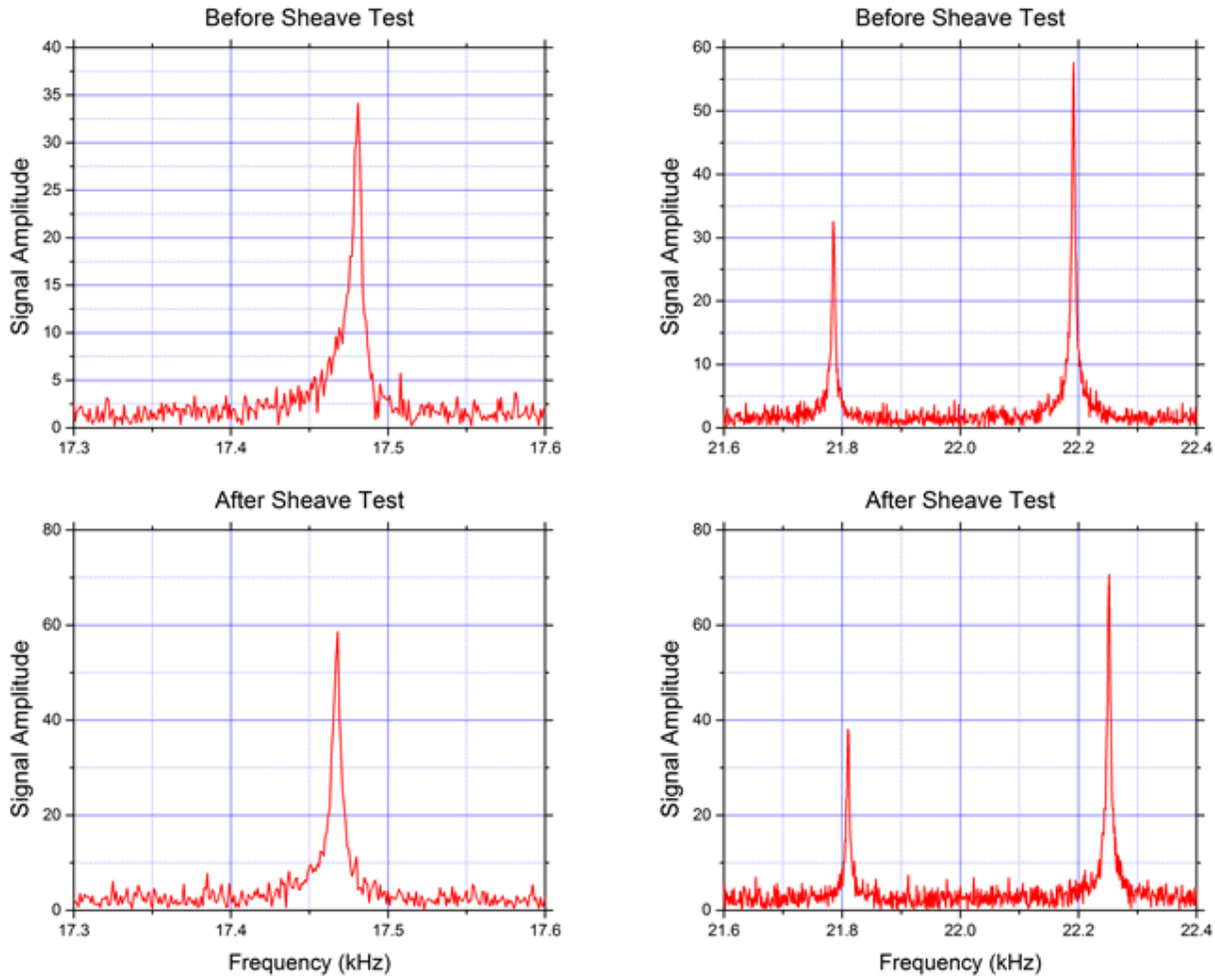

(c) (d)

Fig. 112: Resonant frequencies and amplitudes for high Q sensor signal before and after rolling the sensor package on the sheave tester. Frequencies before: 17.481, 21.785, 22.192, and 41.836 kHz. Frequencies after: 17.468, 21.810, 22.252, and 41.819 kHz.

Because of the cracked weld between the cable and sensor package as previously described and shown in Fig. 111(b), when the sensor was rolled on the sheave tester even with the filament tape holding the cable to the sensor, it is clear that the entire torque of the bending cable did not get applied to the sensor package. Therefore, a second test was devised. As shown in Fig. 113, the broken cable section was removed from the sensor and the end of the sensor was clamped in a vise. A longer piece of ¼" steel cable was attached to the short remaining piece coming out of the sensor using filament tape. This longer piece of cable was then bent into a circular arc by applying force to its outside end. The minimum radius of curvature was measured to be 12". This is much smaller than the 18" radius of curvature of the sheave. For small amounts of torque, the strain in the cable is inversely proportional to the radius of curvature. The torque

applied to the cable is, therefore, much larger for the smaller bending radius than it would experience when rolling over a sheave.

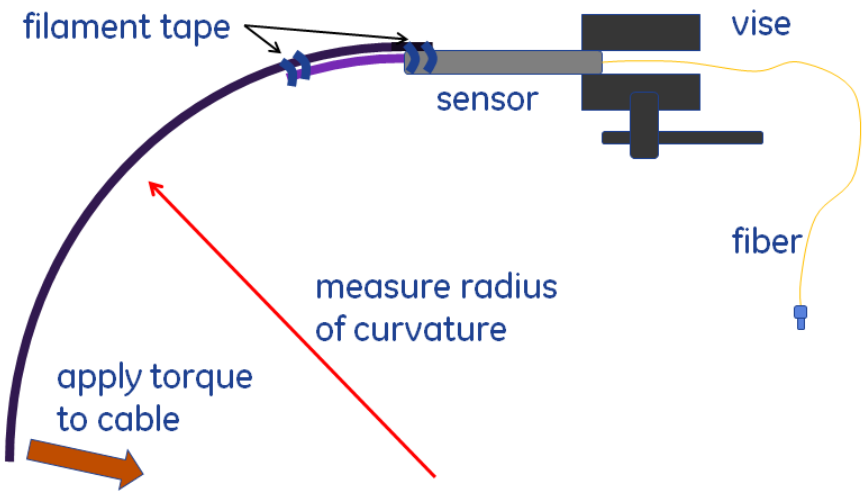

Fig. 113: Second torque test of sensor package. End of sensor with fiber coming out was clamped in a vise. End of sensor with cable coming out was attached with filament tape to a longer (~6′) section of ¼″ cable. The end of the longer cable was then pulled to bend the cable to a tight radius, which was measured to be 12″.

After applying torque to the sensor package as shown in Fig. 113, the sensor response was remeasured. The results are shown in Fig. 114.

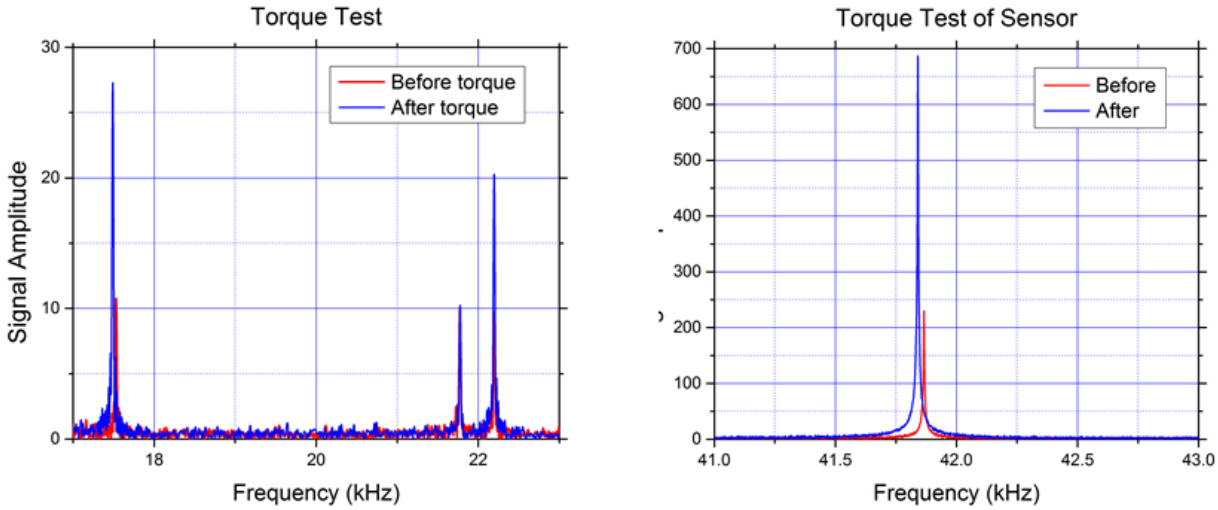

Fig. 114: Resonance signal amplitudes before and after the torque test. The signal amplitude actually increased after applying torque. Resonant frequencies at 17 and 42 kHz decreased slightly, while the resonant frequencies at 22 kHz were unchanged.

Clearly the application of torque to the sensor package appears to have a small effect on the resonant frequencies of the sensors. It is not clear if this effect is due to some strain in bending the package being transferred to the sensor die mount, or if this effect is simply a result of small changes in sensor temperature due to slightly different laser powers used to obtain the best SNR for the measurements.

In any case, the failure of the weld where the cable entered the sensor package was unfortunate. We believe that this joint could be substantially improved by inserting a steel coupler in the tube at this weld.

C. Environmental testing:

Due to the delays in assembling a complete sensor package for environmental testing, an alternate approach was devised for determining the environmental stability of the sensor package. The entire outer surface of the package that is exposed to the environment is made from Inconel 625, which was the material of choice for the single point pressure sensor in an earlier project. 1 mil thick membranes of Inconel 625 were purchased from Goodfellow for use inside the sensors, but it was realized that these would be nearly ideal parts for environmental testing as well due to their very high surface to volume ratio. Eight membranes were chosen for testing and very small holes drilled in the center of each membrane. Their masses were then measured. The average mass was ~10.5 mg. The membranes were inserted into pressure vessels after being placed on ceramic spacers as shown in Fig. 115. This ensured that there was no contact between the membranes and the metallic pressure vessel (which was also composed of Inconel 625, so there should have been no electrochemical processes involved in any case).

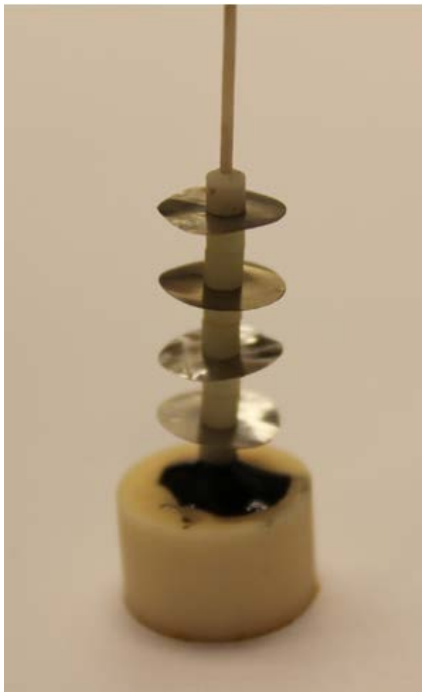

Fig. 115: Inconel membranes that are 8 mm in diameter and 25 mm in thickness with a 1 mm hole in the center are stacked on a ceramic alumina rod with alumina spacers as shown prior to placement inside the high temperature / high pressure vessel for exposure to CO_2. High temperature epoxy (black) was used to secure the alumina rod to the ceramic base.

Several tests were then performed on the membranes. Initially, two membranes were placed in supercritical CO_2 at 250°C and 10 kpsi, and two other membranes were placed in a saturated saline solution at 250°C and 580 psi (from the water vapor pressure) for 190 hours. For the two membranes in the sc-CO_2, the mass change was +42 μg ± 60 μg, and for the membranes in the saline solution, the mass change was +50 μg ± 75 μg. In other words, to within the measurement error, no change was observed in the membrane masses in either environment. The two membranes in the sc-CO_2 were then reinserted into the 250°C, 10 kpsi pressure vessel along with two new membranes and soaked for an additional 1100 hours. The average mass change for the four membranes was then measured to be 33 μg ± 47 μg. Again, there was no apparent mass change within the measurement error. The membranes emerged from the sc-CO_2 bath with a basically shiny appearance and little sign of corrosion as shown in Fig. 116.

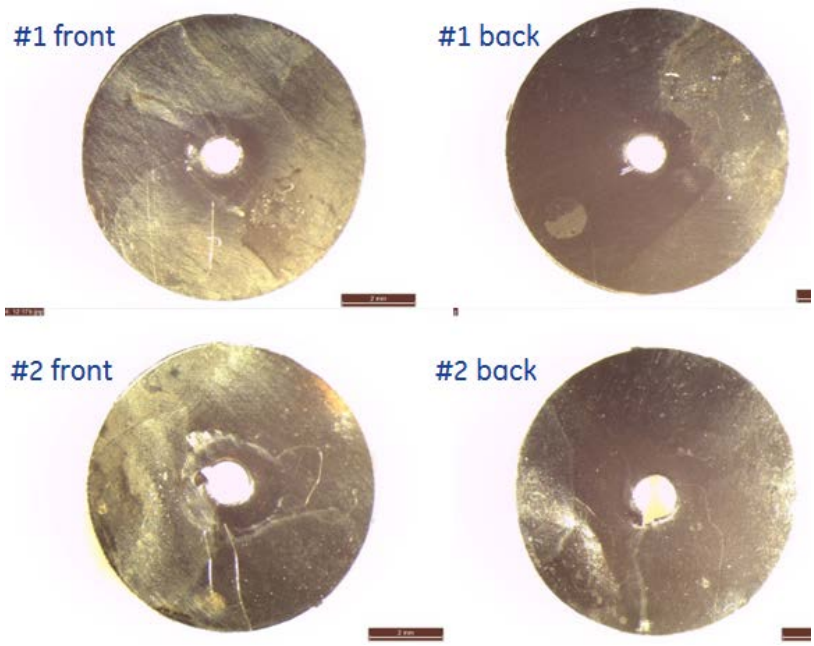

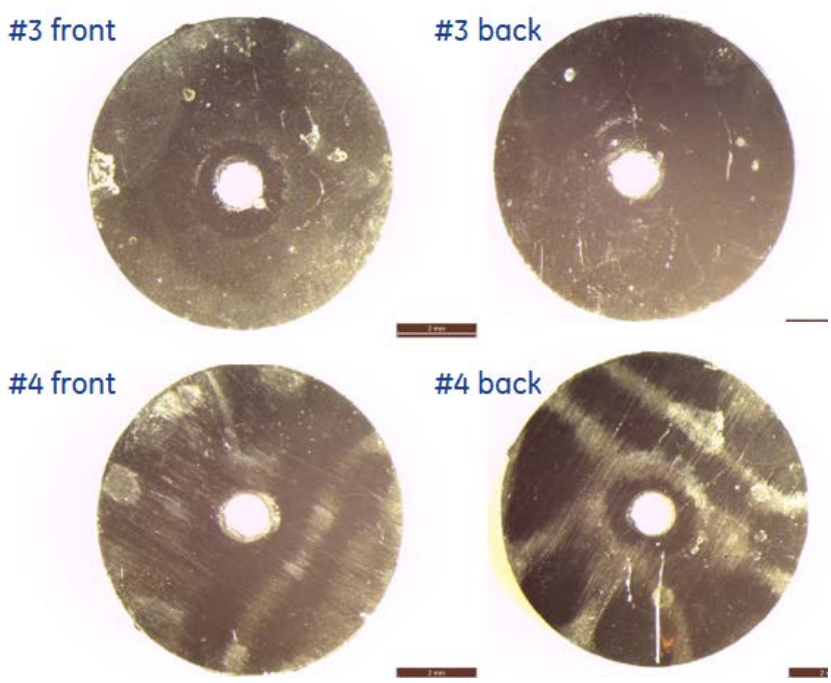

Fig. 116: Inconel membranes exposed for 1100+ hours to sc-CO_2 at 10 kpsi and 250°C.

Finally, the two membranes that had previously been placed in saturated saline at 250° and 580 psi were again tested along with two new membranes in another saturated saline solution which in this test was pressurized to 10 kpsi with sc-CO_2. These membranes were exposed for 220 hours before inspection. The measured change in mass was -50 μg ± 83 μg. Again, within measurement error there was no change in mass. However, when the membranes were examined after the exposure, they had a clear patina from superficial corrosion as shown in Fig. 117.

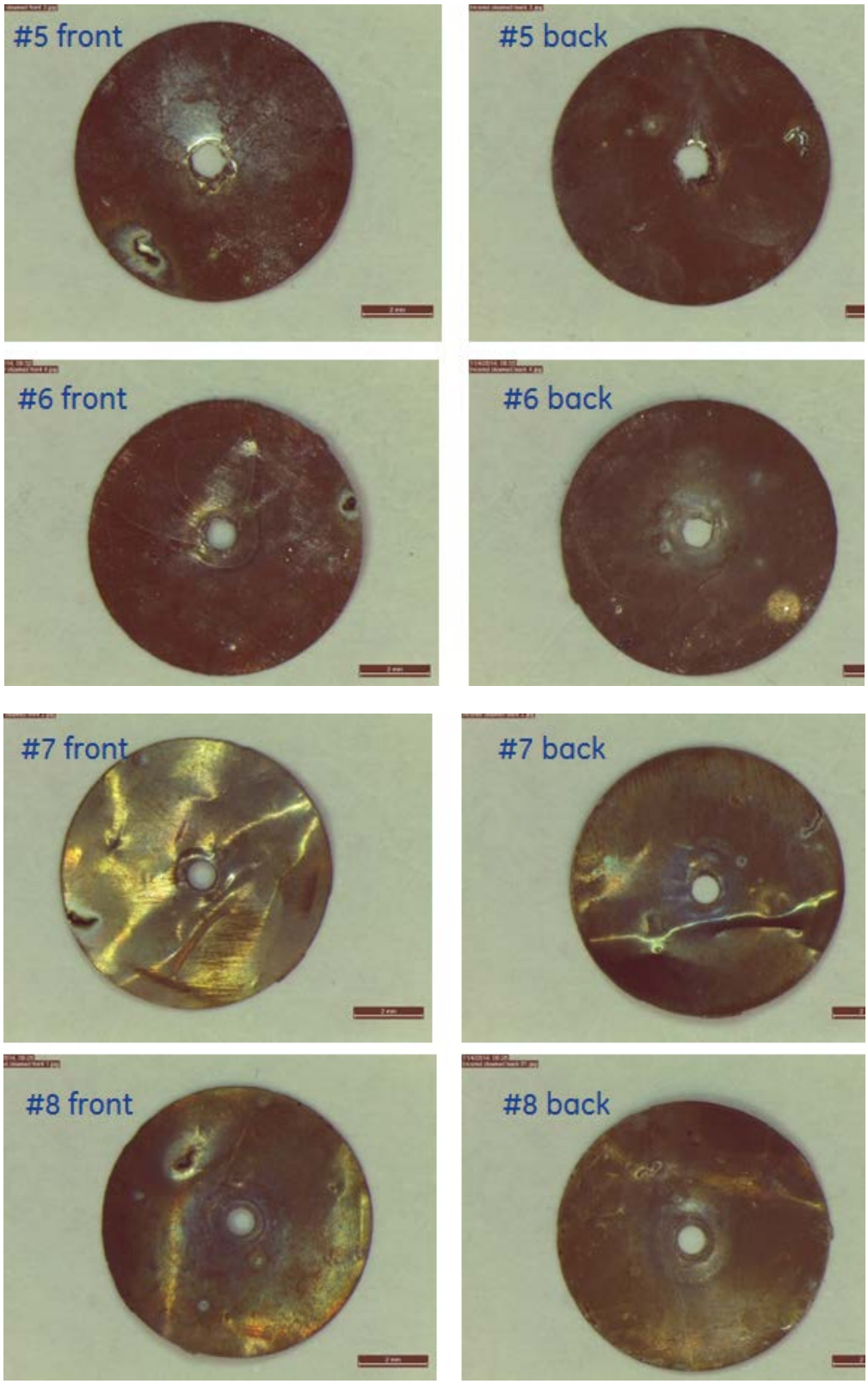

Fig. 117: Inconel membranes exposed for 200+ hours to sc-CO_2 and saturated saline at 10 kpsi and 250°C.

The saturated saline solutions in these tests were made with NaCl at 30 wt. % at room temperature. However, actual downhole brine compositions vary enormously. It is clear that the specific environment for the sensor could in fact be extremely important for the long term accuracy and survivability of the sensor. The test summary is shown in Table 8.

Table 8: Summary of Inconel membrane testing

Test	Temperature	Pressure	Time	Mass change
sat. saline	250°C	580 psi	190 hours	+50 *m*g ± 75 *m*g
sat. saline + CO_2	250°C	10 kpsi	220 hours	-50 *m*g ± 83 *m*g
sc-CO_2	250°C	10 kpsi	1100 hours	+33 *m*g ± 47 *m*g

Task 5: Activate Wireless Remote and Operate Sensors

Task Completion Date: 09/30/2014
% Complete: 100%

A CO_2 sequestration remote monitoring and readout system has been designed, developed, and tested to monitor and control different parameters from the remote location of the well sites. Fig. 118 shows the overview of the system developed by GE Research. The sensor is operated and monitored by a conventional optical interrogator connected to a PC using custom LabView software. The PC communicates to remote stations via a cellular wireless backhaul modem. Between the remote station and the PC is a cloud-based service that automatically collects data from the interrogator PC, stores and analyzes the data, and transfers the data as needed to any internet-enabled remote station with the proper monitoring software.

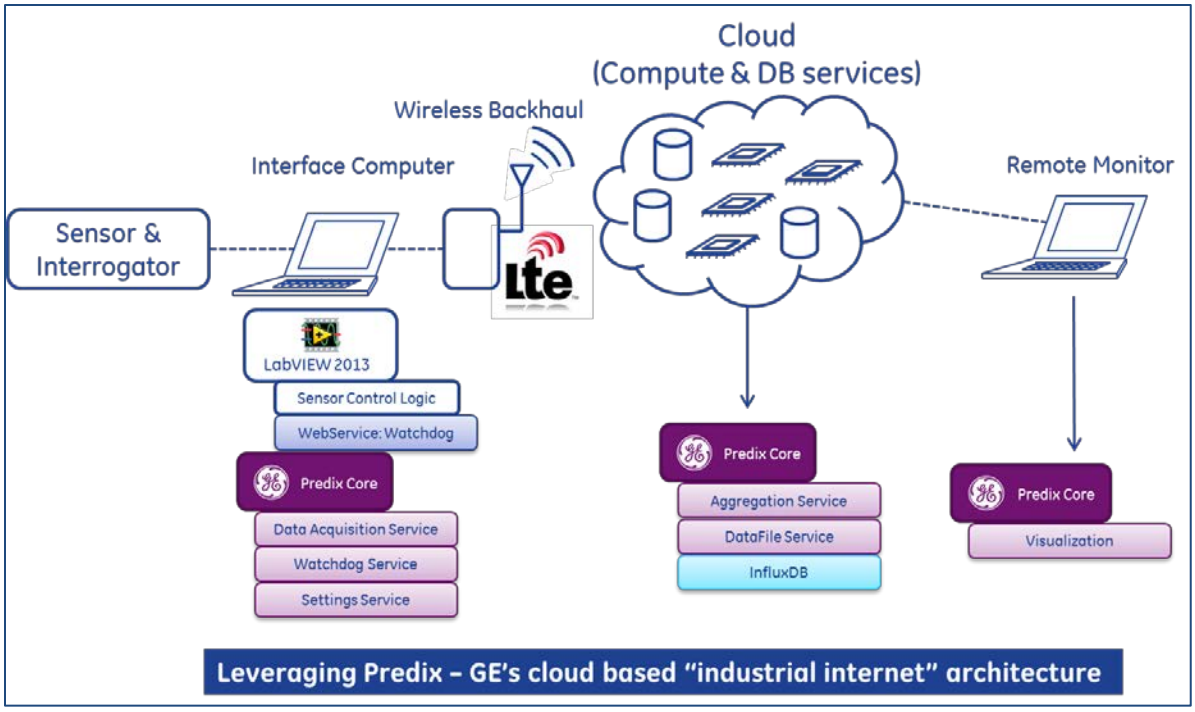

Fig. 118: Readout system overview with service module and deployment locations.

1 INTERROGATOR

A conventional optical interrogator system was developed for the remote communication demonstration as shown in Fig. 119.

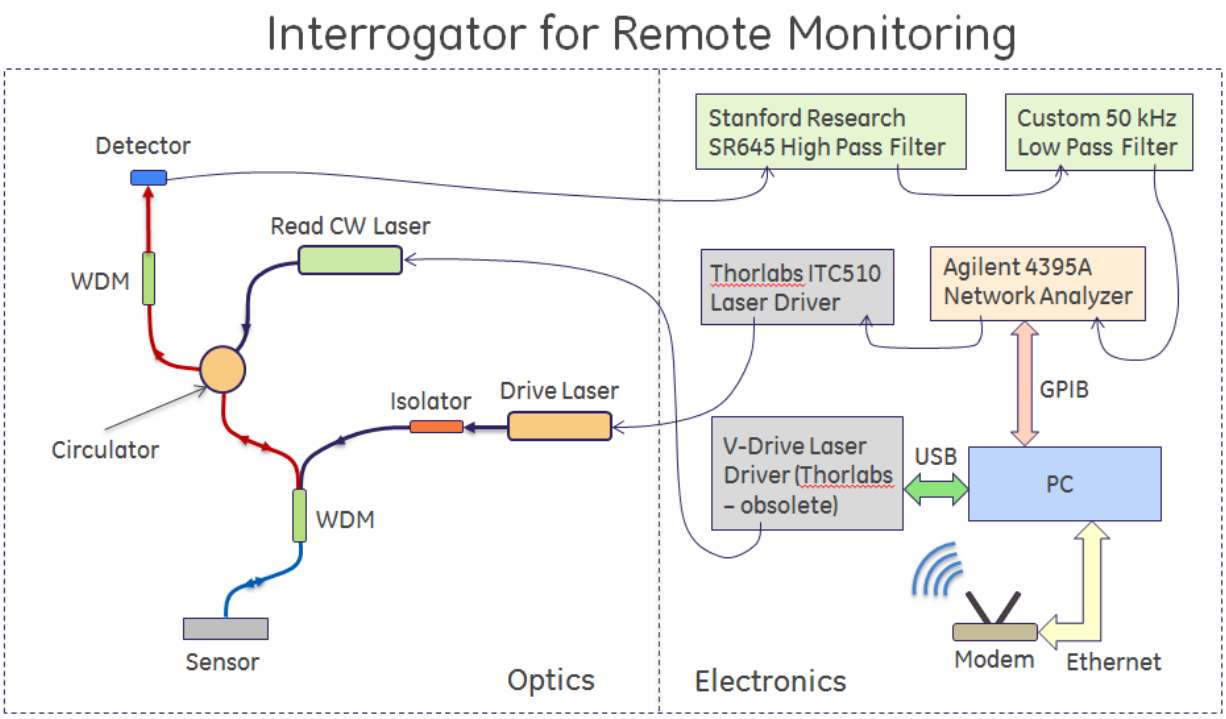

Fig. 119: Diagram of optical interrogator for remote monitoring demonstration. The optical subsystem diagram is shown on the left, and the electronics on the right.

The interrogator is operated by a local PC via a user interface written in LabView™. The drive laser is sinusoidally modulated at the reference frequency output from the network analyzer. As the network analyzer scans across the frequency band of the sensor, the amplitude of the membrane vibration inside the sensor varies, reaching a peak amplitude at its resonant frequency. The membrane forms one side of an optical cavity with the outer package of the sensor die, so the vibrating membrane in turn modulates the amplitude of the CW read laser. The light reflected by the sensor from the read laser is split off via a circulator to a separate detector and the signal amplitude at the reference frequency of the network analyzer is measured as the frequency is scanned. Both the amplitude and frequency of the resonance can thereby be determined.

The LabView program captures the scans from the network analyzer over the GPIB bus and uses a standard quadratic curve fitting routine to determine the peak position and amplitude for each scan. The data are displayed on the screen of the local PC and stored periodically into a file on the local hard drive of the PC. The PC is also connected via USB bus to a thermocouple to monitor the local temperature of the sensor as a function of time.

As the data are collected, they are formatted into an XML file and stored in a specific location on the hard drive. In greater detail, the entire operation is carried out in the following manner (Fig. 120). First, the local PC communicates with the HP network analyzer and reads the spectral waveform from its memory buffer (multiple scans can be averaged as desired by the user for

enhanced signal-to-noise ratio). An example of a waveform that exhibits two separate sensor resonances is shown in the top graph of the upper right screen shot in Fig. 120.

The resulting waveform is then scanned for resonances by an algorithm that uses Labview's *Peak_detect* VI that fits a quadratic curve to a user-selected number of points around each detected peak. Each detected resonance is characterized by its amplitude, frequency, and peak width (FWHM). Both the raw waveform and the detected peak characteristics (as functions of time) are then displayed graphically on the local PC monitor. For example, the lower graph in the upper right screenshot is a real-time chart of the peak amplitude. The LabView program also records ambient temperature by communicating with a USB thermocouple probe. A LabView software flowchart is shown in the upper left image of Fig. 120.

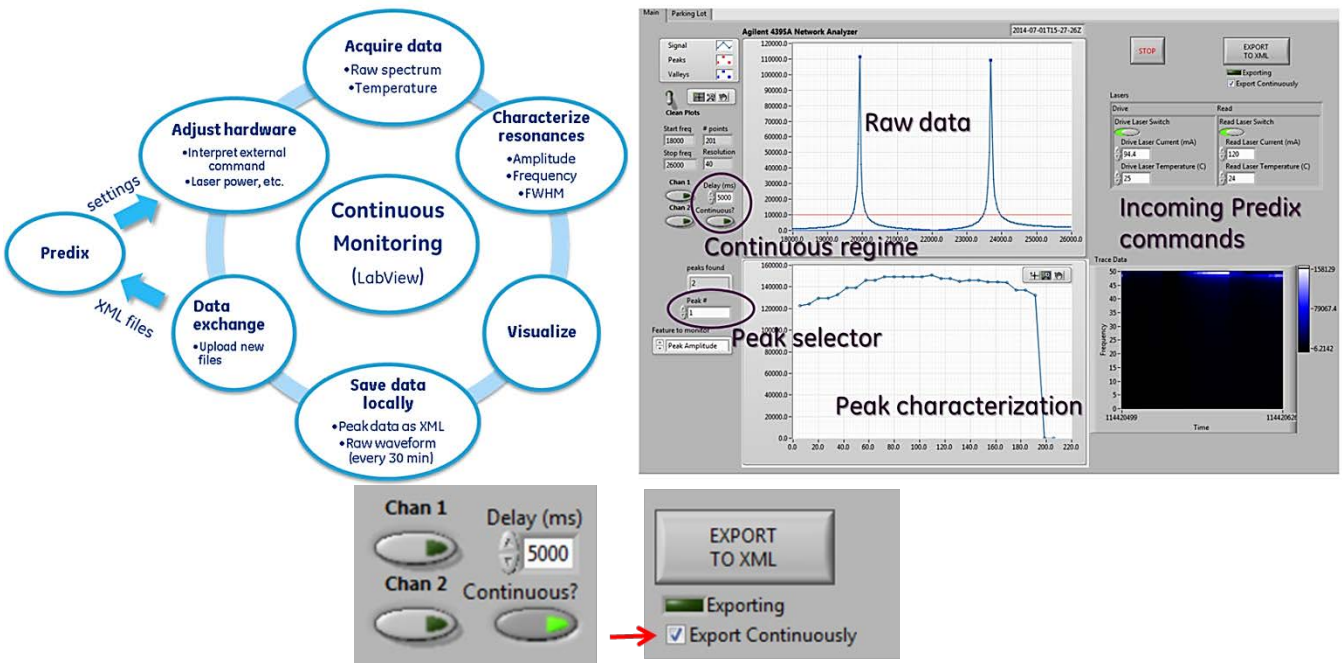

Fig. 120: Left top: Flow diagram for communication between the local machine and GE's internet software system, Predix. Right top: Software interface on LabView for a local machine. Bottom: software detail showing relevant knobs for continuous operation. In this example, the operation cycle is repeated every 5 seconds with enabled continuous exporting of the acquired data.

The peak characteristics are also stored on the local drive in *C:\CO2data* as an XML file. Effort was made to ensure that the structure and format of the XML file were optimized for seamless read-out by Predix, and the file is named by its current timestamp. Depending on number of peaks found in the waveform (2-10 usually) the length of XML array can be 2 to 10 elements, i.e., it has a variable length which can change even during the course of data acquisition. In addition to the peak data, the raw waveform containing the resonances is also stored at reduced

time intervals (e.g., every 10 points) with a filename format as *C:\CO2data*timestamp*-FULL.xml*.

Following the file storing step, Predix reads the stored data at specified time intervals. In addition to transferring the stored data to the cloud, Predix is also able to convey commands from a remote user to the local interrogator. The local LabView software is also designed to read, interpret and carry out these commands from the remote monitoring dashboard. The basic functionality includes triggering knobs externally, changing the value of a numeric control, and interpreting a custom command. An example with the "*restart_hardware*" command is shown in Fig. 121. The data exchange is accomplished using the XML schema and format discussed above. As previously stated, the command interpretation and consequent hardware control / adjustment of equipment settings are carried out by the local machine.

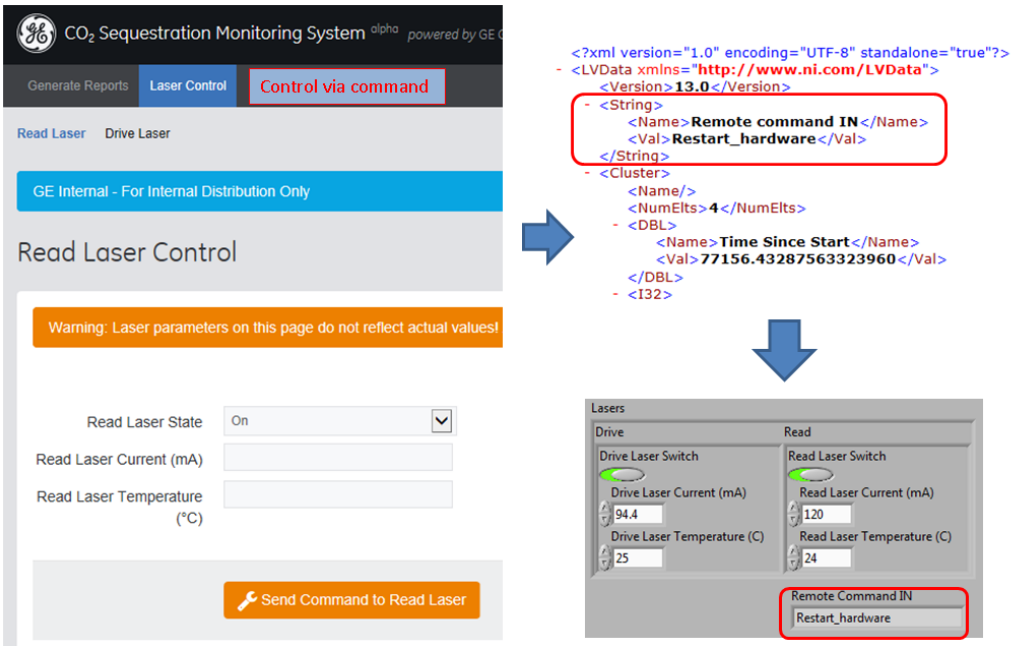

Fig. 121: Transfer of external command to XML file which is saved on local machine by Predix. Labview continuously monitors that file for changes and extracts incoming commands. The commands are then interpreted and hardware settings are adjusted accordingly.

Following the LabView-Predix data exchange, the cycle continues every N seconds, where N is the delay setting shown in Fig. 120. Long-term sensor monitoring can then be done entirely remotely, including rebooting the system if necessary.

2 PREDIX Software Modules

The individual Predix modules in the readout system are discussed below, as well as on which machines the components are typically deployed.

2.1 Sensor Monitoring Service (SMS)

Collecting reports is handled by the Sensor Monitoring Service (SMS) module within the readout system. The SMS will (i.) periodically search for files in a specified location, (ii.) perform basic validation on the reports, (iii.) archive files which have been successfully validated in a predefined location, and (iv.) publish the report data for aggregation. In the typical deployment scenario (Fig. 122) the monitor machine performs the task of collecting reports at periodic intervals. The monitor machine is also usually the machine used to run a particular experiment and generate the reports from an experiment.

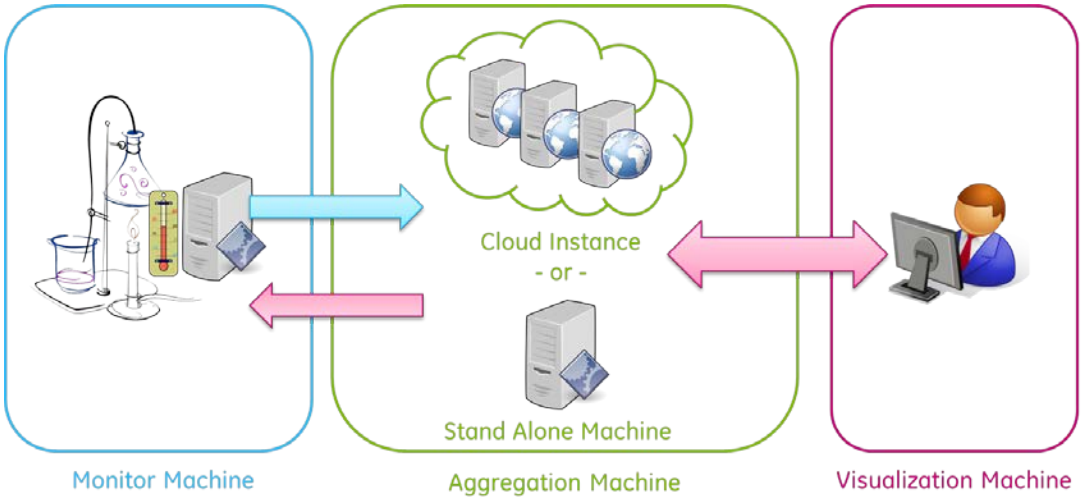

Fig. 122: The typical manner in which the readout system is deployed.

2.2 Remote Monitoring Service (RMS)

Consuming reports, converting data points within reports into a time-series format, and interacting with the database are handled by the Remote Monitoring Service (RMS) module within the readout system. The RMS reads reports produced by the SMS and simplifies the data points in the reports into their most basic form. Once the data points have been simplified, the data points are converted into a time-series and stored in a time-series database. The time-series database is usually hosted within the aggregation machine for convenience, but can be hosted on another machine if desired.

In addition to data aggregation and storage, the RMS is also used to query the time-series database. Querying the time-series database can be done by hosting a webserver on the aggregation machine that serves a visualization web app such as Grafana, or by serving a static webpage that allows users to access the RESTful report generation service in Predix. The RESTful report generation service is provided via the RMS module in the readout system, while visualization tools are standalone web apps that directly query the database.

2.3 Sensor Control Service (SCS)

The Sensor Control Service (SCS) provides a simple method for pushing commands or new values to a remote sensor. The SCS needs to run on the monitor machine or the machine to be controlled. The SCS accepts commands to set values, and will write values to the monitor machine.

2.4 Visualization Machine

The last machine depicted in the typical deployment scenario (Fig. 122) is the visualization machine. It is important to note that the visualization machine does not require any software to be installed, other than a web browser. The visualization machine is included to depict how a researcher or other operator would interact with the RMS and SCS services. Typically researchers will use a web browser to access web pages and the dashboard that allow one to generate a report, view real-time time-series data captured during an experiment, or send commands to a particular sensor. All of the web pages which are accessed on the visualization machine are hosted on the aggregation machine.

3 Monitoring and control dashboard

All of the monitoring and control dashboards are designed using web applications so that the user can access the data and control the instrument from any location where an internet connection is available. The monitoring dashboard displays data collected from the interrogator as shown in Fig. 123. This dashboard may be flexibly organized according to user preferences. Currently the dashboard shows peak frequencies and amplitudes, read laser current and temperature, and ambient temperature. It is also very easy to add new data points if it becomes necessary.

Fig. 123: Monitoring dashboard.

All of the data are stored in the cloud. Using the report generation console, which is shown in Fig. 124, the user can download raw data for post-processing. Currently, the data can be downloaded either in Excel format or in XML format.

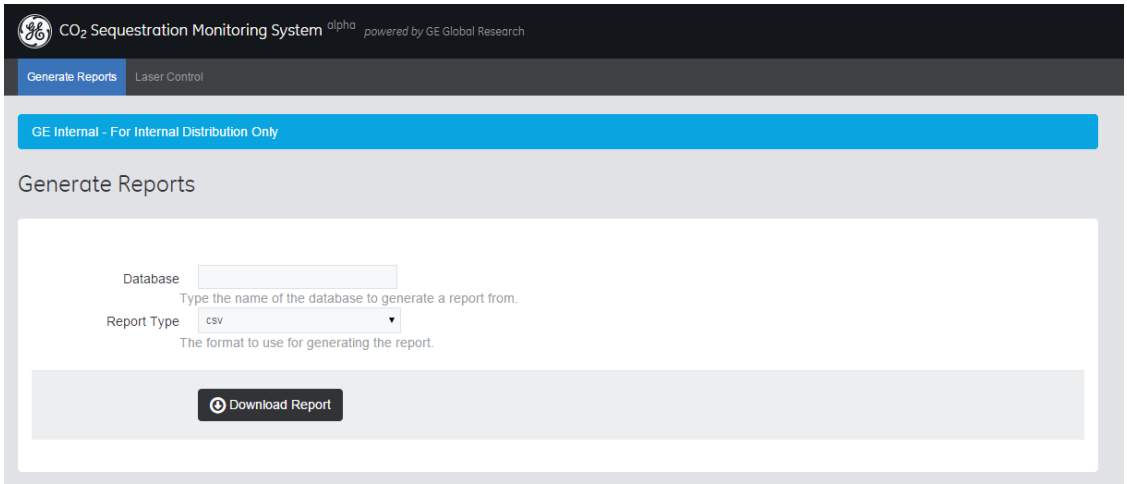

Fig. 124: Report generation console.

The data from the interrogator can not only be monitored, but it is also possible to control different parameters remotely using the cloud-based control application dashboard which is shown in Fig. 125. Currently we can control the state, current, and temperature of the read laser and drive laser. We also have an option to send a custom control command using the "other command" field in the web application.

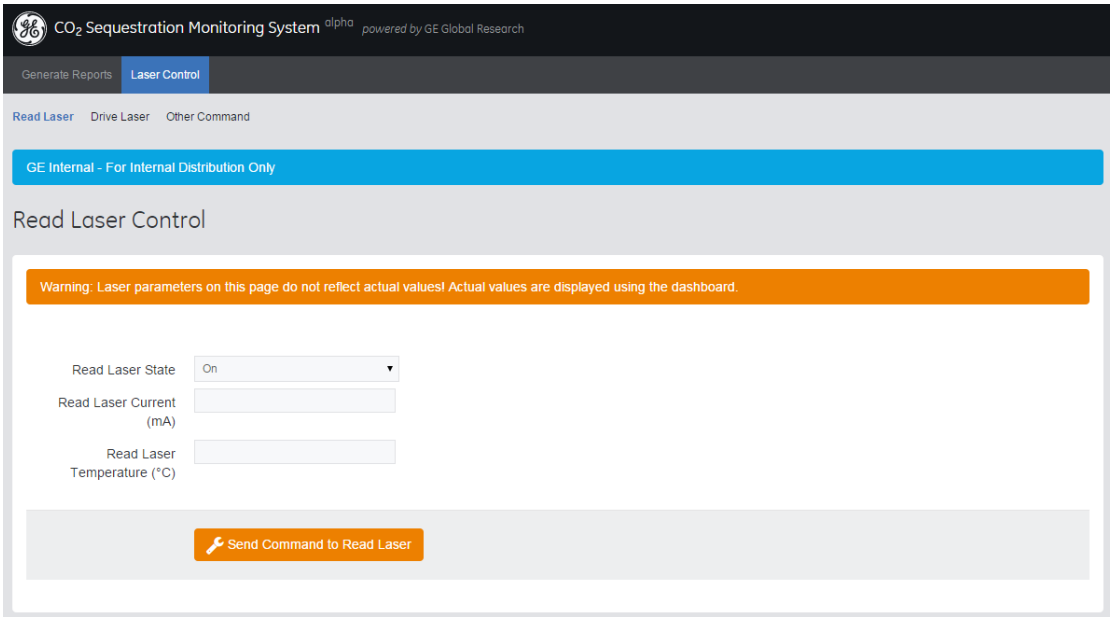

Fig. 125: Control dashboard.

4 RESULTS OF LABORATORY DEMONSTRATION

After completing the construction of the interrogator and debugging the LabView operating software and Predix control/visualization system using the internal (wired) GE network, a special request was made to the GE Information Technology group at GE Global Research to allow a wireless demonstration of the system. This entailed disconnecting the lab PC from the wired network and connecting it instead to a cellular modem that makes use of wireless service provided by the Verizon cellular network. Through this cellular service, the laboratory PC was then connected to the Amazon cloud service (AWS), also outside of the GE firewall. The Predix system as previously described was also installed on AWS and for a limited period of time (several hours on August 15th, 2014) data collected by the interrogator were automatically transferred to the Amazon cloud. This data is still stored on the cloud and can be accessed remotely by any web-connected PC with the appropriate Predix and utility software installed on it. Fig. 126 displays the data collected during this time as wirelessly downloaded on October 29th, 2014 to the office laptop of the PI.

Although it was necessary to operate outside of the GE firewall in order to make this wireless remote demonstration of the system, in an actual commercialization of this system, the sensors/interrogator would be connected to a cloud network using advanced encryption

technology which was not implemented in this demo. With such data encryption it then would become possible to operate these sensors on any outside cloud and connect to the cloud through the GE firewall without special IT permission. This is indeed how GE's industrial internet is being designed, so one purpose of this demonstration was in fact to begin the process of incorporating these sensors into the GE "internet of things."[35,367]

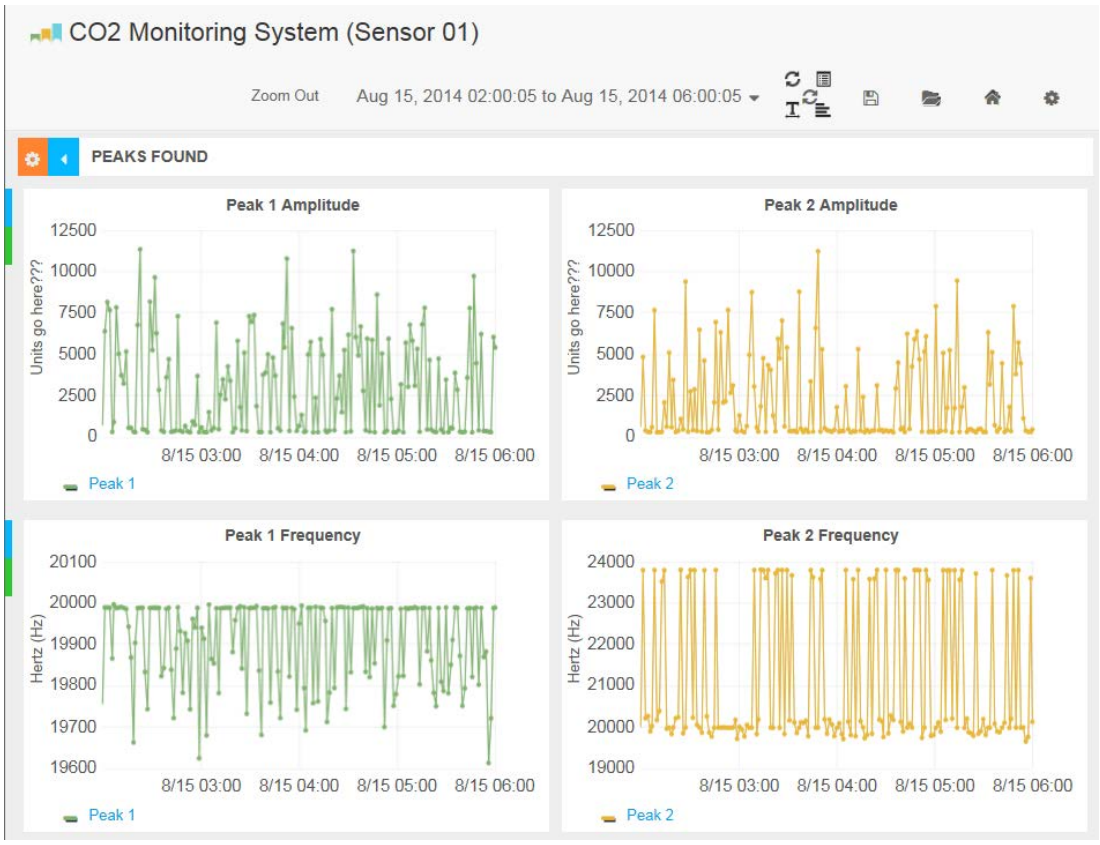

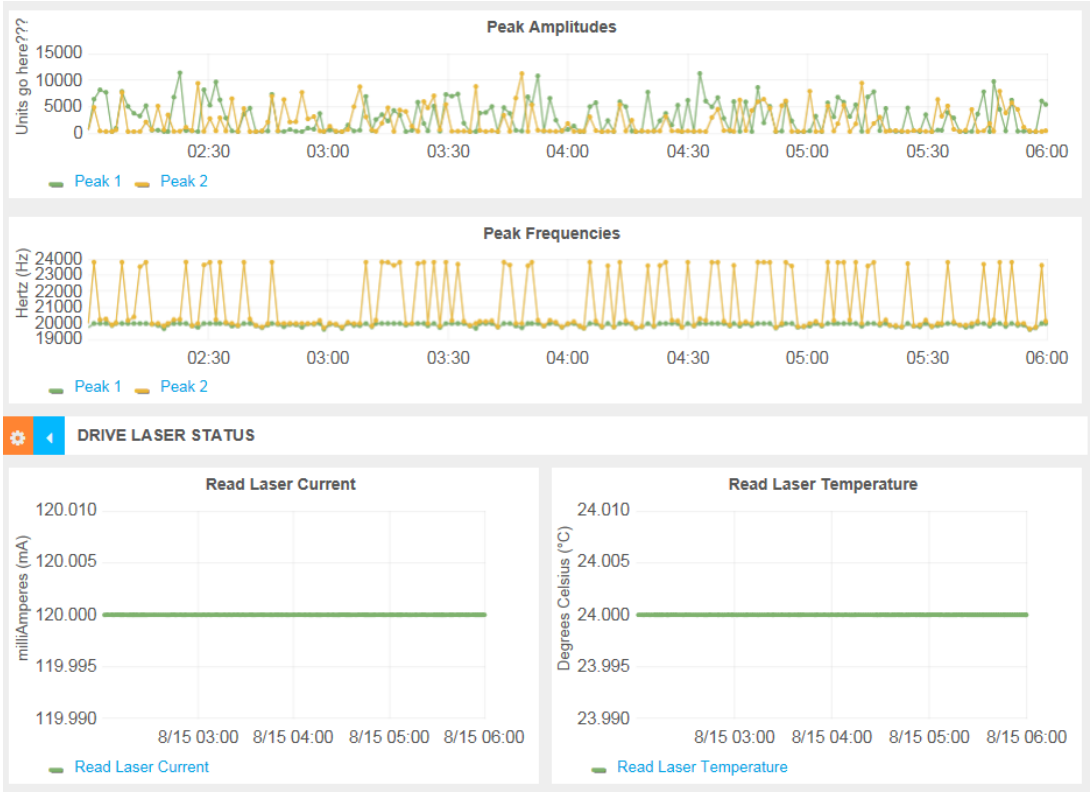

Fig. 126: Output from dashboard for data collected through wireless network via the Amazon Web Services during remote monitoring demonstration on August 15, 2014.

5 Installing the Readout System and its dependencies

The Readout System is a distributed application that is built on top of the GE Predix Core platform, and uses third-party applications for visualizing data. The applications that need to be installed to use the readout system are detailed in Table 9.

Table 9: Required Software

Software	Download Location
SMS, RMS, SCS modules (Monitor and Aggregation Machines)	
Java 7 Server JRE	http://www.oracle.com/technetwork/java/javase/downloads/index.html
Python 2.x	https://www.python.org/
Predix Core Kernel 14.2	http://predix.sw.ge.com/downloads
InfluxDB	http://influxdb.com/
Readout System Package	https://openge.ge.com/gf/project/readout-system/frs/?action=FrsReleaseBrowse&frs_package_id=3779
Data Visualization and Web Hosting (Aggregation Machine)	
Any HTTP server	
Grafana	http://grafana.org/
Elastic Search (Optional, used by Grafana)	http://www.elasticsearch.org/
Static Webpages for Accessing the RMS and SCS	To Be Released on OpenGE
Industrial Internet Design Extension (IIDx) development toolkit	https://www.gesdh.com/industrial-internet

6 Configuring the readout system

The readout system is a system composed of many different modules, and many of the modules require configuration before the readout system will serve as a remote monitoring and control platform. In general, the dependencies must be configured prior to running them. In many cases the dependencies are setup once, and their settings will not change while the readout system is running. The readout system has two methods used for configuration: (i) Dependency Injection, also known as Inversion of Control (IoC), via Spring, Camel, and OSGi context files, and (ii) Config files which are read when any given readout system module is started. The visualization tools have configuration files that need to be configured before using the tool, but can be updated at runtime since the visualization tools are all web pages (hence can be 'refreshed' in a web browser to apply the latest settings).

Predix Core 14.2 kernel

The main item to configure in Predix is the embedded ActiveMQ server and Predix's ActiveMQ client. The readout system relies on ActiveMQ and the Java Message Service (JMS) to properly route messages from the SMS to the RMS. Complete documentation about ActiveMQ, including all the transport protocols supported is online: http://activemq.apache.org/

7 Developer Installation Instructions

The full Predix installation guide can be obtained from the downloads section of the Predix website. The following third party software packages are distributed with the readout system release files.

Software Name	Link	License
Guava: Google Core Libraries for Java 1.6+ (17.0)	https://code.google.com/p/guava-libraries/	Apache License 2.0
Java Native Access (4.1.0)	https://github.com/twall/jna	Apache License 2.0
OkIo (1.0.0)	https://github.com/square/okio	Apache License 2.0
OkHttp (2.0.0)	https://square.github.io/okhttp	Apache License 2.0
Retrofit (1.6.0)	https://square.github.io/retrofit/	Apache License 2.0
Google GSON (2.2.4)	https://code.google.com/p/google-gson/	Apache License 2.0
InfluxDB Java Client (1.2)	https://github.com/influxdb/influxdb-java	MIT License
openCSV (2.3)	http://opencsv.sourceforge.net	Apache License 2.0
Zip4j (1.3.2)	http://www.lingala.net/zip4j	Apache License 2.0

8 Predix OVERVIEW

The GE Predix cloud infrastructure is employed to enable the cloud-based data collection and control, which provides the ability to monitor and control measurement systems from anywhere at any time.[37,38] The PC running the LabView program is connected to the cellular communication network to enable data communication to and from a remote location. The system can also use any other communication system such as satellite communication if necessary, but due to the cost and data requirements cellular communication was chosen to demonstrate the developed readout system. The GE Predix cloud infrastructure is employed to enable the cloud-based data collection and control, which provides the ability to monitor and control measurement systems from anywhere at any time.[39,40]

Research, development, operations, and maintenance tasks in many cases require the ability to monitor a particular value over some period of time. For example, consider studying the effects

of different temperatures on a device or monitoring a patient's vital signs while the patient is in a hospital's care. Monitoring values of interest is essential to perform quantitative analysis in almost any research or production environment.

These scenarios share a common theme: the need to track discrete quantities over time. Furthermore, many times data points need to be gathered from different physical locations, and delivered to researchers, technicians, clinicians, operators and other management who are distributed across a wide campus or potentially the entire world. (For example, a clinician who travels all over a hospital's campus but needs to receive updates about all patient’s status in real time). The readout system is an applied research topic in the application of mobile cloud computing and wireless communications concepts. The readout system framework provides facilities for quickly configuring, capturing, aggregating, and reporting the status of data points (i.e., series) over a particular period of time.

Quantitative data is driving innovation and efficiency today in almost all facets of daily life. Wireless pedometers are tracking steps over time to provide personalized healthcare. Distributed networks of weather stations work in symphony to enable fine-grained insights into local and global weather patterns. All of these innovations require dedicated infrastructure and application-specific logic to enable wireless capture, aggregation, and reporting of data. The infrastructure requires time and effort to design, implement, and maintain. Furthermore, in a research and development environment, the data points of interest will likely change as research matures and researchers have a better understanding of how a particular process functions and the relevant data which describes a particular process.

Capturing and interpreting a posteriori information is time consuming and inflexible. As research matures, researchers may want to capture additional data points as part of an updated experimental procedure. Many mobile cloud computing setups are configured to capture a static set of data. The static nature of data capture can make using mobile cloud patterns in research environments difficult as researchers may need to spend excess amounts of time re-tooling their data capture setups to capture new data points as part of a revised experimental procedure. The amount of time spent re-tooling data capture tools versus performing experiments and analyzing data currently makes mobile cloud computing tools inefficient for use by researchers.

Consider that mobile cloud computing solutions traditionally rely upon hosted or distributed infrastructure, compute and data nodes that are used to aggregate data into a database and provide persistence for data. A database or other datastore is essential for enabling access to data for both (i) storing experimental data points and (ii) interpretation of data points through visualization or by asking questions of data using queries such as the Standard Query Language (SQL). Many databases rely upon a schema which outlines the data points each table in a database expects. The evolving nature of experimentation implies that a schema may be constantly changing as the experimental data of interest changes over the course of a research project. Having to constantly update a database's schema and the corresponding data capture

tools to support the new schema with each iteration requires significant effort as part of an experiment. In many cases this additional effort is difficult to justify in research environments, as the experiments are relatively short lived compared to the amount of effort that must be invested to create and maintain the data capture tools and infrastructure. Therefore, mobile cloud solutions are not efficient in research contexts.

Looking closer at how many research experiments and production monitoring scenarios are performed, a three step pattern emerges, which is shown in Fig. 10: (i) a set of values of interest are identified for monitoring, (ii) data is then captured and aggregated into a database or another centralized data store, and (iii) researchers and operators evaluate the values of the data points over a specific period of time. It is also possible that certain data points only have relevance when evaluated as a group, so groups of points may be evaluated over a period of time. This pattern very closely matches the time-series pattern in databases, where a value of interest is always measured over time (i.e., if plotted, one axis of the plot always corresponds to time).

The dynamic nature of experimentation requires that the quantity and type of data points can vary throughout the course of different experiments as research matures. When applying the time-series pattern, it is important that each data point can be broken down into its constituent parts. So a complex data point, such as an array, would need to track each element in the array independently over time. This facilitates simple data aggregation where a pre-defined data schema is not required. Data points can be added or omitted when capturing experimental data.

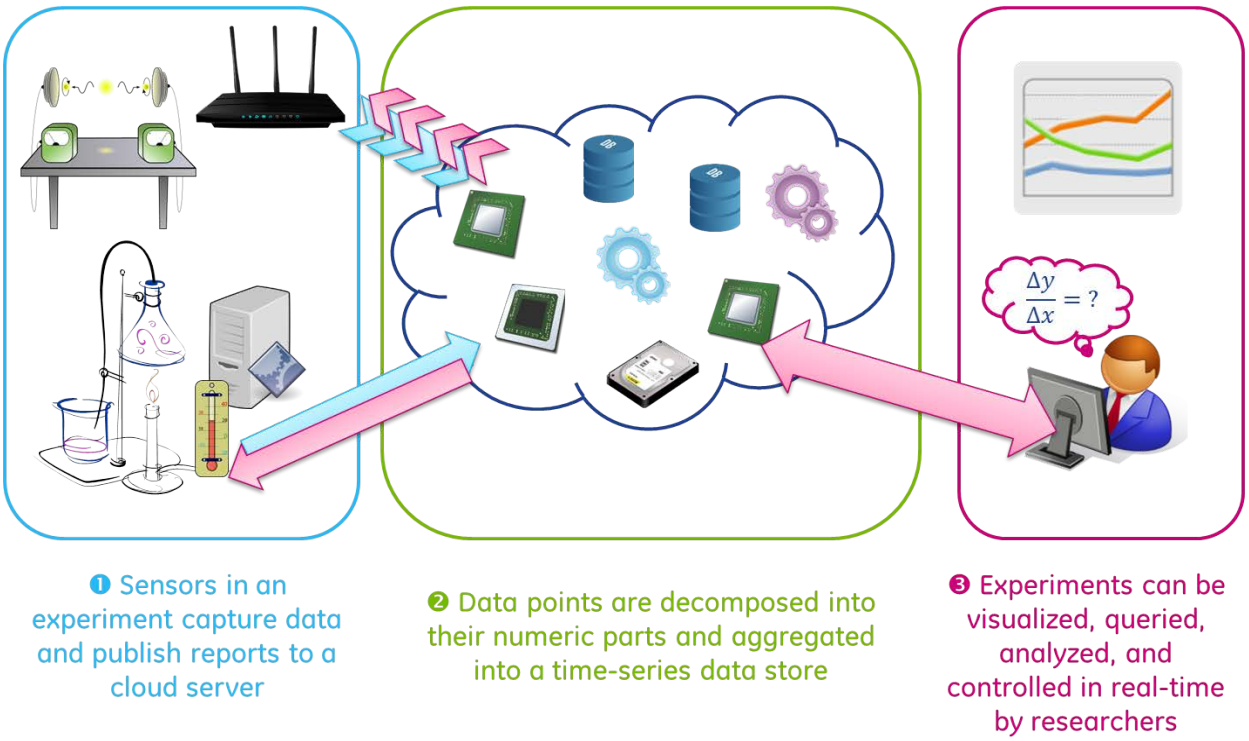

Fig. 127: Major three components in a typical readout system.

Predix is GE's software platform for the Industrial Internet.[39] Predix enables industrial scale analytics for asset and operations optimization by providing a standard way to connect machines, data, and people (see Fig. 128). Deployed on machines, on-premise, or in the cloud, Predix combines an industry leading stack of technologies for machine-to-machine communications, distributed computing and big data analytics, asset management, and mobility, delivering on the industry's needs for scalability, extensibility, customizability, and security. Some of the benefits of Predix are-

- **Machine-Centric:** Connect, make machines intelligent, and optimize them from anywhere in the network.
- **Industrial Big Data:** Optimized for real-time, large-scale analytics and asset management.
- **Modern Architecture:** Rapidly deliver consumer-grade Industrial Internet apps with a cloud-agnostic big data platform.
- **Resilient and Secure:** Protect industrial data and control access to machines, networks, and systems

Predix provides a standard, stable environment that will make it easier to connect, retrofit, and upgrade industrial assets to networks of machines and machine apps, systems, people, and processes, while enabling embedded analytics that can make machines intelligent and self-aware. The Predix platform is also scalable, supporting high-volume analytics, industrial data and operational management, across individual machines and entire networks, on-premise, in the cloud, or in a hybrid environment. And Predix is adaptive, allowing applications to be customized and extended across industries and their assets, data sources, and devices, both mobile and fixed.

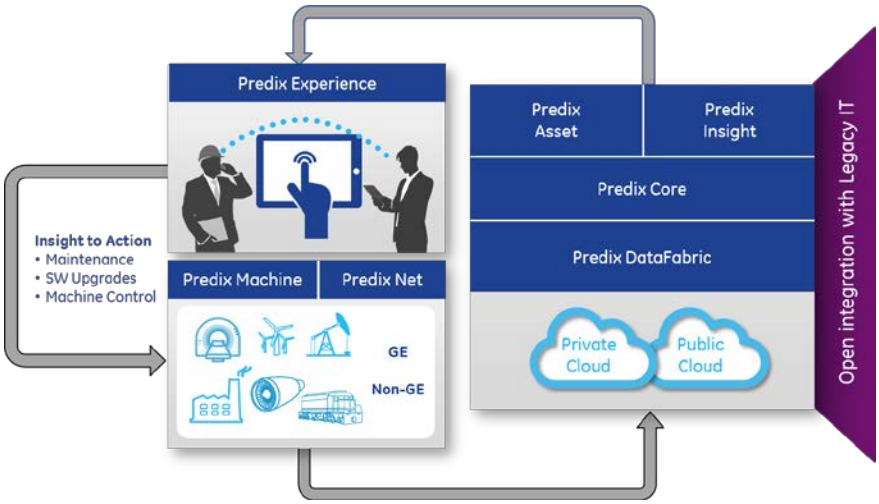

Fig. 128: Predix architecture – connecting people, machines, and big analytics. [Source: http://inside.sw.ge.com/products/predix]

GE's approach to developing Predix and bringing it to market starts with an understanding of the rapid changes at work in the industrial world, gleaned from its experience providing advanced industrial equipment and services. With this background, GE realized the need to accelerate the development, adoption, and time to market of modern industrial solutions and reduce the capital and operational cost and complexity of their use. To enable these goals, GE recognized early on the need to support a standard machine app model and a variety of existing and emerging requirements for connectivity, user experience, machine intelligence, analytics, and advanced industrial operations. It became clear that embodying these concepts in the Predix platform will enable GE, its customers, and partners to accelerate innovation. To this end GE is taking the lead by incorporating Predix into its machines and its Predictivity advanced Industrial Internet solutions.

GE is working with a rich ecosystem of technology partners, application developers and relevant standards groups to make Predix broadly available to the market at a rapid pace. Predix consists of three basic components that underlie the provision of the advanced capabilities we have described above. (For a more complete understanding of Predix please go to: www.GESoftware.com/Predix)

Machines: Predix serves as the enabling platform for the development, deployment, and management of software-defined machines and machine apps. This includes the virtualization of operating environments and the use of embedded hypervisors that can leverage the separation of functionality and services on advanced multi-core processors. This capability enables industrial assets of all kinds to be transformed into Brilliant Machines, including legacy systems and devices, which function as components of an advanced operational and analytical environment. Industrial operators can now deploy, update, maintain and improve assets without service interruption.

Networks: Predix enables the real-time, scalability and functionality requirements of the Industrial Internet, and provides a connectivity platform for the analytics, operations, and wide-area control required in the modern industrial company. This means being able to connect all assets—machines as well as people—in a highly safe and secure environment. Deterministic machine-to-machine connectivity, as well as support for legacy connectivity protocols, is enabled by Predix. The platform also supports a consistent performance and user experience environment backed by support for industrial service level and quality requirements.

Users: Providing a modern, consistent user experience was a key design goal for Predix. This includes support for a highly functional and efficient development environment that can deploy software that integrates data and processes from across the Predix world. The development environment also enables the creation of new apps that can leverage mobile use requirements in a hardware and operating system-neutral manner. Most importantly, the Predix user experience supports the interaction of users with Brilliant Machines and other advanced industrial assets,

and provides a new user experience that is commensurate with the new functionality that Brilliant Machines and the Industrial Internet can unleash.

Project summary and conclusions:

In the course of this project, a novel fiber-optic technique for interrogation of MEMS-based pressure sensors was developed and demonstrated. The technique was shown to enable multiplexing of sensors onto the same optical fiber by both power division and wavelength division, with potentially ~60 or more sensors addressable on a single fiber. In this manner, it should be possible to develop a single fiber optic cable with only 2 – 3 fibers that can accurately measure downhole pressures and temperatures at hundreds of points in order to monitor CO_2 plume penetration, as well as monitoring for CO_2 leakage from the sequestration cavity.

Two sensor packages were assembled and spliced into a single cable onto a single fiber. The outer diameter of each package was only 7/16” or 1.1 cm, another significant achievement of the current project, which is much smaller than the original single point pressure sensor developed in an earlier project that had a 3 cm diameter. The narrower sensor package makes it possible to splice multiple sensors into a cable at the factory prior to deployment on the field, as well as making actual deployment of the cable with the spliced sensors much simpler.

One sensor package contained an earlier, low pressure Si sensor die with a high Q response and the other package contained a low Q sensor die specifically fabricated for the high pressure environment of this project. The two packages were sequentially multiplexed using ¼” stainless steel cable that had been previously used for two downhole deployments and tested using the pulsed laser interrogator developed during this project. Simultaneous measurement of resonant frequencies of both sensors were obtained with integration times of 16 minutes or less with high SNR using a fiber splitter for multiplexing, demonstrating the principle of the interrogation technique.

One sensor was subsequently tested in a high pressure vessel at temperatures up to 200°C and pressures up to 5000 psi, though the sensor began to leak at 100°C and 5000 psi, and failed completely as the temperature was rising to 200°C. This failure is most likely due to either an incomplete seal of the hypodermic tube at one end inside the sensor package or a failure of the hard solder attachment process for the membrane to the sensor package. Therefore, while the basic package design should be suitable for operation to temperatures of 250°C and 10 kpsi, this was not able to be demonstrated.

A remote monitoring system using LabView code on a PC designed to interface with the GE Predix industrial internet was also demonstrated in which data collected from a pressure sensor was wirelessly transmitted through a Verizon cell-based connected to the Amazon cloud, from which it was continuously monitored in real time using a web-based protocol.

Acronyms and abbreviations

AWS	Amazon web services
BF	(Predix) business framework
CCUS	Carbon Capture, Utilization and Sequestration
COTS	commercial of-the-shelf
CSS	cascading style sheets
CTE	coefficient of thermal expansion
CW	continuous wave
EPA	Environmental Protection Agency
FWHM	full width at half maximum
GE	General Electric
GRIN	graded index (lens)
HP	Hewlett Packard
HTML	hypertext markup language
HTTP	hypertext transfer protocol
IIDx	industrial internet design extensions
IoC	inversion of control
ISO	disk image
JDK	Java development kit
JMS	Java message service
JRE	Java runtime environment
JS	Java scripts
MEMS	micro-electro-mechanical system
MOEMS	micro-optical-electro-mechanical system
MR1	maintenance release 1
NETL	National Energy Technology Laboratory
OS	operating system
PC	personal computer
RMS	remote monitoring service
SCS	sensor control service
SM	single mode (optical fiber)
SMS	sensor monitoring service
SNR	signal-to-noise ratio
SPF	service provider framework
SQL	standard query language
TCP	transmission control protocol
TEC	thermoelectric cooler
TERPS	trenched etched resonant pressure sensor
VI	LabView software module
WDM	wavelength division multiplexer

XML extensible markup language

Acknowledgment and Disclaimer

This material is based upon work supported by the Department of Energy under Award Number DE-FE0010116.

This report was prepared as an account of work sponsored by an agency of the United States Government. Neither the United States Government nor any agency thereof, nor any of their employees, makes any warranty, express or implied, or assumes any legal liability or responsibility for the accuracy, completeness, or usefulness of any information, apparatus, product, or process disclosed, or represents that its use would not infringe privately owned rights. Reference herein to any specific commercial product, process, or service by trade name, trademark, manufacturer, or otherwise does not necessarily constitute or imply its endorsement, recommendation, or favoring by the United States Government or any agency thereof. The views and opinions of authors expressed herein do not necessarily state or reflect those of the United States Government or any agency thereof.

References

[1] Mao et al., *13th Annual CCUS Conf.*, Pittsburgh, 2014.
[2] see Inconel 625 data sheet at http://www.specialmetals.com/documents/Inconel%20alloy%20625.pdf
[3] K. Sridharan et al., "Corrosion of Candidate Alloys in High Temperature Supercritical Carbon Dioxide," presentation at the Supercritical CO_2 Power Cycle Symposium, Boulder, CO (2011).
[4] M. Anderson, "Materials, Turbomachinery and Heat Exchangers for Supercritical CO_2 Systems," Project 09-778 Final Report, Department of Energy, Nuclear Energy University Programs.
[5] Goodfellow Inconel foil
[6] Indium Corp. of America hard solder table
[7] RubyFluid flux
[8] Component Supply tubing
[9] Thorlabs ceramic ferrules
[10] Fiberguide gold-coated fiber specs
[11] Comcore high temperature WDM
[12] Comcore high temperature splitter
[13] Gould high temperature splitter
[14] http://www.flexoptix.net/en/dwdm-channels
[15] http://www.transmode.com/en/technologies/wdm/cwdm
[16] Agiltron CWDM specifications
[17] Stanford Research SR530 lock-in amplifier
[18] Thorlabs DET01CFC detector
[19] Thorlabs FPL1009S for 1550 nm, Thorlabs FPL1053S for 1310 nm
[20] QGlex ASE light source
[21] J. Molina, R. M. Stitt, "Fileter Design Program for the UAF42 Universal Active Filter," Burr-Brown Application Bulletin AB-035.
[22] Thorlabs FPL1053S laser diode
[23] Stanford Research SR530 lock-in amplifier
[24] Thorlabs ITC4020 laser driver
[25] Thorlabs PDA10CS detector
[26] Thorlabs PBC1550PM-FC polarization combiner
[27] Cybel pulsed fiber laser
[28] Thorlabs SFL1550S external cavity laser
[29] R. Nawrodt et al., "High mechanical Q-factor measurements on silicon bulk samples," *J. Phys.* **122** (2008) 012008.
[30] N. D. Stokes et al., "Self-excitation in fibre-optic microresonator sensors," *Sens. Act.* **A21-A23** (1990) 369-372.
[31] R. M. Langdon and D. L. Dowe, "Photoacoustic oscillator sensors," *Proc. SPIE* **798** (1987) 86-93
[32] D. W. Carr, L. Sekaric and H. G. Craighead, "Measurement of nanomechanical resonant structures in single-crystal silicon," *J. Vac. Sci. Technol.* **B 16** (1998) 3821-3824.
[33] M. Zalalutidinov et al., "Frequency entrainment for micromechanical oscillator," *Appl. Phys. Lett.* **83** (2003) 3281-3283.
[34] K. Aubin et al., "Limit cycle oscillations in CW laser-driven NEMS," *J. Microelectromech. Sys.* **13** (2004) 1018-1026.
[35] https://www.gesoftware.com/industrial-internet
[36] http://www.washingtonpost.com/business/on-it/ge-brings-the-internet-of-things-to-the-factory-floor/2014/08/01/8b78cd74-176c-11e4-85b6-c1451e622637_story.html
[37] Nikhil Chauhan, "Modernizing machine to machine interactions – a platform for igniting the next industrial revolution," White Paper. [Available Online] www.gesoftware.com, October 2014.
[38] GE Software, [Available Online] www.gesoftware.com, October 2014.
[39] Nikhil Chauhan, "Modernizing machine to machine interactions – a platform for igniting the next industrial revolution," White Paper. [Available Online] www.gesoftware.com, October 2014.
[40] GE Software, [Available Online] www.gesoftware.com, October 2014.